Meteorology and lidar data from the URAHFREP field trials

Ott, Søren; Ejsing Jørgensen, Hans

Publication date:
2002

Document Version
Publisher's PDF, also known as Version of record

Risø–R–1212(EN)

Meteorology and lidar data from the URAHFREP field trials

Søren Ott & Hans E. Jørgensen

Risø National Laboratory, Roskilde, Denmark
May 2002

Abstract This report describes the experimental results obtained by the Risø team during the URAHFREP field trials.

URAHFREP, *Understanding dispersion of industrial Releases of Anhydrous Hydrogen Fluoride and the associated Risk to the Environment and People*, is a project sponsored by the European Commission under contract ENV4-CT97-0630. The purpose of the field trials is to study the possible influence of HF thermodynamics on the dispersion of atmospheric HF clouds. Models predict both negative buoyancy (heavy gas) effects and positive buoyancy effects depending on concentration, humidity and other factors. The main question addressed by the experiments is whether these effects in reality are strong enough to dominate naturally occurring fluctuations. If so plume lift-off can be expected, and even without lift-off it is possible that vertical mixing is enhanced.

In order to test if the lift-off or enhanced mixing created by the HF release was strong enough compared to the naturally fluctuations the HF releases were accompanied by passive smoke release, made shortly after to obtain a reference to the HF release.

The instrumentation included various types of HF sensors, thermocouple arrays, a fully instrumented release rig, a passive smoke machine, a meteorological mast and a lidar backscatter system. In addition video and photography was deployed. Pots with grass were set out in the far range for the purpose of studying environmental effects. This report deals exclusively with the meteorological data and the lidar data.

The trials cover a range meteorological conditions. These include neutral conditions with relatively high windspeed and low humidity as well as unstable conditions with low windspeed and high humidity, the most favorable conditions for lift-off to occur.

The lidar was used to scan vertical cross-plume slices 100 meter downwind of the source. The scan rate was about 1 scan per second. From these measurements various indicators of the plume geometry have been extracted.

A comparison of plume characteristics for HF clouds and passive smoke clouds has been made. The analysis shows no sign of any difference between the dispersion of HF and passive smoke except for one release, where a positive buoyancy effect cannot be excluded. An enhanced mixing effect of HF was not observed.

This work was funded by the The European Commission under contract ENV4-CT97-0630.

ISBN 87–550–2762–8
ISBN 87–550–2763–6 (Internet)
ISSN 0106–2840

Print: Pitney Bowes Management Services Denmark A/S · 2002

Contents

1 Introduction

The field campaign is a part of the EU sponsored project called URAHFREP (*Understanding dispersion of industrial Releases of Anhydrous Hydrogen Fluoride and the associated Risk to the Environment and People*). The purpose of the field trials was to conduct a series of medium scale (~ 0.1 kg/s) atmospheric releases of anhydrous Hydrogen Fluoride in order to assess dispersion characteristics of the substance. The campaign took place during August 2000 at the DERA site near Porton in southern England.

1.1 Participants

The campaign was conducted in co-operation with the following institutes:

- Commission Energy Atomique (CEA/DAMRI): Coordination of the scientific team, filter samplers and electrochemical sensors.
- Chemical and Biological Defence Establishment, Porton Down, DERA: Site owner, Trial Conducting Officer, safety, general assistance.
- Health and Safety Laboratories, HSL: Release rig construction, instrumentation and operation, thermocouple arrays, HF handling expertise.
- Laboratoire de Spectromètrie Physique, UJF: Short path spectroscopic sensors.
- Risø National Laboratory: Micro-meteorology and lidar measurements.
- CEA/DAM/DASE: Flora impact study

Only the micro-meteorological measurements and lidar measurements, for which Risø had the responsibility, are reported here. In addition some preliminary comparisons between the HF measurements by CEA/DAMRI and the lidar measurements are also shown.

1.2 Objectives

The field campaign is a central activity in the URAHFREP project. The trials investigate the atmospheric dispersion characteristics of Hydrogen Fluoride, where buoyancy effects, caused by the special thermodynamic properties of HF, is the main issue. Model predictions indicate that HF clouds may lift off the ground under meteorological conditions involving not-too-low atmospheric humidity and not-too-high windspeeds. The purpose of the trials was to determine whether lift-off actually occurs, and under which conditions. In cases where the cloud does not lift off the ground it is still possible that the mixing is enhanced. The detection of enhanced mixing was also an objective.

The objectives for Risø's work were to

- measure meteorological conditions
- make lidar measurements

The purpose of meteorological measurements is to establish the basic surface layer parameters which are input to dispersion models. According to surface layer theory the statistics of the wind field are characterized by the vertical fluxes of momentum and sensible heat together with mean values of wind speed and temperature at a reference height. This should be supplemented by the absolute humidity

(essentially independent of height) and the barometric pressure. Many of the instruments on the meteorological mast were replicated at other heights, making it possible to obtain vertical profiles.

The lidar measurements were made in order to compare HF plumes with passive smoke plumes. The idea is to make a passive smoke release immediately after each HF release and scan both with the lidar. The duration of the HF releases were restricted to 3 minutes while the smoke releases could be made longer (typically 10-20 minutes). A sampling time of only three minutes could be too short to obtain reliable mean value estimates for some statistics. However, the situation is worse for statistics that are sensitive to meandering, which is known to involve long timescales. This is the case for isolated measurements with fixed sensor, but not for the cross-plume integrated average concentrations, which can be obtained from an arc of sensors or from cross-plume lidar measurements. The somewhat longer smoke releases, which were done under similar meteorological conditions as the HF releases, should make it possible to obtain reliable estimates of quantities characterizing plume geometry.

1.3 The site

The trials were conducted during August 2000 at the DERA test site near Porton in southern England. The institution has a long record of studies of boundary layer meteorology and a large number of dispersion experiments have been conducted there. The classical Pasquil system for classification of atmospheric stability was developed at the institution.

The site measures about 5 by 7 kilometers. Along the periphery is a belt which is used for farming. The central parts, which have not been cultivated since 1917, are covered by low vegetation with small groups of trees and few buildings. Due to the unique wild life, counting rare species of birds and insects, English Heritage has categorized the area as a 'site of special scientific interest'.

The release rig was placed at the SW rim of Boscome Bowl in the central region of the range. Releases were conducted for winds blowing into a 60° wide experimental sector extending roughly NE from the rig. Following the centreline of the experimental sector, moving downwind from the release point, the terrain slopes gently (~ 0.01 m/m) reaching the lowest point of the Bowl approximately 1200 meter from the rig. After this is a fairly steep climb (~ 0.05 m/m) up to Tower Hill. A ridge marks the eastern and northern edges of the Bowl. The ridge turns and ends at Tower Hill about 3 Km NE of the release point. Upwind of the rig is a wide open fetch with grass and a few isolated groups of trees. South of of the rig is a small hill (Moll Harris Clump) and further towards SE is a large Hill (Battery Hill). The grass had been cut in a 200×200 m^2 area extending 200 m NE from the rig and 100 meter to either side of the centreline.

1.4 HF thermodynamics

The thermodynamical properties of HF are peculiar. The boiling is point 19.6°C, hence it is normally stored in liquid form under moderate pressures (including pressures below the atmospheric pressure). The vapour is one of the least ideal gases known. This is due to oligomerization of the gas, which means that diatomic HF molecules form oligomers, i.e. small polymer chains or rings. This raises the effective molecular weight of HF vapour to about 3 times the value expected for a diatomic gas. Concentrated HF vapour is therefore a heavy gas. The oligomerization also lowers the enthalpy of the vapour. Therefore HF vapour cools substantially if it is mixed with dry air. This is because mixing lowers the partial pressure of HF causing the oligomers to break up, which is an endothermic process. The

effect of the oligomers is analogous to the effects of droplets in a spray in the sense that droplets require heat to evaporate, just like oligomers require heat to break up into monomers. However, oligomerization is not the only special feature of HF thermodynamics. Liquid HF and water are mixable in any proportion, and the mixing enthalpy is very large (i.e. mixing generates a lot of heat). This means that HF droplets attract water vapour. In humid air HF droplets therefore tend to grow and get hot, because moisture condenses into them, instead of shrink and get cold as is the case for most other substances. In fact a hot fog may result even if the HF and the air are both initially gaseous. Depending on ambient humidity, temperature, the degree of dilution, and other factors, either mechanism (cooling/heating) may dominate. The cloud may therefore become positively or negatively buoyant and even change between the two as the concentration drops. The growth of the droplets can continue to quite low concentrations (0.1%, say) because of the extremely low vapour pressures of HF-water mixtures. Eventually the droplets evaporate, and the cloud cools and becomes slightly denser than the surrounding air. An HF cloud may therefore 1) become heavier-than-air because of oligomerization, 2) become heavier-than-air because of cooling caused by de-oligomerization 3) become lighter-than-air due to interaction with water and 4) eventually become slightly heavier-than-air as the fog disappears.

1.5 General experimental design

Below a brief summary description of the experimental design is given. For more details information reference is made to data reports of the partners.

Sensors

The following sensors were deployed:

- Chemical filters. The filters were respirated by air pumps at a fixed rate. The pumps could be switched on and off by a radio signal. The filters were analysed in order to obtain the dose. An average concentration can be deduced from the dose, the pumping rate and the time of exposure *(Participant: CEA/DAMRI)*.
- Electrochemical HF sensors. These devices were placed at 1000m and a few at 2000m *(Participant: CEA/DAMRI)*.
- Short path instruments. An accurate, fast response HF sensor developed by UJF.
- Boreal long path instrument. Measures a line integral of the concentration *(Participant: HSL)*.
- Thermocouple arrays. 128 thermocouples were placed in two 2D arrays in the near field *(Participant: HSL)*.
- Bubblers. Deployed in the far field ($\sim$ 2000 m) for the environmental impact study. Measurements of time averaged HF concentrations *(Participant: CEA/DAM/DASE)*.
- Release rig instrumentation: temperature, pressure, flow rate of HF *(Participant: HSL)*.
- Lidar measuring backscatter from aerosol in the the cloud. The measurements can be interpreted in terms of HF concentrations in a vertical plane. See section A.1 *(Participant: Risø)*.
- Meteorological instruments. See section 2.2 *(Participant: HSL)*.

Only the last two items are covered by this report. For the remaining items reference is made to data reports from the other partners.

HF releases

The release rig had been constructed by HSL and is described in detail in the HSL data report. Its basic function is to produce a well defined horizontal jet of liquid HF. This was achieved by pressurizing a portion of liquid HF with nitrogen in a separate container and then discharge the contents through a nozzle. The nozzle pointed horizontally downwind at a height on 1.2 meter. A rather small nozzle diameter was chosen in order to get a spray of HF droplets small enough to be airborne. Butane could be added to the release by means of a similar nozzle located next to the HF nozzle. In the few cases where butane was added it was observed that the two jet merged instantly. A third, smaller nozzle was used to add a small amount of ammonia (NH_3) to the release. The ammonia reacts with HF producing solid NH_4F aerosol, which makes the plume clearly visible even at large downwind distances. This was done in order to mark the plume both for security reasons and to make it detectable by the lidar. In all cases the discharge of liquid HF lasted close to three minutes. Immediately following the liquid discharge, small amounts of gaseous HF and nitrogen would continue to escape for a few minutes. The ammonia seeding was stopped during gaseous discharge.

Table 1. Key parameters for the releases

Trial	Date	Time	HF rate kg/s	NH_3 rate kg/h	HF Press bar	HF Temp °C	Duration s
HF001	9/8	15:17	0.06	0	4.13	18.6	85.25
HF002	9/8	17:30	0.075	3.5	6.67	18.09	131.08
HF003	10/8	09:29	0.15	3.5	–	–	102
HF004	14/8	10:43	0.085	3.5	8.7	16.59	184.52
HF005	14/8	13:35	0.085	3.5	8.83	15.84	180.00
HF006	14/8	16:29	0.085	3.5	8.66	19.11	186.75
HF007	15/8	11:18	0.145	3.5	3.78	18.78	106.21
HF008	16/8	09:32	0.105	3.5	4.04	13.86	145.19
HF009	16/8	13:08	0.11	3.5	4.7	17.9	141.67
HF010	17/8	08:08	0.115	3.5	4.91	10.84	178.76
HF011	17/8	09:24	0.11	3.5	4.78	13.03	187.39
HF012	21/8	07:48	0.125	2	5.74	7.98	163.41

For the HF releases the naming convention is e.g. HF008 for trial 8. The first smoke release made immediately after HF008 is called HF008S1, the second is called HF008S2 etc. In HF009 the isobutane rate was 0.013 kg/s, the isobutane tank pressure 4.75 bar and the isobutane tank temperature 12.85 °C. The corresponding numbers for HF011 are 0.99 kg/s, 4.84 bar and 10.75 °C. In HF003 HF the tank pressure and temperature are not available.

Smoke releases

The smoke was produced by a smoke machine constructed by Risø (Jørgensen and Mikkelsen 1993). It produces smoke by spraying liquid $SiCl_4$ and ammonia water into the jet of an electric fan. The chemicals react instantly to form solid SiO_2 and solid NH_4Cl, which produce a thick, white aerosol smoke. The smoke was released horizontally at a height of 1.2m above the ground.

Smoke releases were made immediately following each HF release (except for trial 11 where the smoke machine was down). The period between the releases

was kept as short as possible, in practice about ten minutes. For some of the trials there are more than one smoke release. In some cases this is because the smoke turned into an unacceptable direction or troubles with the smoke machine. In others it is because the lidar was restarted after about ten minutes. This was done in order to prevent data jam, which can occur for too long sampling times.

1.6 Visual observations

From the field observations it became clear that a genuine lift-off did not occur. Most plumes were definitely on the ground at all times. None of the clouds permanently lost contact with the ground, and those clouds that were observed in the far field ($\sim$ 1000m from the source) were all clearly on the ground. This was true even for Trial 12, where, however, the plumes were frequently losing ground contact in the near field ($\sim$ 100m from the source). In Trial 12 the plumes were also clearly more spread out in the vertical direction than for the other trials. It should be noted that this behaviour was observed both for HF and the smoke. The thermally induced turbulence in the unstable surface layer must therefore have contributed to this behaviour, but we had the impression that the HF release (HF012) showed a larger effect than the subsequent smoke releases. A series of photographs, all taken just outside the control room, show a great deal of similarity between the two types of clouds as well as a large influence of meteorological conditions. Judged from the visual observations it thus appears that buoyancy effects might have been present, but that they were severely masked by turbulent fluctuations.

In the first experiment there was no ammonia seeding of the HF cloud. We observed that it became invisible at a downwind distance of about 30 to 40m. The clouds seeded with ammonia were visible at much larger distances (one kilometer or more) due to the content of NH_4F aerosol.

A number photographs and video recordings document these observations. The material has not been analyzed.

2 Meteorological measurements

2.1 Meteorological conditions

Optimal conditions

From the point of view of model testing the interesting meteorological conditions are those that highlight the effects of HF thermodynamics on the dispersion. These conditions are characterized by low windspeeds combined with high relative humidities. Calculations based on realistic thermodynamics and simple ballistics show that plume rise cannot be expected if the windspeed is too high or the relative humidity is too low. It was therefore a primary concern to seek to achieve meteorological conditions where a clear effect might be observed.

Light wind is often fluctuating and large random changes of the wind direction may occur. As a safety precaution HF releases were ruled out under conditions lacking a well established wind direction. This was judged from our own local measurements, which were displayed in the control room, consistency with the weather forecast and comparison with simultaneous measurements taken at Larkhill about 10 km from the site.

Porton weather

The weather at Porton is dominated by systems coming in from the Atlantic. This implies frequent weather changes and low chances of having the same wind direction for extended periods. The experimental sector had been aligned so as to maximize the distance to the site boundaries. This also favours prevailing wind directions, which in August are in the SW at Porton (i.e. blowing *towards* NE). Fortunately the weather in August 2000 was no exception, but the restriction of the HF releases to a narrow sector still ruled out experiments for most of the time.

Many of the trials, particularly those made during the second half of the Campaign, were done on days following calm nights with clear sky. Below we describe the main characteristics of this type of meteorological conditions.

Stable nights

During calm nights with no protective cloud cover, the ground cools rapidly by radiating heat through the atmosphere into the universe. In open terrain this creates a thin, cold and stably stratified layer. The layer develops during the night and is about 5-10 meter deep just before sunrise. At this point there can be temperature differences of more than ten degrees over a few meters. Most often the cooling is accompanied by fog forming within the cold layer. The stable density stratification very efficiently damps out the turbulence and thereby inhibits exchange of matter, heat and momentum between the cold layer and the atmosphere above. Because of the dynamic de-coupling the cold layer is primarily driven by gravity making it slide down local slopes in the terrain (drainage flow). Since the upper layer slides almost without friction on top of the cold layer a small forcing may cause it to accelerate. The velocity difference between the two layers therefore tends to increase until it reaches a critical point, where enough kinetic energy is available to lift up the cold layer. As a consequence the cold layer is rapidly mixed into the upper layer in a sudden burst of turbulence. Then the surface layer calms down again and the temperature continues to drop. The quiet periods between the bursts may typically last for about an hour. The stable nighttime conditions offer low windspeeds and high relative humidities, but the wind direction varies randomly. For safety reasons HF experiments were therefore confined to the daytime.

Unstable days

After sunrise the temperature gradient changes sign, and the atmosphere soon becomes unstable (we are assuming few or no clouds). The hot ground drives thermal motion which generates a turbulent boundary layer that grows to a thickness of a few kilometer. This creates motion on both small and large scales. The sea breeze acts on large scales of about 100 km. Over sea the boundary layer can split into polygonal convection cells measuring a few kilometer. Over land the boundary

layer more frequently splits into strips of alternating up- and down-draughts. The strips are parallel with the wind direction. The up-draughts are capped by 'streets' of cumulus clouds. Such cloud streets were often observed during the Campaign. Passing from one strip to another may cause a sudden change of the wind direction. Close to the ground the effect of the large scale vertical motion is relatively small, but the heating from below generates small scale turbulence which intensifies mixing. Vertical mixing tends to even out the temperature profile, except close to the ground, where a strong temperature gradient is maintained. The dispersion of plumes on the ground is strongly influenced by the convection which tend to split them up into disconnected parts.

The wind direction can change suddenly during unstable conditions. On several occasions we observed the wind direction changing by more than 90 degrees in just a few seconds. Due to the safety issue releases were avoided in periods with very unstable conditions (e.g. sunshine at noon). This seriously limited the opportunities for making experiments. The first half of the Campaign was dominated by cloudy days with relatively high windspeed. We could see no signs of buoyancy effects in the HF plumes and decided to concentrate on mornings following calm nights, as described above, in order to try to catch low windspeed and high humidity. This was achieved in trial 12. It appears in hindsight that early morning releases was in fact the only chance, but the disadvantage with early mornings is that it is a transition period, where the convective daytime boundary layer has just formed and starts to grow from zero height. This implies redistribution of momentum, kinetic energy and heat, and it is possible that the assumption of a constant flux surface layer may not be fully warranted.

2.2 The met mast

A 10m tall meteorological mast was erected at a point 30 m upwind of the release rig. The datalogger was located in a box about 20m from the mast. Table 2 lists the instrumentation of the mast.

Table 2. Instrumentation of the met mast

Instrument	Measurement	Height	Sampling
Cup anemometer	Wind speed	1.0, 2.0, 5.0, 9.5m	5Hz
Wind vane	Wind direction	2.0, 9.5m	5Hz
Sonic anemometer	3D wind and temp.	9.6m	20Hz
T-abs	Temperature	9.3m	5Hz
Barometer	Pressure	1m	5Hz
ΔT	Temperature dif.	9.3m and2.0m	5Hz
Psychrometer	Relative humidity	1.4, 8.8m	5Hz
Hygrometer	Relative humidity	4.8m	5Hz
Pyranometer	Light flux	2.0m	5Hz
T-surf	Radiation temp.	2.5m	5Hz
TC	Temperature	0.05, 0.1, 0.2, 0.4, 0.8	
		1.6, 3.2, 5.1, 7.0, 9.0m	5Hz

All instruments were read with a base frequency of 20 Hz and, except for the sonic anemometer, the data rate was further reduced by block averaging. The characteristics of the instruments and the calibration procedures are described in Appendix A.

The instruments on the met mast were logged continuously for the whole period.

Except for a few breaks the record goes from 10 am August 4 to 10 am August 25. The sampling scheme was the same whether or not an experiment was ongoing.

The datalogger clock was synchronized with the control room clock (a high precision radio controlled clock). This was done to an accuracy of about one second. After a few days we observed that the datalogger clock had lost some tens of seconds, and it was adjusted again. This was done every now and then and the deviations were noted. On the basis of these notes a time correction could be worked out. The timing of all measurements therefore refer to the control room clock.

2.3 Met overview

Table 3. Meteorological parameters for the releases

Trial	T_{av} s	U(2m) m/s	u_* m/s	RH(2m) %	T(2m) °C	L m
HF003	191	3.8	0.39	80	18.3	-150
HF003S1	1042	3.9	0.33	78	18.5	-118
HF004	259	5.2	0.27	89	20	-40
HF004S1	272	6.4	0.53	84	20.7	-162
HF004S2	272	7.0	0.49	81	21.1	-87
HF005	228	4.9	0.50	80	19.8	-436
HF005S1	135	5.1	0.32	81	19.8	-257
HF005S2	1131	5.5	0.43	83	19.6	-319
HF006	187	5.1	0.41	74	21.2	-80
HF006S1	635	5.2	0.49	74	21.2	-119
HF007	125	3.4	0.36	53	19.9	-30
HF007S1	939	4.0	0.36	49	20.7	-24
HF008	190	2.8	0.21	76	17.4	-6
HF008S1	446	3.5	0.31	70	18.1	-22
HF008S2	514	3.5	0.32	68	18.4	-18
HF008S3	462	3.4	0.23	67	18.7	-6
HF009	158	6.5	0.49	46	21.6	-67
HF009S1	274	5.3	0.44	48	21.2	-38
HF009S2	452	5.4	0.35	49	21.2	-25
HF009S3	430	5.6	0.38	48	21.4	-29
HF010	203	4.0	0.39	83	14.5	-180
HF010S1	614	3.9	0.41	82	14.8	-175
HF010S2	495	4.3	0.38	80	15.1	-95
HF011	199	4.6	0.50	69	16.7	-167
HF012	182	1.3	0.15	92	11.8	-21
HF012S1	710	0.8	0.11	92	12.3	-3
HF012S2	242	2.3	0.23	84	14.1	-22
HF012S3	122	2.1	0.27	83	14.1	-31
HF012S4	267	2.1	0.18	83	14.2	-16

Complete records in the form of time series of meteorological measurements will be made available in the rediphem database. Appendix B summarizes the meteorological parameters for each release. Table 3 gives an overview of key parameters. The averaging times, T_{av}, are also listed in the table. The averaging period for the meteorology is in each case equal to the averaging period used for analysis of the

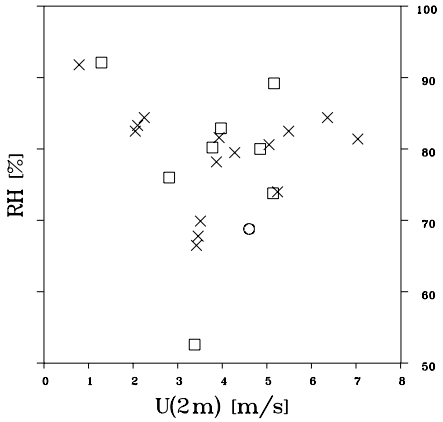

Figure 1. Scatter plot of relative humidity vs. windspeed. ×: Smoke, □: HF, ○: HF with butane.

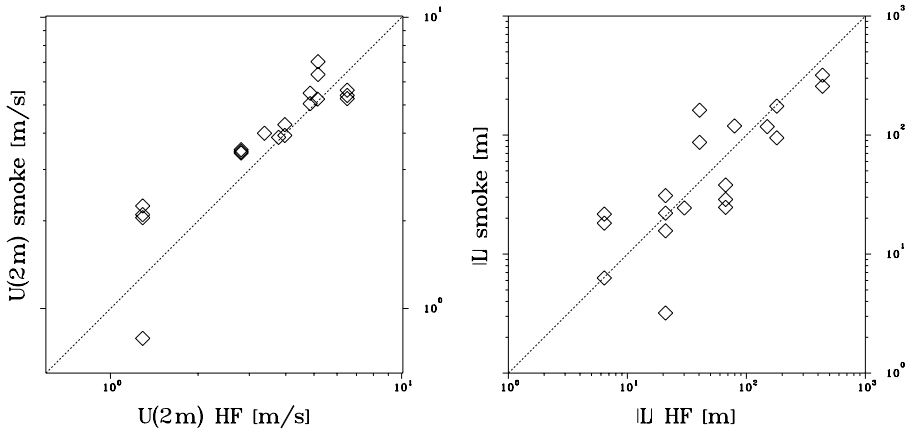

Figure 2. Comparison of windspeeds (left) and Monin-Obukhov lengths (right) during HF and smoke releases.

lidar data.

Figure 1 shows averaged windspeeds and averaged relative humidities (both measured at 2m level) for the releases. The relative humidity is most relevant for the HF releases. The points are scattered over a quite wide range of values, although few releases combine of low windspeed and high humidity.

Figure 2 compares the wind speed at two metre $U(2\text{m})$ and the Monin-Obukhov length scale L for corresponding HF and smoke releases. The windspeeds generally match well for large values and less well for the lowest values. The lowest windspeeds are for Trial 12, which differs in many ways from the other trials. A corresponding plot for the Monin-Obukhov length L is also shown (L is defined in Appendix B). L is obtained from flux measurements which are difficult to make, in particular for short time series, and this explains some of the scatter. Small values of $|L|$ are obtained in unstable atmospheric conditions and large values are for neutral conditions. Any large values ($\sim$ 100m, say) indicates neutral conditions and hence large values need not match closely. Small values indicate convection,

which influences the dispersion, and a close match of values for HF and smoke is preferable. This was not obtained. The 'worst' point is L=-21m during the HF release (HF012) compared to L=-3.2m during the smoke release (HF012S1).

In Appendix B there is a table for each trial showing key meteorological parameters for the HF plume and the corresponding smoke plumes. In most cases there is a fairly good agreement between conditions during the HF releases and the smoke releases. Very good agreement is found in trials 3, 6 and 10. Trials 5, 7, 8 and 9 are somewhat poorer, and for trial 4 and 12 the agreement is not very good.

2.4 z_o

The roughness length z_o is a constant in the logarithmic law for the average wind profile

$$U(z) = \frac{u_*}{\kappa} \log\left(\frac{z}{z_o}\right) \tag{1}$$

The law is valid for neutral atmospheric conditions over flat uniform terrain, where it is actually very accurate. It was determined in the following way. Based on meteorological data from the whole period, 30 minute periods were selected such that

- The average wind direction should be within the experimental sector
- The Monin-Obukhov length L should be less than -1000m or greater than 1000m
- The average windspeed at 10m height should be greater than 3m/s.

For each period the average windspeeds measured by the four cup anemometers, were plotted against $\log z$. In all these plots the four points lie closely on a straight line in accordance with (1). The slope determines u_*/κ and intersects with the $\log z$ axis determines $\log z_0$. The values of z_o are not constant, which is surprising. Figure 3 shows a systematic decrease of z_0 for increasing windspeed. Wind induced waves in the vegetation are expected to give the opposite dependence. Neither is it due to a displacement height, but it might be a terrain effect. In any case the roughness length always enters as $\log z_o$ and it should be safe to use the value

$$z_o = 2\text{cm}. \tag{2}$$

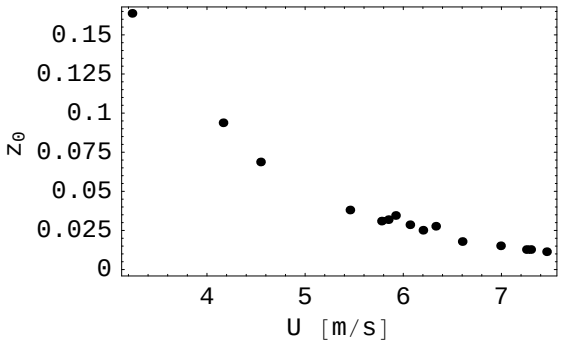

Figure 3. Surface roughness z_0 vs. windspeed U.

3 Lidar Measurements

The detection of possible lift-off of the HF plumes is the main objective, and for this the lidar system plays a central role. The lidar system is described in Appendix A. The essential lidar output is the extinction (attenuation due to aerosol particles) at points along the laser beam. The lidar is operated in sequences consisting of 20 shots with the laser along different angles. Together the 20 shots scan a vertical, transverse section of the plume.

Concentration

Calibration experiments made earlier have shown that there is a linear relation between extinction and concentration in smoke clouds seeded with SF_6. A linear relation between the measured extinction and the HF concentration can therefore be expected for the HF clouds seeded with ammonia, at least after the point where the HF-water droplets have evaporated. The visible plume observed in the first release was far too short to reach the 100m distance. This observation is consistent with the lidar measurements from HF001 in where backscatter is below the detection limit. It is likely that HF droplets had evaporated at 100m also for the remaining experiments, perhaps with the exception of Trial 12 (this is discussed elsewhere in this report). We therefore assume that HF-water droplets were generally not interfering with the lidar measurements and that the lidar signal was solely due to backscatter from the NH_4F aerosol. This implies that the measured backscatter is proportional to the HF concentration.

3.1 Plume parameters

Data conversion

The lidar system stores data in files with a definite record structure. A record contains a time stamp, various settings such as laser power, scan angles etc., and twenty line scans. A line scan consists of 500 integers corresponding to voltage readings of the storage scope corresponding to points with a spacing of 0.75m. The twenty lines were made at a frequency of 32 Hz representing an essentially instantaneous vertical slice across the plume. After conversion from raw voltages to concentrations (actually extinctions) the data were transformed from polar coordinates to a Cartesian coordinates by interpolation in a grid with a square grid spacing of 0.75m (both horizontally and vertically). In this way the concentration field $C(y,z,t)$ is obtained. For simplicity $C(y,z,t)$ is normalized so that

$$\int_{-\infty}^{\infty} \mathrm{d}y \int_{0}^{\infty} \mathrm{d}z\, C(y,z,t) \;=\; 1 \tag{3}$$

Plume parameters

This and the following integrals can be evaluated numerically from data. Using the normalized concentration we may write the height of the centroid as

$$H(t) = \int_{0}^{\infty} \mathrm{d}z \int_{-\infty}^{\infty} zC(y,z,t)\mathrm{d}y \tag{4}$$

We also define the average concentration for the sampling period T_{av}

$$\overline{C}(y,z) \equiv \frac{1}{T_{\mathrm{av}}} \int_{t_0}^{t_0+T_{\mathrm{av}}} C(y,z,t)\,\mathrm{d}t, \tag{5}$$

the vertical crossplume-integrated profile

$$\overline{C}_v(z) \equiv \int_{-\infty}^{\infty} \overline{C}(y,z)\,\mathrm{d}y, \tag{6}$$

and the horizontal depth-integrated profile

$$\overline{C}_h(y) \equiv \int_0^\infty \overline{C}(y,z)\,\mathrm{d}z. \tag{7}$$

From these we form the average height (or average centroid)

$$\overline{H} = \int_0^\infty z\overline{C}_v(z)\mathrm{d}z, \tag{8}$$

the vertical width

$${\sigma_z}^2 = \int_0^\infty (z-\overline{H})^2\overline{C}_v(z)\mathrm{d}z, \tag{9}$$

the horizontal centre

$$\overline{y} = \int_{-\infty}^\infty y\overline{C}_h(y)\mathrm{d}y, \tag{10}$$

and the horizontal width

$${\sigma_y}^2 = \int_{-\infty}^\infty (y-\overline{y})^2\overline{C}_h(y)\mathrm{d}y. \tag{11}$$

The averaging time interval, of length T_{av}, is not exactly the same as the release duration because the arrival of the plume at 100m plume is delayed by a about a minute. There is also a corresponding delay of after the release stops. We have found that a good indicator of the presence of the plume is obtained by integrating each lidar scan. The result is roughly proportional to the mass of HF in the vertical cross-plume slice at 100m. Ammonia seeding was applied only together with the discharge of *liquid* HF, and the switching on and off of the seeding is very clear on the lidar signals. An example is shown in figure 4. The time of arrival of the plume is particularly sharp and can be located to within a few seconds. The switching off is less sharp, but sharp enough to make it possible to select an interval of time where the HF mass in the scanned slice is roughly constant in time.

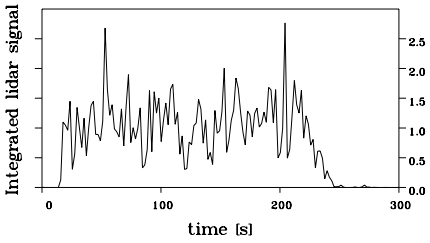

Figure 4. The integrated lidar signal, an indicator of the HF mass in the scanned slice, vs time for HF006.

3.2 Moving frame analysis

Plots of $\overline{C}_v$ and $\overline{C}_h$ for each release are shown in Appendix B. In general $\overline{C}_v$ is a regular curve which is well represented by the two parameters $\overline{H}$ and σ_z. The same is not true for $\overline{C}_h$, which is irregular and random deviating substantially from the gaussian shape used in many models. This irreproducibility of the horizontal

Table 4. Measured plume parameters

Trial	Plume	$\overline{\overline{H}}$ [m]	σ_z [m]	σ_y [m]	σ_{ym} [m]	σ_c [m]
HF003	HF	6.50	3.71	12.03	6.82	9.91
HF003S1	Smoke	4.69	3.06	14.48	7.91	12.13
HF004S	Smoke	4.87	2.68	15.08	8.83	12.22
HF004S1	Smoke	5.04	2.97	13.65	8.19	10.92
HF004S2	Smoke	4.31	2.83	21.70	9.91	19.30
HF005	HF	5.32	3.32	14.08	7.48	11.93
HF005S1	Smoke	4.92	3.01	12.58	8.81	8.98
HF005S2	Smoke	4.85	3.15	16.73	8.20	14.58
HF006	HF	6.08	3.48	12.39	6.55	10.52
HF006S1	Smoke	5.64	3.37	17.42	7.81	15.57
HF007	HF	7.03	3.43	13.92	6.67	12.22
HF007S1	Smoke	6.91	4.52	18.36	7.78	16.63
HF008	HF	8.15	4.77	13.02	6.86	11.06
HF008S1	Smoke	6.72	4.31	17.04	8.14	14.96
HF008S2	Smoke	6.66	4.21	25.47	8.94	23.85
HF008S3	Smoke	8.60	5.58	13.42	7.64	11.03
HF009	HF+butane	4.29	2.66	16.93	6.14	15.78
HF009S1	Smoke	5.78	3.78	14.81	8.13	12.38
HF009S2	Smoke	4.77	3.50	19.36	8.83	17.23
HF009S3	Smoke	4.99	3.29	25.58	8.75	24.04
HF010	HF	6.13	3.5	10.66	7.56	7.51
HF010S1	Smoke	4.96	3.33	10.14	6.58	7.72
HF010S2	Smoke	4.78	3.19	13.37	6.70	11.57
HF011	HF+butane	5.96	4.02	13.03	7.41	10.72
HF012	HF	19.29	7.46	11.23	8.42	7.43
HF012S1	Smoke	16.59	7.06	19.28	13.23	14.02
HF012S2	Smoke	11.40	6.77	17.71	8.00	15.80
HF012S3	Smoke	8.06	5.25	13.93	7.98	11.42
HF012S4	Smoke	9.23	6.03	22.66	10.24	20.21

profile is a general feature, which is seen for both short and large averaging times. It is caused by random changes of the wind direction, which make the plume wander from side to side, a phenomenon usually referred to as meandering. The horizontal width is therefore influenced by slow wind direction variations, which have no influence on the mixing process. In order to get a better measure of the plume width we introduce the so-called moving frame profile defined by

$$\overline{C}_m(y) \equiv \frac{1}{T}\int_0^T \mathrm{d}t \int_0^\infty \mathrm{d}z\, C(y + y_c(t), z, t) \tag{12}$$

where

$$y_c(t) = \int_{-\infty}^{\infty} \mathrm{d}y \int_0^\infty \mathrm{d}z\, yC(y, z, t) \tag{13}$$

is the instantaneous lateral plume centre. The idea is to evaluate the average concentration in a frame of reference following the instantaneous centre. From the plots in Appendix B it appears that the moving frame profiles are indeed very

regular and symmetric with almost the same shape. This indicates a high degree of reproducibility.

The moving frame plume width is defined as

$$\sigma_{ym}{}^2 \equiv \int_{-\infty}^{\infty} y^2 \overline{C}_m(y)\,\mathrm{d}y \tag{14}$$

We recall that

$$\sigma_y{}^2 = \sigma_{ym}{}^2 + \sigma_c{}^2 \tag{15}$$

where

$$\sigma_c{}^2 \equiv \frac{1}{T}\int_0^T (y_c(t) - \overline{y})^2\,\mathrm{d}t \tag{16}$$

is the observed variance of the lateral position of the plume centre. When $\sigma_c > \sigma_{ym}$ the meandering of the plume centre is the main contribution to σ_y. From Table 4 it appears that this is the case for almost all the plumes.

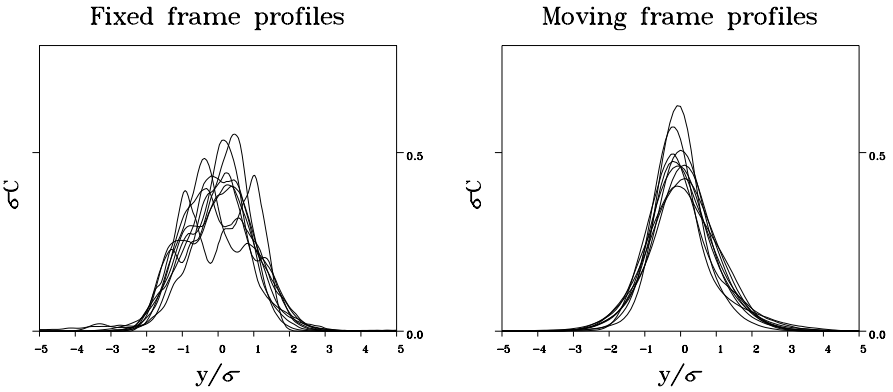

Figure 5. Depth integrated horizontal profiles from fixed and moving frame analysis.

Figure 5 shows measured profiles plotted as $\sigma_{ym}\overline{C}_m$ vs y/σ_{ym} for moving frame data and $\sigma_y\overline{C}_h$ vs y/σ_y for fixed frame data. In this plot the moving frame profiles look fairly similar, and $\overline{C}_m$ is well represented just by its width. The fixed frame profiles are more scattered. Table 4 shows the plume parameters obtained for the releases. The general picture is that both $\overline{H}$, σ_z and σ_{ym} are very similar for HF and smoke. We also note the large differences between plume widths determined by the two methods. In most cases σ_y is more than twice as large as σ_{ym}, which means that σ_y primarily measures the meandering of the plume centre. HF is not likely to influence the large scale eddies that produce plume meandering, and hence differences of σ_y for the two types of plumes must be due to natural variability.

3.3 Some simple plots

Figure 6 shows $\overline{H}$ plotted against the average windspeed at 2 meter height. It turns out that all the points, both HF, smoke and HF with butane, lie on a fairly narrow strip. At windspeeds above 4 m/s it appears that $\overline{H}$ is constant while it increases as $U(2\mathrm{m})$ decreases below 4 m/s. The constant value at high windspeeds is what is expected for a passive plume in neutral conditions. The consistency of

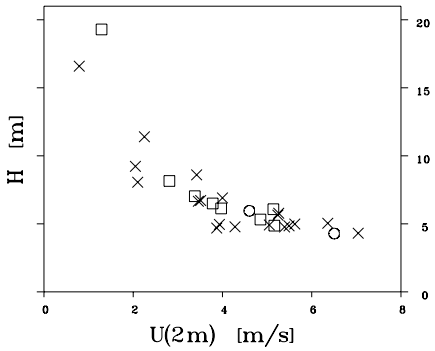

Figure 6. The average plume height plotted against the average wind speed at 2m level. ×: smoke, □: HF, ○: HF with butane.

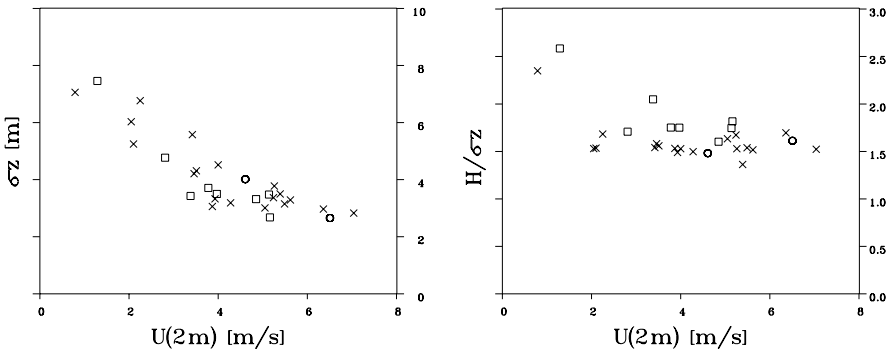

Figure 7. The average plume thickness σ_z (left) and $\sigma_z/\overline{H}$ (right) plotted against the average wind speed at 2m level. ×: smoke, □: HF, ○: HF with butane.

the value measured average plume heights for $U(2\text{m}) > 4\text{m/s}$ is quite remarkable. The standard deviation of $\overline{H}$ for the 15 releases with $U(2\text{m}) > 4\text{m/s}$ is only 3%.

For the passive plume the higher values of $\overline{H}$ at low windspeeds must be due to convection. Convection also affects HF plumes in addition to buoyancy effects. In general the atmosphere is more unstable at lower wind speed and high insolation. For the present dataset the low wind speeds occurred mainly on sunny days while the high wind speeds occurred on cloudy days, therefore there might be a stronger correlation between stability and windspeed in the data than could otherwise be expected. Whatever the reason, the data points lie on a narrow strip closely together with the HF data points. This indicates that the buoyancy effect in the HF clouds was small compared to the effect of atmospheric convection.

Figure 7 shows similar plots for the cloud thickness σ_z and the ratio $\overline{H}/\sigma_z$, which can be regarded as an indicator of the degree of lift-off. It could be argued that $\overline{H}/\sigma_z$ tends to be slightly larger for HF than for smoke, but it is not much in any case.

3.4 Surface layer scaling

In order to make a possible difference between the HF plumes and the passive plumes more clear we introduce surface layer scaling (or Monin-Obukhov scaling). The idea is to make plots where data points for the smoke releases (are supposed to) lie on a curve, and see if the HF data points are outliers. The advantage of the procedure is that it compensates differences in the meteorological conditions between the HF and the smoke releases. The disadvantage is the introduction of meteorological parameters based on flux measurements, which are difficult to measure accurately and for which average values inevitably suffer from short averaging times.

Surface layer scaling is based on flat and uniform terrain and is confined to the constant flux layer, i.e. the lower part of the boundary layer characterized by constant values of vertical fluxes of horizontal momentum, heat and water vapour. The constant flux layer excludes the region next to the surface, where the flow is directly influenced by roughness elements. The water vapour only plays a role if it is condensing, which is not the case here, hence the momentum flux, quantified by the friction velocity $u_* \equiv \sqrt{-\langle uw \rangle}$, and the sensible heat flux $\langle T'w \rangle$ characterize the layer. The influence of the earth's rotation is assumed to be negligible, the Reynolds number is assumed to be effectively infinite, and the Boussinesq approximation is adopted (i.e. constant density, but with temperature fluctuations acting as a sort of buoyancy 'charge' analogous with a massless electric charge acted upon by a constant electric field).

The governing equations, based on these assumptions, can be brought to a simple form if lengths are scaled with (the absolute value of) the Monin-Obukhov length scale L, time is scaled by the timescale $|L|/u_*$ and temperature fluctuations are scaled with $T_* \equiv \langle T'w \rangle / u_*$. L is defined as

$$L \equiv -\frac{{u_*}^3 \langle T \rangle}{\kappa g \langle T'w \rangle}, \tag{17}$$

where $\langle T \rangle$ is the absolute temperature at some reference height, g is the acceleration of gravity and $\kappa \approx 0.4$ is the von Karman constant. The point is that the scaled equations come in just two versions: one for stable conditions ($L > 0$) and one for unstable conditions ($L < 0$). Neutral conditions are obtained as the limiting case where $L \to \infty$. In non-dimensional form the friction velocity and the heat flux, i.e. the boundary conditions, are both equal to 1. Actual, dimensional values are obtained by substituting the values of the scales into the scaled solutions. This determines the velocity and temperature fields except for average values at a reference height. For the temperature this is simply a matter of adding a constant, while u is fixed by a suitable Gallilei transformation, i.e. the substitution $u(x, y, z, t) \to u(x + u_o t, y, z, t) - u_o$, where u_o is the velocity difference for the two reference systems. This means that we may end up in a coordinate system in which is the ground is moving, which is of course seldom the case. However, the basic assumption is that turbulence is independent of the friction mechanism, and, as long as the value of u_* is the same, it does not matter whether friction is provided by a ground moving like a conveyor belt or by static roughness elements. It is usual to specify the average windspeed at the 10 meter level, but it is convenient here to specify the height z_0, where the average wind speed is zero (actually z_0 is usually below the constant flux layer, and z_0 is determined by extrapolation). Therefore z_0 is somewhat arbitrary since we may change it a transformation to a frame of reference moving parallel with the mean wind direction. This will not change statistics Gallilean invariant quantities which are therefore independent of z_0.

An ideal passive scalar is obtained by 'marking' parts of the fluid without dis-

turbing the flow. Surface layer scaling includes dispersion of ideal scalars, since this is fully described by the statistics of trajectories of selected fluid particles. An ideal passive source therefore simply marks all fluid that passes through it, while an ideal instantaneous source marks the fluid in side it only at a single moment in time. Gallilean invariance is a problem for continuous releases, because the setup for a continuous release experiment transforms into a continuous release with a moving source. Instantaneous puff releases are more elegant, because they transform into puff releases. This means that similarity solutions exists for puffs and that Gallilean invariants of puffs obey surface layer scaling. The invariants include geometric measures such as the puff width σ_p and the mean centroid elevation $\overline{H}_p$, but not e.g. the downwind distance to the puff centre. Thus for $\overline{H}_p$ we have

$$\frac{\overline{H}_p(t)}{u_* t} = F_p\left(\frac{u_* t}{|L|}, \frac{\overline{H}_p(0)}{u_* t}\right), \tag{18}$$

where t is time since the release, $\overline{H}_p(0)$ is the initial release height and F_p is a non-dimensional universal function with two arguments (actually there are two functions, one for $L < 0$ and one for $L > 0$, but the present experiments were all made during unstable conditions). It is convenient[1], and permissible, to scale $\overline{H}$ with $u_* t$ rather than with L. Sufficiently long time after the release the puff has forgotten its initial height and

$$\frac{\overline{H}_p(t)}{u_* t} = F\left(\frac{u_* t}{|L|}\right). \tag{19}$$

where $F(x) = F_p(x, 0)$.

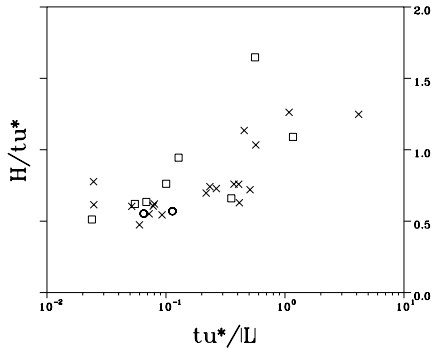

Figure 8. Non-dimensional plume height plotted against the non-dimensional downwind distance. ×: smoke, □: HF, ○: HF with butane.

In the neutral limit $L \to \pm\infty$ equation reduces to

$$\frac{\overline{H}_p(t)}{u_* t} = C_1 \quad \text{for} \quad u_* t/|L| \to 0 \tag{20}$$

where $C_1 = F(0)$.

There is another important exact result for $L \to -0$. This limit can be achieved by stopping the wind so that $u_* \to 0$ while keeping the sunshine so that $\langle Tw \rangle / T$ is constant. In other words, this is the limit of free convection, where turbulence is powered mainly by the heat flux and friction is of no importance. For fixed heat

[1] L varies considerably more than other quantities. Therefore $\overline{H}/|L|$ is always strongly correlated with $u_* t/|L|$ simply because the common factor $1/|L|$ dominates the other factors.

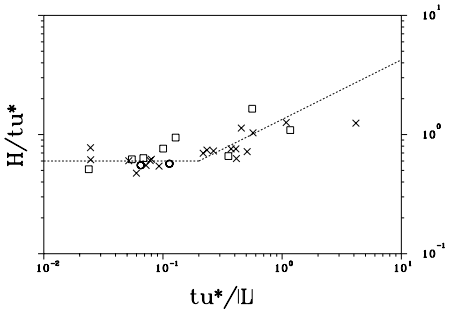

Figure 9. Essentially the same plot as in figure 8. ×: smoke, □: HF, ○: HF with butane. The dotted lines correspond to equations 20 and **??** *with* $C_1 = 0.6$ *and* $C_2 = 1.5$.

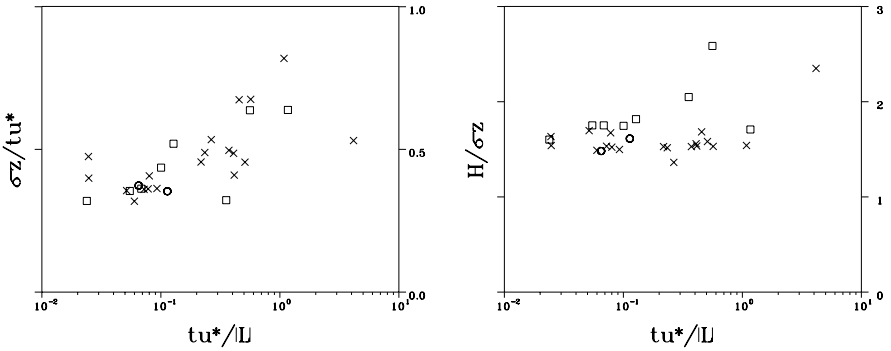

Figure 10. Non-dimensional plume thickness (left) and lift-off indicator $\overline{H}/\sigma_z$ *plotted against the non-dimensional downwind distance. ×: smoke, □: HF, ○: HF with butane.*

flux ($\langle Tw \rangle$), L is proportional to u_*^3 and the only way $\overline{H}$ can become independent of the friction velocity is if $F(\xi)$ is proportional to $\xi^{\frac{1}{2}}$. It therefore follows that

$$\frac{\overline{H}_p(t)}{u_* t} = C_2 \sqrt{\frac{u_* t}{|L|}} \quad \text{for} \quad u_* t/|L| \to \infty \tag{21}$$

for free convection. The value of C_2, characterizing the onset of free convection, is uncertain. Monin and Yaglom (1975) suggest that C_2 is 'several tenth'.

A plume can be regarded as a series of puffs and, although it is not a simple consequence of the equations, it seems plausible to assume that the plume width at a certain downwind distance x is equal to the width of a puff at time $t = x/U_t$, where U_t is a suitable travel speed. Table 5 shows measured values of U_t and $U(2\text{m})$. U_t was measured by timing the arrival of the leading edge of the plume at the 100m downwind distance. The arrival is seen on the lidar data as a fairly sharp change of mass in the cross-plume slice (see figure 4, allowing the travel time to be estimated to within a few seconds. The table shows that U_t does not differ much from $U(2\text{m})$. Assuming further that the dependence of the release height can be neglected, the analogy between puffs and plumes yields

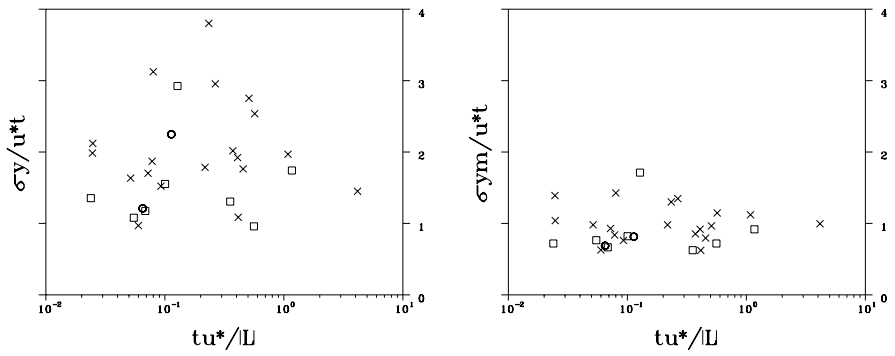

Figure 11. Non-dimensional plumewidth plotted against the non-dimensional downwind distance. Left: fixed frame. Right: moving frame. ×: smoke, □: HF, ○: HF with butane.

$$\frac{\overline{H}(x)}{u_* t} \approx F\left(\frac{u_* t}{|L|}\right), \tag{22}$$

where $t \equiv x/U(2\text{m})$, and $x = 100$ m. The group $u_* t/L$ can be seen either as a non-dimensional downwind distance or as a measure of atmospheric stability. Figure 8 shows a tendency for the passive smoke measurements to form a curve. Moreover, the HF data point are similar to the smoke data except, perhaps, for one data point which lies above the others. This data point is for trial HF012.

The data are consistent with the value $C_1 \sim 0.6$. This is close to the value $C_1 \sim 0.45$ suggested by e.g. Monin and Yaglom (1975).

Yaglom (1969) points out that the change from the logarithmic to the $(z/|L|)^{-\frac{1}{3}}$ behaviour for the average temperature profile (and similar for the windspeed), marking the transition to the free convection regime, is very sharp and sets in already at $z/L \sim -0.1$. A similar sharp transition to a convective regime could therefore expected for $\frac{\overline{H}}{u_* t}$ when plotted against $\frac{u_* t}{|L|}$. From the present data it seems that something happens at $\frac{u_* t}{|L|} \sim 0.2$, where $\frac{\overline{H}}{u_* t}$ changes from relatively constant values to larger and much more scattered values. We interpret this as a the transition to free convection, although a behaviour according to equation **??** is not clear. Taking the transition to be at $\frac{u_* t}{|L|} = 0.2$ we get the estimate $C_2 \sim 1.5$. In figure 9 we have plotted same the data as in figure 8, but with logarithmic ordinate and dotted lines indicating the behaviour in the two regimes. Although the figure is essentially a re-plot of figure 8 it is not obvious from figure 9 that Trial HF012 should an outlier. In fact the point at the far right (HF012S1, the smoke release following HF012) appears to be more out of place.

Similar plots for $\frac{\sigma_z}{u_* t}$, $\frac{\sigma_y}{u_* t}$, $\frac{\sigma_{ym}}{u_* t}$ and $\frac{\overline{H}}{\sigma_z}$ are also shown. The non-dimensional plume thickness $\frac{\sigma_z}{u_* t}$ does not appear to different for HF compared to smoke (figure 10 left). The arguments leading to (20) and (20) should also apply to $\frac{\sigma_z}{u_* t}$, and the plot indeed look very similar to figure 8.

For $\frac{\overline{H}}{\sigma_z}$ the HF and the smoke data point are also close with a tendency for the HF values to be slightly higher than the smoke points (figure 10 right).

For the moving frame width $\frac{\sigma_{ym}}{u_* t}$ and for the (less well behaved) fixed frame width $\frac{\sigma_y}{u_* t}$ there is also no difference. Interestingly $\frac{\sigma_{ym}}{u_* t}$ is fairly constant and independent of stability (figure 11). Judged from the plume width and thickness there is no detectable enhanced mixing effect of HF. There is a tendency for the HF plumes to be slightly narrower than the smoke plumes, which could, however,

be explained by differences in the backscatter characteristics of the two types of aerosols.

Table 5. Measures travel velocities of the cloud front compared to wind speeds at 2m

Trial	U_t	U(2m)
HF003	3.3	3.8
HF004	4.8	5.2
HF005	4.1	4.9
HF006	4.5	5.1
HF007	3.1	3.4
HF008	2.8	2.8
HF009	4.6	6.5
HF010	3.9	4.0
HF011	4.1	4.6
HF012	1.3	1.3

3.5 Vertical concentration profiles

The vertical average concentration profiles are shown in plots for each trial in Appendix B. In all except two cases the concentration is a decreasing function of height so that the maximum average concentration is found at the ground. This clearly excludes a lift-off. The two exceptional cases are HF012 (HF) and HF012S1 (smoke), where the maximum concentration does not occur at the ground. If we accept this as a sign of lift-off then lift-off occurred both for HF and smoke (we recall that the plumes were observed to be on the ground at a distance of about 1km). The lift-off of the smoke was definitely due to convection. Therefore convection must have been partly responsible for the observed lift-off of the HF cloud. The difference of the centroid heights is only 2.7m, which is small compared to $\overline{H}$=19.3m for HF012. However, HF012S1 is more convective than HF012 and the release conditions do not match very well. In figure 8 HF012S1 is represented by the point most to the right, which seems to be consistent with the trend of the other points. HF012S1 corresponds to the highest point in figure 8, which is definitely above the other points. The difference corresponds to an excess height in HF012 of about 8m.

3.6 Concentration estimates

As already mentioned the lidar output is the extinction, not the concentration. In this section we make an attempt to convert to HF concentrations. Some assumptions have to be made. First we assume a linear relation between extinction and concentration. This is justified if either backscatter from HF-water droplets is small compared to backscatter from NH_4F aerosol or if the ratio between the two is constant. The NH_4F aerosol most probably consists of droplets unless the humidity is very low. Both NH_4F and HF droplets will tend to be larger at high humidity, but the influence is largest on the HF droplets. In most of the experiments there probably were no HF droplets 100m downwind where the lidar was measuring, and a linear relation between HF concentration and extinction can be safely assumed. Figure **??** shows a plot of the relative amount of liquid in adiabatic mixtures of HF with humid air. It is noted that for a wide range of concentrations the liquid mass is of the same order of magnitude as the mass of the HF. At

intermediate concentrations the liquid mass goes rapidly to zero, and below a certain concentration the liquid phase has evaporated. In the first regime the aerosol mass is about 100 times larger than the mass of NH_4F aerosol. The high aerosol content excludes the first regime, since the aerosol would surely have blocked the laser beam. The rate of the NH_3 was chosen so as to produce NH_4F aerosol in similar amounts as the smoke from the smoke machine, and the observed optical depths are in fact not very different. Therefore the amount of HF droplets at 100 meter must have been limited. Model calculations also show that the amount of HF aerosol is small in all cases. We therefore assume that backscatter was mainly due to NH_4F and adopt a linear calibration.

HF readily deposits on humid soil and plants, and spilling of liquid HF on the ground in front of the source was observed. The resulting loss of HF cannot be estimated from measurements. A mass balance based on concentration measurements has been made (Nielsen, Ott, Jørgensen, Bengtsson, Nyrén, Winter, Ride and Jones 1997) for the FLADIS ammonia releases. These releases were made over grass and with similar release rates as in Porton. The loss of ammonia by deposition was estimated to be less than 10%. Anhydrous ammonia is very hygroscopic and resembles HF in this respect. The relatively small loss of ammonia by deposition therefore indicates a small loss of HF. We therefore ignore loss of HF by deposition. This leads to an overestimate of the concentrations, but the error is only large if a very substantial fraction of the HF was lost by deposition.

The conversion factor between extinction and concentration can be estimated by means of an estimated mass balance, viz.

$$\dot{m} = \int_0^\infty \mathrm{d}z \int_{-\infty}^{\infty} \mathrm{d}y \ \langle \rho C U \rangle \sim \int_0^\infty \mathrm{d}z \int_{-\infty}^{\infty} \mathrm{d}y \, \rho_a \langle C \rangle \langle U \rangle \tag{23}$$

Here C is the mass–by–mass HF concentration. The average wind profile $\langle U(z) \rangle$ can be extracted from the cup anemometer data, and is in all cases well represented by a logarithmic profile. The HF release rate $\dot{m}$ was measured directly at the source rig. Since HF concentrations are low at 100m the density is close to a constant value ρ_a. In the estimate the turbulent diffusion term $\langle u'C' \rangle$ has been neglected. Using $\sigma_u \ \langle C \rangle$ as an upper bound of the magnitude of this term we find that is contributes with at most 20%. Furthermore $\langle u'C' \rangle$ is generally negative. Neglecting turbulent diffusion therefore leads to a slight overestimate of the concentration.

Another source of error is introduced in cases where the lidar scan angle did not entirely cover the plume. The distance between lowest beam and the ground is approximately 1.5m varying ±0.5m due to the uneven the terrain. This was accounted for by assuming $\langle C \rangle$ to be constant below 1.5m. No corrections were made for losses at the top of the scan angle. Here the coverage is generally very good even if the upper edge of the plume occasionally was lost during some of the trials. It is only during HF012 that a major part of the plume seems overshoot the lidar scan angle, and perhaps as much as half of the plume is lost for about ten second. For this reason the concentrations estimates for HF012 are more uncertain than for the other trials.

One of the arcs of impregnated filter samplers was placed 100m downwind of the source. The estimated average (fixed frame) HF concentrations at approximately the same positions are shown in table 6 below. A comparison with preliminary data from the samplers show good agreement with respect to centre position and width of the profiles. The concentrations obtained from the two methods are mostly within a factor 2. The lack of point-by-point agreement can probably be explained by differences in sampling periods and the fact that the lidar points are not exactly coincident with the sampler positions (the lidar measures along a line while the samplers were placed on a circular arc). The obtained ground level

profiles are far less regular than e.g. the depth integrated profiles. It therefore seems that the short sampling time introduces a considerable variance in these measurements. Comparing the obtained maximum concentrations we find good agreement: on average the lidar estimates are only 5% lower than the those based on filter samplers. Figure 12 shows the calculated Lidar concentrations based on the estimated massbalance compared with the HF filter measurements.

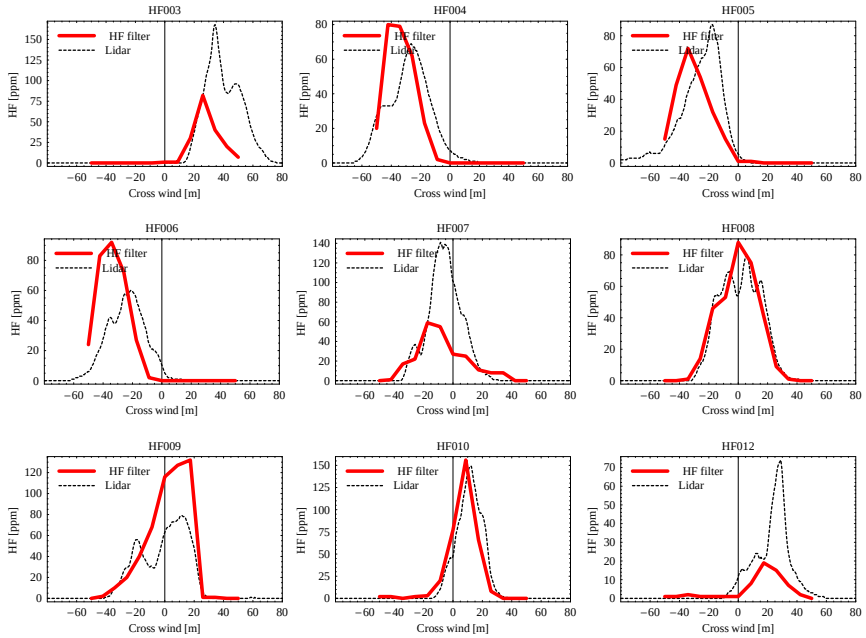

Figure 12. Calibrated Lidar measurements compared to the measurements based on the HF filters across the plume at 100 meter downwind.

Moving frame concentrations have also been estimated. Table **??** shows maximum moving frame average concentrations at 1.5m and global maxima. In most cases the two are identical and only HF012 shows a substantial difference.

Table 6. Estimated fixed frame average concentrations near the sampler positions. In all cases x=100m and z=1.5m and θ is measured in degrees from magnetic North. The values are in ppm.

y [m]	-50.0	-42.3	-34.2	-25.9	-17.4	-8.7	0.0	8.7	17.4	25.9	34.2	42.3	50.0
HF003	0	0	0	0	0	0	0	0	18	81	168	85	95
HF004	28	33	45	68	50	23	7	3	1	0	0	0	0
HF005	11	25	44	64	87	36	6	0	0	0	0	0	0
HF006	6	21	41	57	54	25	10	1	0	0	0	0	0
HF007	0	0	2	37	59	140	101	63	15	4	0	0	0
HF008	0	0	0	10	48	65	55	63	55	15	2	0	0
HF009	0	0	10	29	53	30	63	75	62	6	0	0	0
HF010	0	0	0	0	0	11	48	129	102	26	2	0	0
HF011	0	0	0	0	0	0	0	0	2	8	4	12	50
HF012	0	0	0	0	0	1	12	19	21	66	24	9	3

Table 7. Estimated maximum average moving frame concentrations at the $z = 1.5$ meter level and global maxima. The values are in ppm.

Trial	$C_{\max}$ @ 1.5m	$C_{\max}$
HF003	253	253
HF004	133	133
HF005	143	144
HF006	111	111
HF007	216	240
HF008	146	188
HF009	178	178
HF010	212	240
HF011	156	156
HF012	67	227

3.7 Overlap test

The height of the centroid is the most important parameter for determination of buoyancy effects. Each successful trial produces a pair of time series, $H_1(t)$ (HF) and $H_2(t)$ (smoke) (for some of the trials there are more than one smoke series). The idea is to quantify the difference/similarty of such a pair of time series in a simple way.

The average height $\overline{H}$ is given by (8) which may also be written as

$$\overline{H} = \frac{1}{T}\int_0^T H(t)\,\mathrm{d}t \tag{24}$$

where T is the duration of the sampling period and t is time counted from the start of the time series. We may also form the spread of the data $D(T)$, i.e.

$$D^2(T) \equiv \frac{1}{T}\int_0^T (H(t)-\overline{H})^2\,\mathrm{d}t = \frac{1}{2T^2}\int_0^T \mathrm{d}t \int_0^T \mathrm{d}t'\,(H(t)-H(t'))^2 \tag{25}$$

The second equality follows directly from the definition of $\overline{H}$. About two thirds of the observations will belong to the interval $\overline{H} \pm D$. If the intervals for the two series overlap we may say that the two time series are not distinctly different. No overlap means that in that one is almost always larger than the other. An even more direct approach is to count pairs of observations $(H_1(t), H_2(t'))$ with $H_1(t) > H_2(t')$ and express this as a fraction F of the total number of pairs, i.e.

$$F \equiv \frac{1}{T_1 T_2}\int_0^{T_1} \mathrm{d}t \int_0^{T_2} \mathrm{d}t'\,\theta(H_1(t)-H_2(t')) \tag{26}$$

where θ is the Heavyside step function ($\theta(x) = 0$ for $x < 0$ and 1 for $x < 0$). This is a test of whether the observed difference is substantial compared to the variability. We emphasize that this is not a test of the significance of the difference between the observed *average values* $\overline{H}_1$ and $\overline{H}_1$.

Table 8 shows the results for the trials. The average heights[2] are strikingly similar, even if the HF plumes are slightly higher than the smoke plume in most cases. The only possible exception is HF012, where the height of the HF cloud might be significantly higher than the smoke plumes.

The test shows that the range of $H(t)$ for an HF plume generally overlaps the range of $H(t)$ for the corresponding smoke plumes. The same conclusion can be drawn from the calculated values of F, which generally do not differ much from 0.5. Again Trial 12 is an exception with values of F larger than 0.9 for HF012S3 and HF012S4.

For trial 12 it should be realized that none of the smoke releases match the HF release in terms of meteorology. In HF012S1 the wind speed is extremely low and it decreased during the release. Actually the release was abandoned when the windspeed dropped to almost zero and the wind turned. From the plots in Appendix B it is evident that there is a change of weather conditions between HF012S1 and HF012S2. In the last three later smoke releases the windspeed is almost twice as large as during the HF release. Due to the changing conditions it is probably best not to regard the smoke plumes in trial 12 as repeats of HF012.

[2]The values of $\overline{H}$ in Table 8 differ slightly from values found elsewhere in this report. This is because $H(t)$ was calculated without first interpolating concentrations in a rectangular coordinate system.

Table 8. Results of the overlap test

Trial	Plume	$\overline{H}$ [m]	D [m]	Overlap?	F [–]
HF003	HF	6.46	2.47		
HF003S1	smoke	5.08	2.04	yes	0.67
HF004	HF	4.76	1.43		
HF004S1	smoke	5.03	1.66	yes	0.46
HF004S2	smoke	4.36	1.71	yes	0.61
HF005	HF	5.23	2.35		
HF005S1	smoke	4.82	1.85	yes	0.55
HF005S2	smoke	4.93	1.97	yes	0.53
HF006	HF	5.86	2.43		
HF006S1	smoke	5.77	2.21	yes	0.50
HF007	HF	6.59	2.42		
HF007S1	smoke	7.08	3.58	yes	0.49
HF008	HF	8.26	3.66		
HF008S1	smoke	6.97	3.05	yes	0.60
HF008S2	smoke	6.69	2.84	yes	0.62
HF008S3	smoke	8.54	4.51	yes	0.50
HF009	HF+butane	4.56	1.76		
HF009S1	smoke	6.07	2.68	yes	0.32
HF009S2	smoke	5.03	2.71	yes	0.50
HF009S3	smoke	5.36	2.22	yes	0.39
HF010	HF	6.33	2.22		
HF010S1	smoke	5.50	2.04	yes	0.63
HF010S2	smoke	5.06	1.94	yes	0.69
HF011	HF+butane	6.21	2.68		
HF012	HF	18.88	4.21		
HF012S1	smoke	16.33	4.52	yes	0.67
HF012S2	smoke	11.39	5.28	yes	0.86
HF012S3	smoke	8.18	3.82	no	0.96
HF012S4	smoke	9.68	4.25	no	0.93

4 Conclusions

The experimental Campaign was successfully completed. The meteorological mast worked well with few cases of failing instruments. Twelve HF releases were made during which the lidar system was operational. The first two trials were used to calibrate the lidar. In the remaining ten trials the lidar measured concentrations in a vertical 2D cross-plume slice located 100m downwind of the source. In nine of these trials the HF releases were supplemented by passive smoke releases. A total of 19 passive smoke releases were made (plus two made for calibration purposes).

The lidar data have been analyzed in several ways in order to detect a difference between the HF plumes and the smoke plumes.

Simple plots of plume height, thickness and width versus windspeed show a nice collapse, which might, however, be fortuitous since high wind speeds are coincident with heavier cloud cover in this particular dataset. The plots show a high degree of consistency for near neutral conditions (the 15 releases with $U > 4$m/s), where the standard deviation of experimental values of $\overline{H}$ is only 3%. This high degree of reproducibility indicates that the sampling time was adequate for the determination of $\overline{H}$.

The ratio $\overline{H}/\sigma_z$ can be regarded as a lift-off indicator. For the present data it is generally slightly larger for the HF plumes without butane compared to the smoke plumes, but it is not more than a few percent.

Surface layer theory has been employed in order to obtain universal plots for passive plumes and to see if the HF data points would follow the trend of the passive releases. The plots show that the plume centroid is generally not affected by HF except for HF012, where $\overline{H}$ is about 8m higher than the trend for the passive plumes. This accounts for about half of the observed plume rise, while the remaining half must be due to convection.

Horizontal, depth integrated average concentration profiles were obtained in two ways by the conventional fixed frame method and by the moving frame method. The moving frame method removes the effect of meandering from the data. The moving frame profiles are fairly random and meandering of the plume centre typically accounts for 80-90% of the width. The fixed frame profiles are all bell-shaped and symmetric, and they are considerably narrower than the fixed frame profiles. For the 15 releases done in near neutral conditions the standard deviations of σ_y is 22% while it is 12% for σ_{ym}.

Most of the vertical, cross-plume integrated, average concentration profiles have similar shapes characterized by a decrease of the concentration with height. HF012 and HF012S1 are exceptional in that maximum average concentration is located about 20m above the ground. This can be taken as a sign of lift-off. The two releases were done in succession and the fact that lift-off occurred even for the passive smoke indicate that convection must have played a major role.

The meteorological record of trial 12 shows that conditions were changing, in particular during and right after the first smoke release HF012S1. Therefore the surface layer must have been in a state of transition, which might have influenced the dispersion of both the HF and the smoke plumes. It is also possible that the observed plume rise was caused by a pool of cold air still in the bowl, but not at the met-mast. We also note that the elevated position of the maximum concentration is a characteristic of passive ground releases in convective conditions (G. E. Willis 1976).

Time series of the instantaneous centroid elevation, $H(t)$, are characterized by large fluctuations. For all pairs of releases there is a considerable overlap of the ranges of $H(t)$. The small differences between the mean values for smoke and HF plumes are therefore generally masked by much larger fluctuations induced by the

atmospheric turbulence.

Our main conclusion is that meteorological conditions seem to have had a larger impact on the dispersion of the observed HF plumes than the effects of HF thermodynamics. Of the 29 analyzed releases only two showed signs of lift-off and one of them was a passive smoke release. The measurements of plume width and thickness show no evidence of enhanced mixing in the HF plumes.

Since not much lift-off was observed, it is natural to ask if lift-off would have occurred with larger release rates. When the humidity is so low that buoyant mixtures do not exist there is of course no effect, hence we can limit the discussion to cases where buoyant mixtures do exist. The possibility of enhanced lift-off of a larger plume depends on stability. Because of its size a larger plume more easily overcomes the ambient fluctuations than a smaller one, but it also extends higher up into the boundary layer where the turbulent eddies are larger. In the extreme case of pure free convection these two trends balance and there is no effect of increasing the release rate. In neutral or moderately convective conditions the first trend is more important, i.e. larger plumes should exhibit a more 'clean' lift-off than smaller one. Although convection was clearly influencing some of the releases, we believe that the plumes produced in the field all fall into the second category, where the release rate makes a difference. It is difficult to say how much the release rate would have to be increased in order to see a clear effect and the answer would depend on the atmospheric conditions. However, some guidance can be obtained by applying scaling laws to the releases. D. J. Hall (1997) has reviewed scaling of HF releases and conclude that Froude scaling is appropriate. Only weak and generally accepted assumptions are required, and hence it is permissible to regard a small release as a down-scaled version of a larger one. The release rate scales with the factor $S_c^{5/2}$, the windspeed (and u_*) with the factor $S_c^{1/2}$, and the Monin-Obukhov length, the roughness length and other lengths scale with the factor S_c. The large scaling factor associated with the release rate indicates that a substantial increase of the release rate is required in order to make a large difference. We also note that the 'clearness' of lift-off must be invariant under scaling, for any sensible definition of this concept. Hence scaled up versions of the experimental releases *do not* exhibit clearer buoyancy effects. Scaling the obtained results we can in fact rule out lift-off for a wide range of meteorological conditions for larger releases. It should be noted that the scaling applies to release rate as well as L, z_0 and u_*. In general an up-scaled version of a release therefore corresponds to a larger wind speed and is it closer to neutral than the original. The main advantage of making a larger release is therefore that it is made at lower windspeeds than the corresponding scaled windspeed of a scaled experiment. In order to illustrate this we summarize the observations roughly by stating that buoyancy effects are insignificant for 0.1 kg/s HF releases when the relative humidity is less than 90% and the windspeed is above 2 m/s. Using scaling we may infer from this that 10 kg/s releases show insignificant buoyancy effects when the relative humidity is less than 90% and the windspeed is above 5 m/s. Conversely, the behaviour of a 10 kg/s release at lower windspeeds than 5 m/s is not covered by this experiment, and the results do not rule out the possibility of lift-off for such a release.

References

Bohren, C. and D.R., H.: 1983, *Absorpation and Scattering of Light by Small Particles*, John Wiley & Sons.

D. J. Hall, S. W.: 1997, Scaling rules for reduced-scale field release of hydrogen flouride, *Journal of Hazardous Materials* **54**, 89–111.

Evans, B.: 1988, Sensitivity of the backscatter/extinction ratio to changes in the aerosol properties: implication of lidar, *Appl. Optics* **27**, 3229.

G. E. Willis, J. W. D.: 1976, A laboratory model of diffusion into the convective planetory boundary layer, *Quart. J. Roy. Meteor, Soc.* **102**, 427–445.

Jørgensen, H. E. and Mikkelsen, T.: 1993, Lidar measurements of plume statistics, *Boundary-Layer Meteorol.* **62**, 361–378.

Jørgensen, H. E., Mikkelsen, T., Streicher, J., Herrmann, H., Werner, C. and Lyck, E.: 1997, Lidar calibration experiments, *Appl. Phys. B* **64**, 355–361.

Measures, R. M.: 1984, *Laser Remote Sensing- Fundametals and applications*, John Wiley & Sons.

Monin, A. S. and Yaglom, A. M.: 1975, *Statistical Fluid Mechanics*, Vol. 2, The MIT Press.

Nielsen, M., Ott, S., Jørgensen, H. E., Bengtsson, R., Nyrén, K., Winter, S., Ride, D. and Jones, C.: 1997, Field experiments with dispersion of pressure liquefied ammonia, *J. Hazard. Mater.* **56**, 59–105.

Yaglom, A. M.: 1969, Lagrangian turbulence characteristics in a diabatic atmospheric layer and in convective jets, *Izvestiya AN SSSR,Sr. fiz. atmos. i okeana* **1**, 157–166.

A Instrument specifications

This appendix contains brief descriptions of the applied meteorological instruments as presented by the manufacturer, including calibration procedures, known systematic errors etc.

A.1 The lidar system

The lidar system consists of

System components

- A water cooled pulsed laser
- A telescope with a detector
- Stepper motors and controllers that can turn the telescope
- A storage scope used for digitization
- A PC used for control and data acquisition
- A 220V AC power generator
- A van to contain it all

The lidar is used to detect aerosol concentrations in the atmosphere. It is sensitive enough to detect the natural aerosol background or clouds, but here it is used to measure smoke particles. It works much like a conventional radar except that it uses a pulsed infrared laser beam instead of radio waves. A short (2 meter long) light beam is emitted by the laser and the echo is recorded by the storage scope. The position is given by the time delay of the echo and the strength of the echo is proportional to the number of aerosol particles at that position. One pulse produces up to 500 sampling points along the beam path. The detector and the laser are built into the telescope. The telescope (with laser and detector) can be turned along two axes by means of stepper motors. In the experiments the telescope was moved up and down in order to scan a vertical plane across the plume. Each scan consists 20 laser shots covering angles between 0° and 10° (sometimes a smaller angle was used). Each scan is typically less than 1 sec and with a pause of approximately 1.5 seconds between the scans. The pause is used to decelerate and accelerate the telescope and to transfer data to the PC.

Principle of operation

In the experiments the spatial separation of the sampling points was always 0.75 m, which is a slight oversampling compared to the length of the light pulse and the resolution of the detector. The detector consists of an avalanche diode and a preamplifier. A first order low pass filter time sets the limit of the spatial resolution to about 2 meter.

Detection and sampling

Interpretation of lidar measurements is based on the theory of propagation of electro-magnetic radiation and attenuation in an optically dense media (here the polluted atmosphere) in combination with scattering from distributed targets. The so-called "lidar equation" accounts to first-order for this complex process: The backscatter lidar principles can be formally expressed by the single-scattering lidar equation:

The lidar equation

$$P(r) = P_0 \left(\frac{c\tau}{2}\right) F(r)\, A_t\, \frac{1}{r^2}\, \beta(r)\, \mathrm{e}^{-2\int_{r_0}^{r} \kappa(r')\mathrm{d}r'} \tag{A.27}$$

$P(r)$ is the power received from the range $r = ct/2$, where c is the speed of light. The factor 2 arises from the traveling of the laser beam to the distance r and back to the receiver. P_0 is the power transmitted at time t equal to zero. The effective length of the laser pulse is specified as $\frac{c\tau}{2}$. The telescope area is A_t, and divided by r^2 this term defines the "solid angle acceptance $[sr]$". The coaxial design with the laser in front of the telescope results in a geometric overlapping function, $F(r)$, which relates the receiver field of view of the telescope to the width of the laser pulse, (Measures 1984). The quantity $\beta(r)$ $[sr^{-1}m^{-1}]$ is the volume backscattering coefficient of the atmosphere at distance r, and $\kappa(r)$ $[m^{-1}]$ is the volume extinction coefficient in the atmosphere.

The volume backscattering coefficient β is defined here as the fraction of incident energy scattered per solid angle in the backward direction (180°), per unit length. The volume extinction coefficient κ represents the fraction of the energy flux removed in the propagation direction.

Both the backscatter and the extinction properties depend on parameters such as wavelength, particle size distribution, and the optical properties of the media, see e.g. (Measures 1984).

The last term in the lidar equation represents the attenuation through the atmosphere known as Beer's law. The attenuation, along the two-way pulse path between the lidar and the range r, is defined as:

$$T(r) = \mathrm{e}^{-2\int_{0}^{r} \kappa(r')\mathrm{d}r'} \tag{A.28}$$

The lidar equation (A.27) applies to a medium where single scatter on a particle is responsible for the backscattered light. The lidar equation compensates for

damping of the laser light due to: 1) absorption by particles, 2) range dependency, and 3) the optical geometry of the transmitter and receiver units.

Raw data processing

The raw signal is scaled with the laser energy and a factor that compensates for the view of the optical system and the $1/r^2$ dependence. The result is the so-called signature $S(r)$

$$S(r) = \frac{P(r)r^2}{K_{\text{sys}}} \tag{A.29}$$

$$K_{\text{sys}} = P_0(\frac{c\tau}{2})A_t F(r) \tag{A.30}$$

$$S(r) = \alpha\kappa(r)\mathrm{e}^{-2\int_{r_0}^{r}\kappa(r')\mathrm{d}r'} \tag{A.31}$$

which indicates the intensity of back scattered light at position r. For optically thin clouds $S(r)$ is proportional to the density of aerosol particles at position r. If the background aerosol level is low S is therefore proportional to the cloud concentration. For optically thick clouds it is necessary to make corrections for the extinction (the attenuation by diffuse scatter on particles). The extinction (measured in m^{-1}) can be assumed to be proportional to the density of aerosol particles and hence proportional to concentration. The correction is made by solving equation A.29.

$$\kappa(r) = \frac{S(r)}{C - 2\int S(r)\mathrm{d}r} \tag{A.32}$$

Backscatter to extinction ratio

The single-scatter lidar equation (A.27) is a first order integral equation with two unknown quantities. To solve the equation for κ or β a simple relationship between the backscatter and extinction is introduced.

Assuming spherical particles and elastic scattering (no shift between the received and transmitted wavelength, respectively), Mie theory can be applied to obtain a basis for such a relationship, (Bohren and D.R. 1983). Mie theory describes the scattering of light from spherical particles of a known index of refraction with a size comparable to the wavelength. The intensity of the backscatter light here is proportional to the number of particles per unit volume, or the particle density (in the following assumed to be concentration). The concentration can therefore be related proportionally to the backscatter intensity. The backscatter coefficient per unit volume is here expressed as:

$$\beta = \int_0^\infty \pi a^2\, \mathrm{Q}_{\text{back}}(\lambda, m, a)\, \mathrm{N}(a)\, \mathrm{d}a \tag{A.33}$$

The backscatter cross-section efficiency of a single spherical particle $\mathrm{Q}_{\text{back}}(\lambda, m, a)$ can be calculated based on Mie theory and can be shown to depend on the wavelength λ, refractive index m, and size a (diameter) of the sphere, (Bohren and D.R. 1983). $N(a)$ is the particle size-distribution [(number)/m]. Similarly the volume extinction coefficient per unit length can be expressed as:

$$\kappa = \int_0^\infty \pi a^2\, \mathrm{Q}_{\text{ext}}(\lambda, m, a)\, \mathrm{N}(a)\, \mathrm{d}a \tag{A.34}$$

Here $\mathrm{Q}_{\text{ext}}(\lambda, m, a)$ is the extinction cross-section efficiency also to be evaluated from Mie theory.

Now given the following assumptions, a linear relation between the backscatter and extinction can be introduced (Evans 1988):

1. The quantities $\mathrm{Q}_{\text{back}}(\lambda, m, a)$ and $\mathrm{Q}_{\text{ext}}(\lambda, m, a)$ remain constant with time which means that the optical properties of the particle remain unchanged during a single measuring trial (1/2 - 1 hr.).

2. The shape of the particle size distribution does not change during an experiment. This means that the distribution $N_t(a)$ at time t can be expressed as $N_t(a) = f(t)N_0(a)$ where $f(t)$ contains the time variation in the number of particles, leaving the size distribution $N_0(a)$ unchanged.

By dividing the two equations (A.33) and (A.34) we get the relation:

$$\alpha = \frac{\beta}{\kappa} = \frac{\int_0^\infty \pi a^2 \, \mathrm{Q_{back}}(\lambda, m, a) \, \mathrm{N}_0(a) \, \mathrm{d}a}{\int_0^\infty \pi a^2 \, \mathrm{Q_{ext}}(\lambda, m, a) \, \mathrm{N}_0(a) \, \mathrm{d}a} \tag{A.35}$$

During quasi-stationary meteorological conditions with respect to background aerosol level and humidity, we assume that the shape of the particle size distribution is constant, and consequently a constant relation between backscatter and extinction is obtained.

Adjusting α

In the first two experiments only horizontal line scans were made in order to adjust the laser power, sensitivity range, other settings to provide data for estimating α values for the smoke, see (Jørgensen, Mikkelsen, Streicher, Herrmann, Werner and Lyck 1997), and for the ammonia seeded HF cloud. It should be noted that α is only relevant for optically thick clouds, i.e. clouds with low cross-plume transmission. In other words α is used to make corrections for the transmission loss through the plume. The transmission depends on factors such as windspeed and emission rate and varied somewhat for the experiments. Typically the transmission was 50 to almost 100% in which case the correction is relatively small and α need not be known very precisely. The uncertainty of α does not have much influence on calculated parameters such as plume widths and centroid position. In the first two trials the lidar was scanning a fixed beam direction along the ground. A hard target, consisting of wires, had been placed at the opposite side of the release sector. α was determined by comparing the reduction of the signal from the hard target due to the cloud. The value of α was found to be twice as high for the smoke compared to the HF cloud.

Noise removal

Due to the smallness of the detector current the signal exhibits shot noise. The main source of the noise is the wideband pre-amplifier. In the signal the shot noise is seen as small narrow spikes. For the present measurements the noise level was just a few percent of the typical HF signal. Noise should be removed from the concentration profiles because it sets a small level even far away from the actual cloud, which may influence calculated widths etc. Due to the finite width of the laser pulse the backscatter from an ideal point echoes a signal with finite width, and any spike in the signal which is narrower must be noise. The intensity of the laser pulse is known to vary almost like a Gaussian along the beam, and from this limits can be set on the point-to-point variations of the true signal. Based on this the signal was de-spiked by cutting away too fast variations. Subsequently any remaining noise was removed by applying a lower threshold (corresponding to less than 1% of the typical signal).

A.2 Smoke machine

Artificially generated smoke was used during all the experiments. An aerosol generator produced a continuous release of sub-micron aerosol particles consisting of a conglomerate of SiO_2 and NH_4Cl, which could be detected by the lidar system. Mixing the liquids $SiCl_4$ and a 25% water solution of NH_4OH in a neutralizing, stoichiometric ratio (1:3.2) in a jet, the reactions between the two liquids are as follows:

$$\begin{aligned} \mathrm{SiCl_4 + 2\,H_2O} &\rightarrow \mathrm{SiO_2 + 4\,HCl}, \\ \mathrm{NH_4OH + HCl} &\rightarrow \mathrm{NH_4Cl + H_2O}. \end{aligned}$$

The flow of chemicals was kept at a constant rate, and depending on the atmospheric stability and chemical flow rate, the plumes were visible several kilometers downwind. The flow speed from the air tube to the injecting tubes for the chemicals was approximately 30 m/s.

The size distributions of the artificially generated particles have been found to be remarkably consistent and reproducible in terms of size range and shape. Earlier experiments have shown the size distributions to be Log-normal $N(\mu_r, \sigma_r)$ with a geometric mean $\mu_r = \mathrm{Log}(\bar{r})$, corresponding to $\bar{r}$ of 0.232 μm. The standard deviation of the mean radius was 0.007 μm based on 14 different experiments. The corresponding standard deviation $\sigma = \mathrm{Exp}(\sigma_r)$ for the distribution was within the range 1.31 - 1.22 .

Is the smoke passive?

The smoke generation is basically a neutralization of acid so some heat is generated. In the following we estimate the temperature rise of the passive smoke due to this heat generation.

The enthalpy of the different compounds and the enthalpy budget of the mixing process are shown in table 9. Values are from Handbook of Chemistry and Physics 72^{nd} Edition.

Table 9. The enthalpy calculation where we have estimated the release of energy (Q) for one mol of $SiCl_4$.

Substance	Phase	molar weight g/mol	Density kg/l	enthalpy kcal/mol	No of mol	enthalpy kcal/mol
$SiCl_4$	liq.	169.9	1.483	-164.2	1	-164.2
NH_4OH	liq.	35		-87.505	4	-350.02
H_2O	liq.	18		-68.35	7.33	-501.23
H_2O	g	18		-57.79	-9.33	539.37
NH_4Cl	s	53.453		-75.15	-4	300.6
SiO_2	s	60.086		-215.94	-1	215.94
					Q=	40.6

The air flow of the smoke generator is 0.40 m^3/s. With a release of 8 l/h of $SiCl_4$, which corresponds to 3.28 kW, we obtain an initial temperature rise of 8 ^oC of the smoke. Model calculations show that the temperature 10 meter from the release will be less than 0.5 degree above the ambient temperature. Measurements of the temperature 10 meters from the release rig shows no significant temperature rise due to the smoke plume. We therefore conclude that smoke can be regarded as passive for all practical purposes.

A.3 Met mast data logger

The data from the met mast are sampled on a personal computer by software developed at Risø. The system consists of a PC with serial ports, ADC card, and a timer card. All analog signals are sampled through a multiplexer (16 channels) connected to the ADC card in the PC. The frequency signal (from the cup anemometers) are sampled through a cup counter interface (developed at Risø) connected to the timer card in the PC. The serial signal (from the sonic) is optically isolated from the PC and sampled by the standard serial cards in the PC.

The system samples the data as analog, frequency, or serial signals. Recording of the signals are performed continuously with a base frequency of 20 Hz without any timegaps in the data. The system ran continuously during the whole experiment. On-line calculation of basic statistics such as variances, means, and min and max values are performed on the basis of 5 min and half-hour periods. The time series

of all the data are stored each half-hour and zipped into one file containing both the calculated statistics and the raw data.

In addition to the basic statistics, covariances from the four sonic signals are calculated to obtain basic micro-meteorological parameters.

A.4 Kipp & Zonen CM11 pyranometer

This instrument measures the incoming short wave irradiation on a plane surface, and it follows the requirements of the WMO secondary standard. The sensor is a plate constructed of 100 thin layers of thermocouples, also called a thermopile. When the solar radiation heats the upper surface, a temperature gradient develops in the thermopile yielding a thermoelectric force. In order to minimize the influence of convective heat loss, the thermopile is covered by a double glass dome. It is important to keep the outer domes tidy and the interior of the sensor dry. The technical data are listed in table A.4.

Table 10. Specification of Kipp & Zonen CM11 and CM14.

Spectral range	305–2800 nm (50% points)
Sensitivity	4-6μV/Wm^{-2}
Impedance	700–1500 Ω
Response time	1/e 4 s, 99% 26 s
Nonlinearity	$\pm$ 0.6% ($<$ 1000 W/m^2)
Tilt error	none
Operating temperature	-40 to 90°C
Temperature dependence of sensitivity	$\pm$1% (-10 to 40°C)
Maximum irradiance	4000 W/m^2
Directional error	$<\pm$10 W/m^2 at 1000 W/m^2
Weight	0.85 kg
Cable length	10 m

A.5 Frankenberger psycrometer

The instrument measures the dry the wet-bulp temperatures. Knowing the barometric pressure and the saturated vapour pressure curve of water the air humidity can be calculated. The thermometers are two Pt100 sensors placed in individual radiation shields ventilated by an air pump. The Pt100 sensors are powered and monitored by a temperature difference transmitter. Only the temperature difference is transmitted. The relative humidity depends foremost on this difference and is nearly insensitive to the absolute temperature, which may therefore be estimated or measured with a nearby sensor. The nearest thermocouple sensor was used.

A.6 Vaisala HMP45A/D

The Instrument measures the relative humidity of the air. The basic principle of humidity measurement the HUMICAP sensor is that a thin polymer film either absorbs or exudes water vapour as the relative humidity of the ambient air rises or drops. The dielectric properties of the polymer film depend on the amount of water contained in it: as the relative humidity changes, the dielectric properties of the film change and so the capacitance of the sensor changes. The electronics

of the instrument measure the capacitance of the sensor and convert it into a humidity reading, see also www.vaisala.com.

Table 11. Specification of Vaisala HMP45A/D

Measurement range	0.8 ..100 %RH
Output scale	0-100 % RH equals 0-1 VDC
Accuracy at +20 (lab.) ^oC	±1% RH
Accuracy field mes. (0..90%	±2% RH
Accuracy field mes. (90..100%)	±3% RH
Response time (90%RH)	15 s
humidity sensor	HUMICAP

A.7 Barometer

The barometer uses a calibrated pressure transducer supplied by Vaisala. The transducer was built into a suitable box and calibrated against a precision mercury barometer. The tolerance (including repeatability) is about 2hPa.

A.8 Pt100 absolute thermometers

The temperature is measured by means of a standard 100 Ohm Platinum resistor. Pure Platinum is used to define the practical temperature scale because the temperature-resistivity curve of pure Pt is highly reproducible. The resistance is measured by the four point method (separate leads for current and voltage drop detection). The method is the most accurate one for practical use.

The Pt100 sits in a standard white radiation shield. Like other thermometers the Pt100 yields its own temperature, which need not be equal to the temperature of the surrounding air. The most severe source of error is heating by sunlight, hence the shield. The response of the sensor is slow, of the order of minutes.

The Pt100 was calibrated against a precision Platinum reference probe (P1182 probe constructed by Risø). The reference probe was in turn calibrated at Risø's thermometry lab.

The Pt100 sensor is very reliable, but experience shows that the calibration may suffer if it is exposed to shocks caused by e.g. dropping it. This may have happened during the set-up of the met mast, because the Pt100 readings disagreed with the other temperature sensors on the mast by 1-2K. The sensor was recalibrated after the campaign, and it was verified that the calibration had indeed changed. Application of the new calibration resulted in a far better agreement.

A.9 Solent sonic anemometers

The principle of the Solent ultrasonic anemometer is to measure the time-of-flight of a ultrasonic sound signal in two directions between a pair of sound transducers. From these measurements the wind velocity component along the measurement path is calculated with analog computing. This is done for three pairs of sound transducers arranged according to the vertical direction and two horizontal directions with an angle of 120°. The instrument coordinate system of the Solent anemometer is left-handed. The technical data are listed in table 12.

From one of the measuring paths (the vertical) the average speed of the pulses is also evaluated. This speed of sound is converted into a 'sound virtual' sonic

temperature equal to the true temperature in pure air at 1 atm with no humidity.

Table 12. Specification of the research version of a Solent ultrasonic anemometer.

Sample rate	168/s
Data output rate	21/s 10 Hz or 56/s 28 Hz
Wind speed range	0–60 m/s
Power supply	9–30 VDC, 150 mA
Wind speed accuracy (10 s average)	± 1% below 30 m/s;± 2% above 30 m/s
Instantaneous accuracy	± 3% below 30 m/s
Wind speed offset	± 0.02 m/s
Direction accuracy (10 s average)	± 1° below 30 m/s;± 2° above 30 m/s
Speed of sound accuracy	± 0.5%
Cal/maintenance requirement	None
Analogue output (4)	2.5V ±2.5V 11 bit total
Analogue output date	U, V, W, Speed of sound or 2.5 V ref.
Analogue output range	± 30 m/s or ± 60 m/s
Analogue inputs	Five channels, 0–5 V, 11 bit
Serial output	RS485/422, 4800–19200 baud
Serial data	U, V, W, Speed of sound, diagnostics
Logged data	Up to 2 min internal data buffer
Internal memory	32 kB, Lithium backup
Temperature (storage)	-40 to 75°
Temperature (operation)	-20 to 50°
Icing	Operational up to 2–3 mm ice cover
Precipitation	Operational up to 300 mm/Hr
Altitude	0–3000 m
Weight	1 kg

A.10 Risø cup anemometer

The Risø cup anemometer has three cups on a rotor with a diameter of 19 cm mounted on a 25 cm vertical axis. The response function is very close to being linear, with an O(0.3) m/s offset velocity below which the drag of the wind is too weak to overcome the friction in the ball bearings. The output of the instrument is two pulses per rotation, but in order to compensate for possible mechanical asymmetries, the wind speed is always calculated from a full rotation. The response time is proportional to the rotation rate and found to be l/U, where l is a length constant O(1.5) m and U is the wind speed. Thus, for a typical meanwind speed of 2 m/s the response time is 0.6 s. In order to minimize flow distortion of the mast, the anemometer is placed on a O(1.5) m long boom. Furthermore, the anemometer is placed on a O(0.5) m vertical rod to avoid the effect of the boom.

Table 13. Specification of the Risø cup anemometer.

range	up to 0-70 m/s
distance constant	1.5 m
temperature range	-25°C to +50°C
protection	short circuit and overvoltage protected
dimensions	
height	250 mm
diameter of housing	50 mm
rotor diameter	190 mm

Calibration

The cup anemometers are calibrated in a wind tunnel at regular intervals. The following pages show individual calibration sheets for the cup anemometers used.

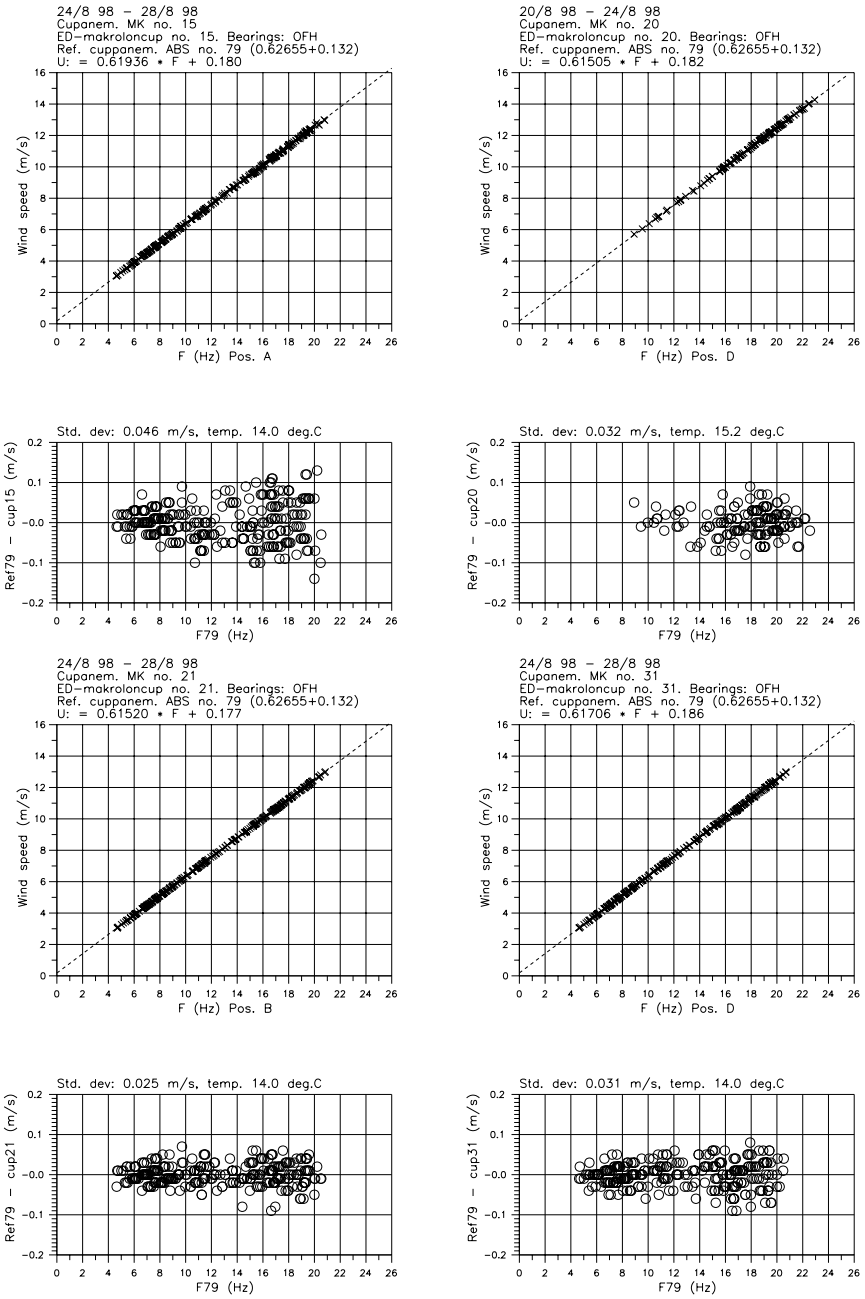

Figure 13. Calibration sheets for the Risø cupanemometers.

A.11 Risø wind vane

The dimensions of the wind vane are similar to those of the cup anemometer, and the response time about twice as fast. The transducer is a resolver mounted on the vane shaft inside the windvane housing. A resolver is essentially a 2-phase transformer with stator windings and 2 rotor windings wound 90° out of phase. When a stator winding is excited with a sinusoidal carrier the two output amplitudes of the rotor voltages will be proportional to the sine and cosine, respectively, of the rotor shaft angle.

The resolver eliminates the noise and lifetime problems usually encountered in potentiometer-based wind vanes. Furthermore, this type of transducer permits a variance calculation based only on the meanvalue measurements.

The function of the transmitter is to generate the carrier for the resolver and synchronously demodulate the rotor voltages by means of phase-sensitive detectors.

Table 14. Specification of the Risø P2021 wind vane with a P2058 wind direction transmitter.

range	0-360°
resolution	infinite
inaccuracy	0.5° typical
outputs	$V_{cos} = 4.5 \cdot \cos\phi$
	$V_{sin} = 4.5 \cdot \sin\phi$
vane material	polystyrene/epoxy
distance constant	0.7 m
damping factor	0.5
maximum wind speed	40 m/s
temperature range	-25°C to +50°C
power supply	+ 15 V, + 20 mA
protection	short circuit and overvoltage protected
dimensions	
height	300 mm
diameter	60 mm
vane	100·200 mm
transmitter box	175·80·60 mm

A.12 Fast temperature sensors

The Risø temperature sensor is a fast, reliable and inexpensive instrument ideally suited for measurements of temperature fluctuations in the atmospheric boundary layer. Using an array of sensors a detailed spatial and temporal resolution of the temperature profile can be obtained. The sensor consists of a thermocouple probe and a water tight metal box containing electronic icepoint compensation and preamplifier. The 100mm long thermocouple probe is connected directly to the box in order to effectively eliminate noise, which can be a problem for long thermocouple wires. The electronics is mounted on a PCB placed in a thick Al block serving as thermal anchor. The thermal anchor has direct thermal contact with the metal housing, ensuring a rapid warming/cooling of the electronics so that temperature difference between the hot and the cold junction is minimized (this reduces errors due to thermopower nonlinearity). The central IC is located in a symmetric geometry and the cold junctions and surface mounted miniature components are placed directly under the IC between the pins in heat conducting cement. Larger components (electrolytes) are thermally separated from the IC. This design minimizes icepoint compensation errors since the cold junctions are positioned close to the IC chip at a point with zero thermal gradient.

The sensor output depends on

1. the temperature of the chip
2. the thermoelectric voltage set up by the temperature difference between the 'hot' junction (the tip of the probe) and the 'cold' junctions (icepoint compensation)

The chip amplifies the thermoelectric voltage to a nominal value of 10mV/K and adds a voltage proportional to the chip temperature in Centigrades (also nominally 10mV/K). The first signal is proportional to the thermopower generated by the temperature difference between the cold and the hot junction. This represents the fluctuating part of the signal. The amplification is laser trimmed to correspond to 10mV/K for type K thermocouple material. In normal circumstances the metal house, including the chip, will follow the ambient temperature to within a few degrees, hence the main part of the output signal stems from the cold junction compensation.

Specifications

- Positive power supply voltage : 5-15V
- Negative power supply[3] : optional
- Power consumption : 800μW
- Output [4]: V_{out}=10$mV/^0$C
- Temperature rangee[3] : 0-50 ^{0}C
- Absolute accuracy (calibrated)[5]: $\pm 0.1\,^0C$
- Tracking[6]: 0.014K rms.
- Thermocouple wire material: $\emptyset$ 100μm NiCr-NiAl (type K)

[3]Negative temperatures can be measured if a negative voltage is supplied.
[4]t in ^{0}C
[5]Assuming that the chip temperature is within a few degrees of the measured temperature.
[6]The number indicates the standard deviation of readings from ten devices cooled to 13 ^{0}C. Calibration constants had previously been determined from readings at 3^{0}C and at 20^{0}C. During the calibration sensors were replaced by Copper clamps. The tracking therefore only relates to the on-chip cold junction compensation.

- Thermocouple response time[7] : 80 ms
- Sensor 3dB cutoff[8] : ∼1Hz
- Curcuitry built around AD595CQ
- Electronic filtre (AD595)[9]: 15kHz
- Rms noise level[10]: $< 100\mu$V ($\sim$ 0.01 K)
- Size of box: $25 \times 35 \times 100$mm
- Probe length: 100mm
- Component cost[11]: 500 DEK

Calibration procedures

The sensors were calibrated in a thermal bath against a precision Platinum reference probe (P1182 probe constructed by Risø). The reference probe was calibrated at Risø's thermometry lab. The probes were removed and replaced by Cu clamps. This determines gain and offset of the cold junction compensation. The thermoelectric characteristics of the probe are certified. The probes have not been calibrated, since they produce only a small part of the signal and the Ni alloys are certified. The wires which are used have been tested by the thermometry lab in other connections and they were found to follow the standard type K thermopower curve very precisely. The part of the signal generated by the probe should be accurate to within 0.05 K.

Typically the gain was found to be within 1% of the ideal 10mV/K, while offsets as large as 2K were observed. By comparison with earlier calibrations it was found that the gain is very stable over long periods while the offset may change somewhat (∼1 K per year). The linearity is excellent: less than 0.01 K rms error (after calibration) over a 20 K interval (15°C to 35°C).

Carefully calibrated the absolute accuracy of the sensor is 0.1K under laboratory conditions. In the harsh conditions in the field the accuracy is probably somewhat less.

Figure A.12 shows a spectrum made by means of a hot air blower (hair dryer). The broken line is a model spectrum

$$S_{\mathrm{model}}(n) = \frac{C\frac{n^{-5/3}}{1+(n/n_s)^2} + L_s}{1 + (n/n_{lp})^2} \tag{A.36}$$

Response characteristics

where n is the frequency, L_s is the noise level of the sensor electronics, n_s is the 3dB frequency of the sensor, and n_{lp}=7Hz is the 3dB frequency of the low pass filter of the mux card. The plot actually shows $n(S_{\mathrm{model}}(n) + S_{\mathrm{model}}(n_N - n))$, where n_N is the Nyquist frequency (250Hz). Choosing $L_s = 6 \cdot 10^{-5}\mathrm{K}^2/\mathrm{Hz}$ and n_s =2Hz gives a good fit to the data in the high frequency end of the spectrum. The corresponding noise level is

$$\sigma_T = \sqrt{L_s n_{lp}\pi/2} \sim 25\mathrm{mK} \tag{A.37}$$

and the response time is

$$\tau = \frac{1}{2\pi n_s} \sim 0.08\mathrm{s} \tag{A.38}$$

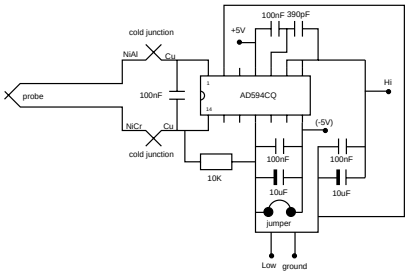

Figure 14. Diagram of the preamp and icepoint compensation electronics.

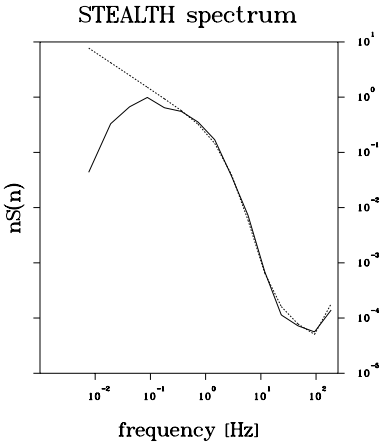

Figure 15. Solid line: experimental spectrum. Dotted line: model spectrum (see text).

Systematic errors

The hot junction is not shielded from sunlight. This introduces a systematic error due to radiative heating. Using a correlation for the heat transfer the following

[7]The response time is defined as the time to reach 1/e of a step impulse
[8]Then sensor response time depends on the ambient wind speed.
[9]An additional ∼10Hz lowpass filter in the preamp is recommended
[10]Measured through a 7Hz 1st order low pass filter using a 10× pre-amplifier and a 12 bit adc set to range 0-5V. The noise was less than one bit
[11]Including all parts except the cable.

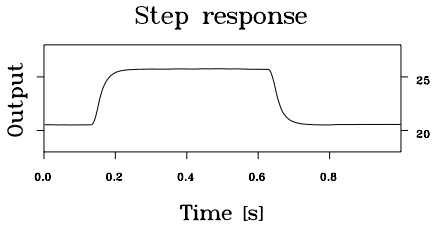

Figure 16. The response to a square voltage signal applied to the probe input. The output was sampled using the datalogger system described in the text including a 7Hz low pass filter.

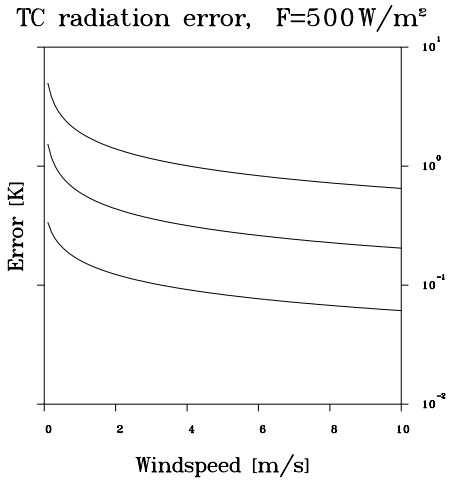

Figure 17. Radiation error of NiCr-NiAl (type K) thermocouple for D = 10mm 1mm and 0.1mm. $F = 500W/m^2$ is assumed.

heat ballance can be set up:

$$0 = D\pi h(T_a - T) - D\pi\epsilon\sigma T^4 + D\pi\epsilon\sigma {T_a}^4 + D\epsilon$$

$$h = \frac{\lambda}{D}\left(0.42Pr^{0.2} + 0.57Pr^{0.33}Re^{0.5}\right) \tag{A.39}$$

where the constants are: ϵ=0.45, λ=2.62·10^{-2}W/mK, Pr=0.708, ν=1.57·10^{-5}, $\sigma = 5.67 \cdot 10^{-8}\mathrm{W/m^2K^4}$.

Figure A.12 shows calculated corrections for three diameters. The correction is too small to matter.

Dew (or rain) is more serious. When the probe gets wet it follows a wet bulb temperature rather than the ambient air temperature.

Spiders is another problem. The probe catch the webs of flying spiders and therefore the probes have to be cleaned every now and then.

The sensor picks up strong radio signals. Radio transmitters should not be placed near the sensor (e.g. on the same mast).

A.13 Radiation temperature sensor

Principle of operation

The sensor measures the radiation temperature of the ground. It provides two signals: the sensor temperature and a radiation signal provided by an infrared detector. The housing is made from an Al pipe (5mm wall thickness) with 20mm Al plugs at the ends. The detector is located at the end in a hole with a 45° conical opening in good thermal contact with the Al plug and the temperature sensor located next to it. The radiation detector consists of a miniature thermopile located inside a hermetically sealed can with a Germanium window. Over an appreciable range the detector signal is proportional to the difference between the effective black body radiation temperature of the incoming radiation and the sensor temperature. It is not actually a thermometer, it is a radiometer, because it responds to the radiation emitted from the ground. The instrument was built by Risø.

- Germanium window transmitting in tha 8-14μm range

- Ultra fast detector response (< 100ms)
- Wide view angle *Specifications*
- 10mV/K standard output
- Low noise
- Chopper stabilized amplifiers
- Low power consumption (∼ 100mW)
- Rugged water tight design
- Standard Burndy connector
- Standard ±15V power

The temperature sensor was calibrated in the same way as the fast thermometers to an accuracy of about 0.1K. The radiation detector was calibrated by pointing it into a long Copper tube which had been painted black inside and put into a dewar filled with water at various temperatures. *Calibration*

The radiation temperature of the ground need not be the same as the true temperature, since this also depends on the emissivity of the ground. In this case the ground was covered by about 50cm high grass which is known to have an emissivity close to 1. Sunlight reflections may also be a problem although the Ge window is an effective daylight filter. The instrument was place at a height of 2m looking down and tilted towards the North. The use of chopper stabilized amplifiers limits offset errors to less than 0.02K. The accuracy is believed to be about $< \pm 1 <$ K. *Systematic errors*

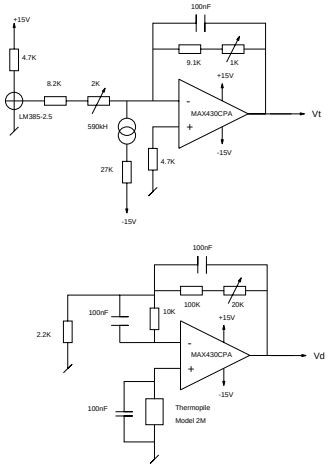

B Experimental data

B.1 Presentation of the individual trials

Below meteorological data sheets and Lidar data for each of the 12 trials are presented. The comments are based on noted taken during the experiments.

HF001

Comments: The first release, which was meant to be a rehearsal. Neutral stability and 7/8 cloud cover. There did not appear to be much difference between HF and smoke except for the first $\sim 20m$, where the HF plume seemed to be slightly higher than the smoke. The plumes had ground contact. Unlike in the remaining experiments the HF plume was *not* seeded with NH_3. The HF plume was invisible beyond 30-40m, and hence no lidar measurements were made. The smoke plume was scanned along a fixed horizontal line, and the lidar data is for calibration only.

HF002

Comments: About 6/8 cloud cover and neutral stability. No lift-off. The HF release was seeded both during the main liquid release and the during the subsequent gaseous release. The seeding was stopped after about 8 minutes and the gaseous release instantly became invisible. The lidar was scanned along a fixed horizontal line and the data is for calibration only.

HF003

Comments: Overcast and stable. The HF cloud seemed heavy on the first 5 meter, and after that passive behaviour, with no observed difference between smoke and HF. Both plumes were on the ground at all times. HF deposit on the ground near the first thermocouple array. NH_3 seeding stopped after 5 minutes, but the ground continued smoking. Problems with the rig datalogger, rig data lost.

Table 15. Timing

Release	Start	Stop	2D scans
HF003	09:30:00.56	09:33:11.65	91
HF003S1	09:40:10.40	09:57:32.67	492

Table 16. Plume parameters 100m downwind derived from lidar measurements

Parameter	Unit	HF003	HF003S1
$\overline{H}$	[m]	6.50	4.69
σ_z	[m]	3.71	3.06
σ_y	[m]	12.03	14.48
σ_{ym}	[m]	6.82	7.91

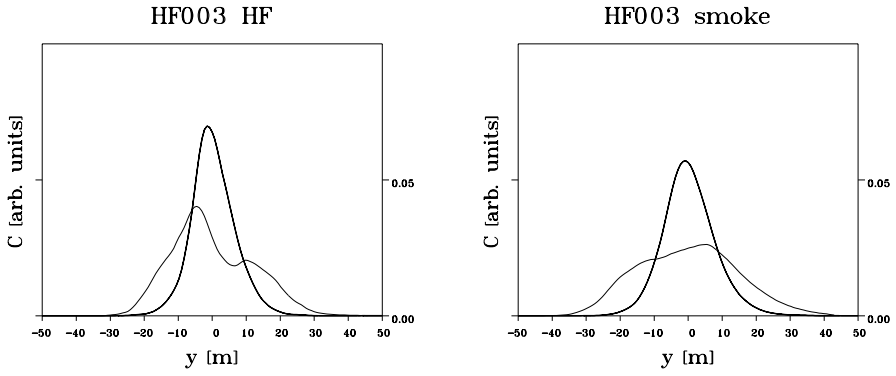

Figure 18. Depth integrated horizontal profiles from fixed frame analysis (thin line) and moving frame analysis (thick line).

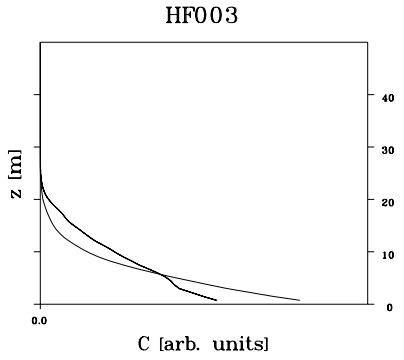

Figure 19. Cross-plume integrated vertical concentration profiles. Thin line: smoke, thick line: HF.

Parameter	Unit	HF003	HF003S1
Cup 10m	[m/s]	5.206	5.355
Cup 5m	[m/s]	4.583	4.799
Cup 2m	[m/s]	3.777	3.874
Cup 1m	[m/s]	3.168	3.195
Dir. 10m	deg.	256.487	261.523
Dir. 2m	deg.	254.684	259.505
Temp 10m	[^{o}C]	18.003	18.126
Temp 2m	[^{o}C]	18.338	18.458
RH 10m	[%]	80.674	78.527
RH 6m	[%]	81.568	79.698
RH 2m	[%]	80.172	78.204
Abs Hum 10m	[g H_2O/m^3]	12.389	12.148
Abs Hum 2m	[g H_2O/m^3]	12.560	12.339
TC 9m	[^{o}C]	18.017	18.144
TC 7m	[^{o}C]	18.080	18.206
TC 5m	[^{o}C]	18.198	18.317
TC 320cm	[^{o}C]	18.232	18.363
TC 160cm	[^{o}C]	18.374	18.517
TC 80cm	[^{o}C]	18.637	18.805
TC 40cm	[^{o}C]	18.737	18.905
TC 20cm	[^{o}C]	18.855	19.016
TC 10cm	[^{o}C]	19.031	19.204
TC 5cm	[^{o}C]	19.379	19.581
T surface	[^{o}C]	19.239	19.487
U	[m/s]	5.262	5.456
σ_u^2	[m^2/s^2]	0.960	0.611
σ_v^2	[m^2/s^2]	0.608	0.581
σ_w^2	[m^2/s^2]	0.175	0.157
σ_T^2	[K^2]	0.032	0.021
u_*	[m/s]	0.381	0.330
$\overline{w't'}$	[m/s K]	0.029	0.022
L	[m]	-141.505	-124.347

Table 17. Key meteorological parameters measured during the experiments. The upper part represents the profile measurements and the lower part represents micrometeorological paramters measured by the sonic

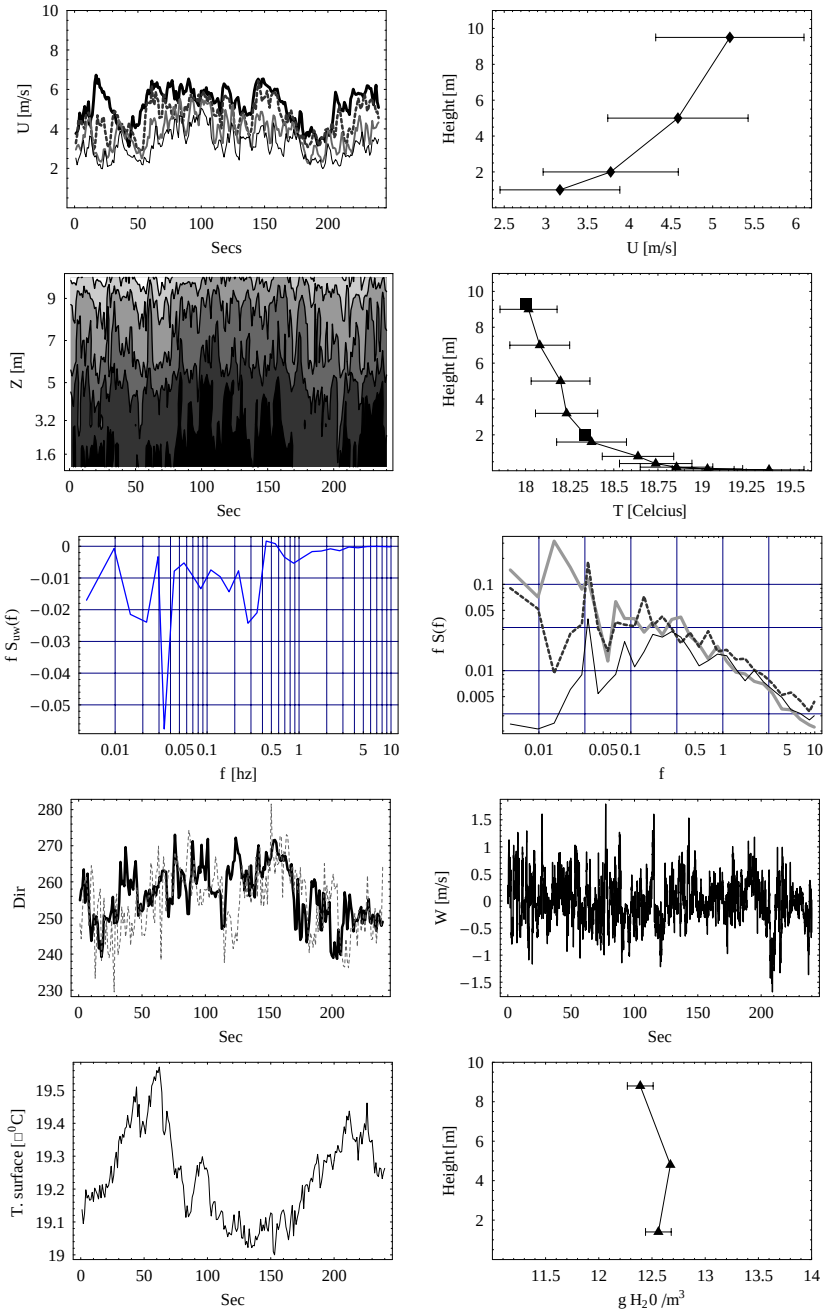

Figure 20. Overview of the meteorology during the release. In the first row is shown the wind-speed time series and the corresponding averaged wind profile. Second row shows time series of the temperature contours measured by the thermocouples and the corresponding temperature profile, the boxes shows the pt100 temperature. Third row shows the co-spectrum of $u'w'$ and the power spectra of u, v, w. The fourth row shows time series of the wind directions measured at 10 and 2m and the second figure shows a time series of the vertical fluctuations w'. The fifth row shows a time series of the surface temperature and the profile of absolute humidity.

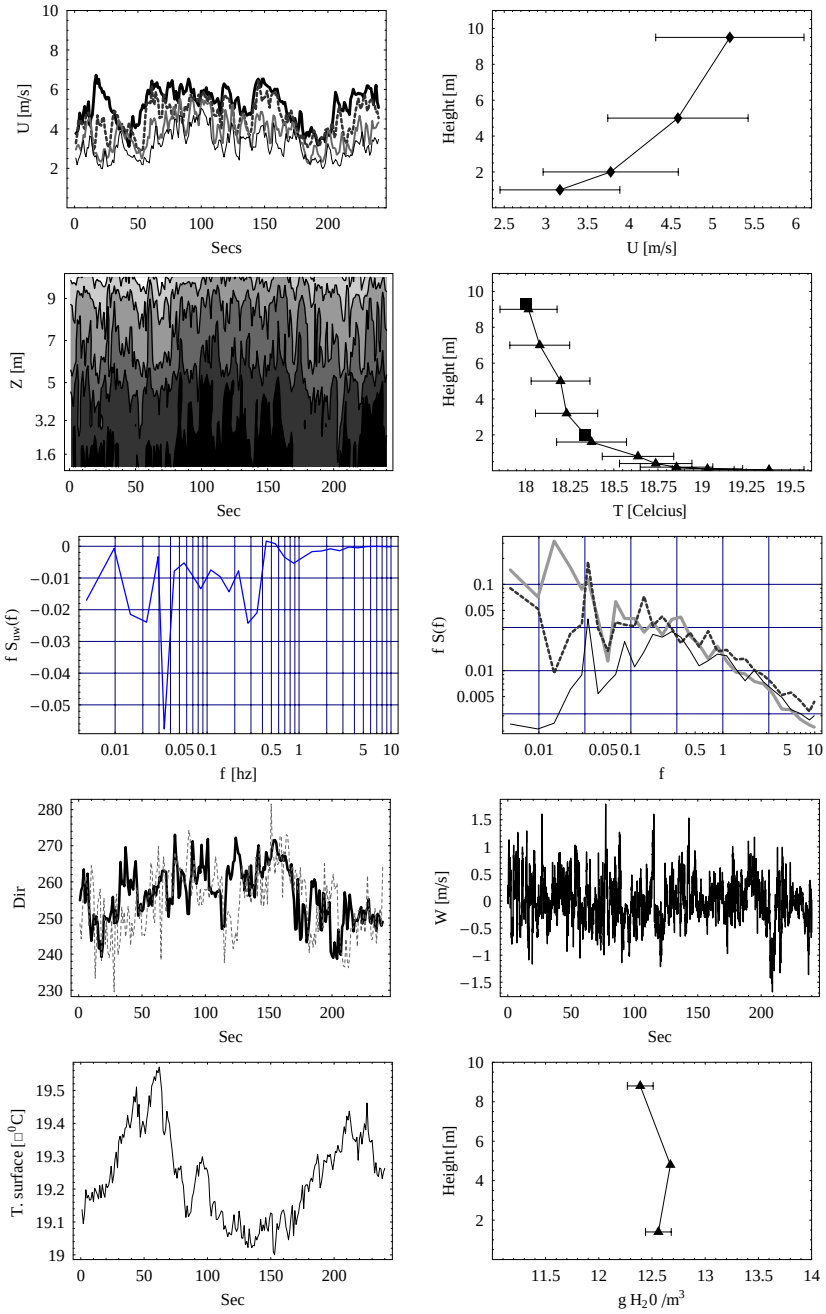

Figure 21. Overview of the meteorology during the release. In the first row is shown the wind-speed time series and the corresponding averaged wind profile. Second row shows time series of the temperature contours measured by the thermocouples and the corresponding temperature profile, the boxes shows the pt100 temperature. Third row shows the co-spectrum of $u'w'$ and the power spectra of u, v, w. The fourth row shows time series of the wind directions measured at 10 and 2m and the second figure shows a time series of the vertical fluctuations w'. The fifth row shows a time series of the surface temperature and the profile of absolute humidity.

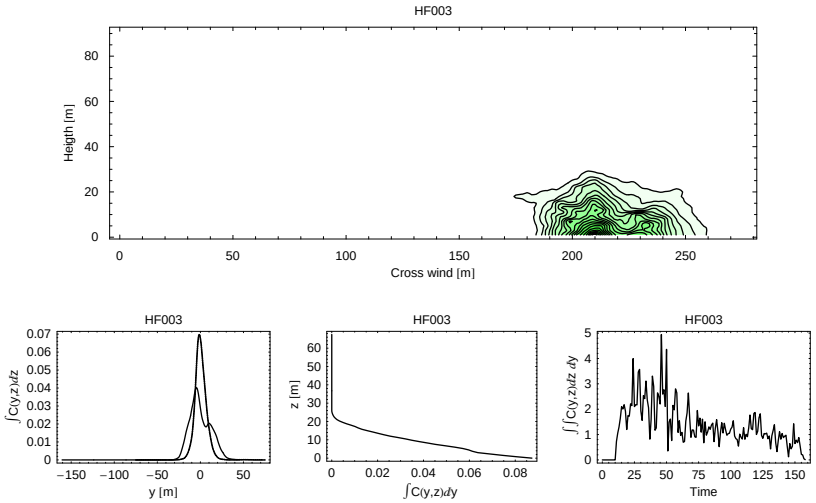

Figure 22. Overview of the measured HF plume profiles by the LIDAR. The top figure shows the contour lines of the mean profile. The bottom figures show : 1) The cross wind integrated profile in the vertical direction (thin line : fixed frame; thick line: moving frame). 2) The cross wind integrated profile in the horizontal direction.3) A timeserie of the cross wind integrated area of each LIDAR scan

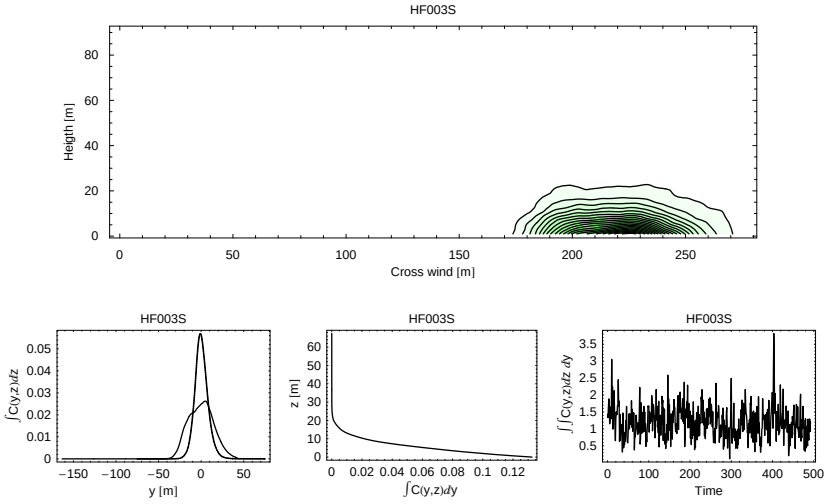

Figure 23. Overview of the measured smoke plume profiles by the LIDAR. The top figure shows the contour lines of the mean profile. The bottom figures show : 1) The cross wind integrated profile in the vertical direction (thin line : fixed frame; thick line: moving frame). 2) The cross wind integrated profile in the horizontal direction.3) A timeserie of the cross wind integrated area of each LIDAR scan

HF004

Comments: It rained about half an hour before the release. Overcast during the HF release, but sunshine with 6/8 cloud cover during the smoke release. The HF plume looked neutral.

Table 18. Timing

Release	Start	Stop	2D scans
HF004	10:43:16.91	10:47:35.55	191
HF004S1	10:53:03.40	10:57:35.06	200
HF004S2	11:00:20.39	11:04:52.60	201

Table 19. Plume parameters 100m downwind derived from lidar measurements

Parameter	Unit	HF004	HF004S1	HF004S2
$\overline{H}$	[m]	4.87	5.04	4.31
σ_z	[m]	2.68	2.97	2.83
σ_y	[m]	15.08	13.65	21.70
σ_{ym}	[m]	8.83	8.19	9.91

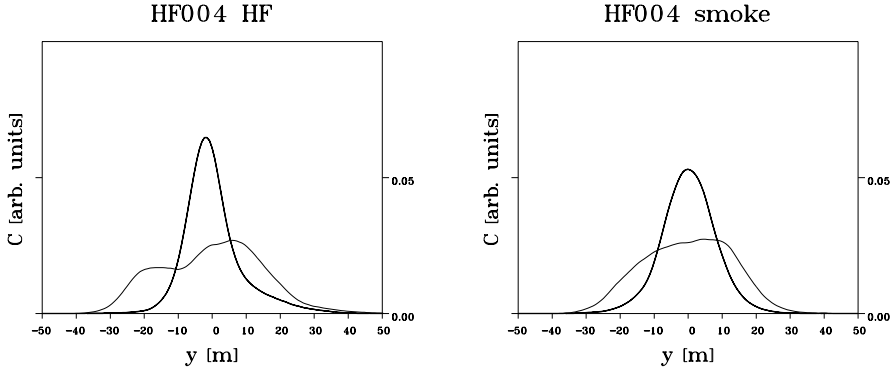

Figure 24. Depth integrated horizontal profiles from fixed frame analysis (thin line) and moving frame analysis (thick line).

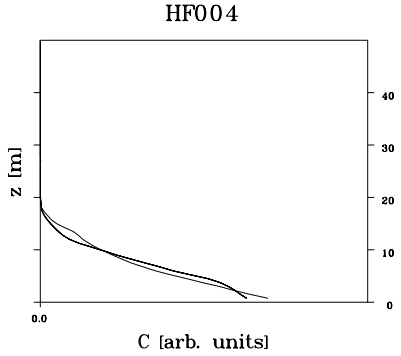

Figure 25. Cross-plume integrated vertical concentration profiles. Thin line: smoke, thick line: HF.

Parameter	Unit	HF004	HF004S1	HF004S2
Cup 10m	[m/s]	7.040	8.781	9.645
Cup 5m	[m/s]	6.335	7.921	8.664
Cup 2m	[m/s]	5.162	6.358	7.039
Cup 1m	[m/s]	4.289	5.341	5.819
Dir. 10m	deg.	222.356	215.701	218.111
Dir. 2m	deg.	218.711	212.712	214.830
Temp 10m	[^{o}C]	19.502	20.087	20.268
Temp 2m	[^{o}C]	20.000	20.721	21.093
RH 10m	[%]	89.825	85.485	83.150
RH 6m	[%]	88.971	85.424	82.582
RH 2m	[%]	89.180	84.357	81.362
Abs Hum 10m	[g H_2O/m^3]	15.072	14.844	14.593
Abs Hum 2m	[g H_2O/m^3]	15.407	15.199	14.981
TC 9m	[^{o}C]	19.744	20.347	20.486
TC 7m	[^{o}C]	19.775	20.374	20.508
TC 5m	[^{o}C]	19.963	20.615	20.771
TC 320cm	[^{o}C]	20.052	20.759	20.991
TC 160cm	[^{o}C]	20.330	21.030	21.329
TC 80cm	[^{o}C]	20.748	21.520	21.933
TC 40cm	[^{o}C]	21.026	21.852	22.340
TC 20cm	[^{o}C]	21.193	22.046	22.596
TC 10cm	[^{o}C]	21.564	22.529	23.200
TC 5cm	[^{o}C]	20.569	21.047	21.453
T surface	[^{o}C]	21.471	22.362	23.031
U	[m/s]	7.084	8.788	9.680
σ_u^2	[m^2/s^2]	0.713	1.352	1.569
σ_v^2	[m^2/s^2]	0.814	1.141	1.922
σ_w^2	[m^2/s^2]	0.219	0.470	0.411
σ_T^2	[K^2]	0.050	0.084	0.135
u_*	[m/s]	0.238	0.533	0.489
$\overline{w't'}$	[m/s K]	0.038	0.071	0.102
L	[m]	-26.550	-161.349	-86.162

Table 20. Key meteorological parameters measured during the experiments. The upper part represents the profile measurements and the lower part represents micrometeorological paramters measured by the sonic

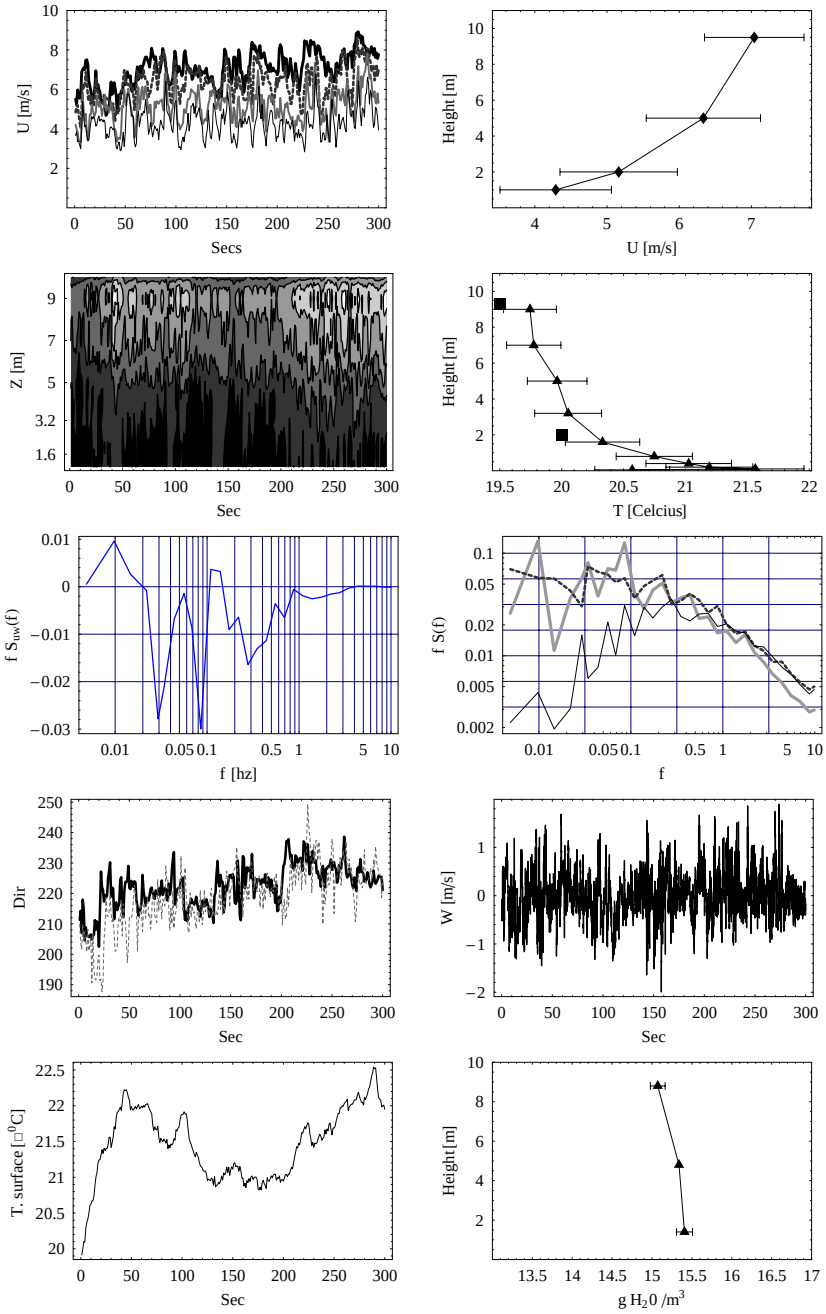

Figure 26. Overview of the meteorology during the release. In the first row is shown the wind-speed time series and the corresponding averaged wind profile. Second row shows time series of the temperature contours measured by the thermocouples and the corresponding temperature profile, the boxes shows the pt100 temperature. Third row shows the co-spectrum of $u'w'$ and the power spectra of u, v, w. The fourth row shows time series of the wind directions measured at 10 and 2m and the second figure shows a time series of the vertical fluctuations w'. The fifth row shows a time series of the surface temperature and the profile of absolute humidity.

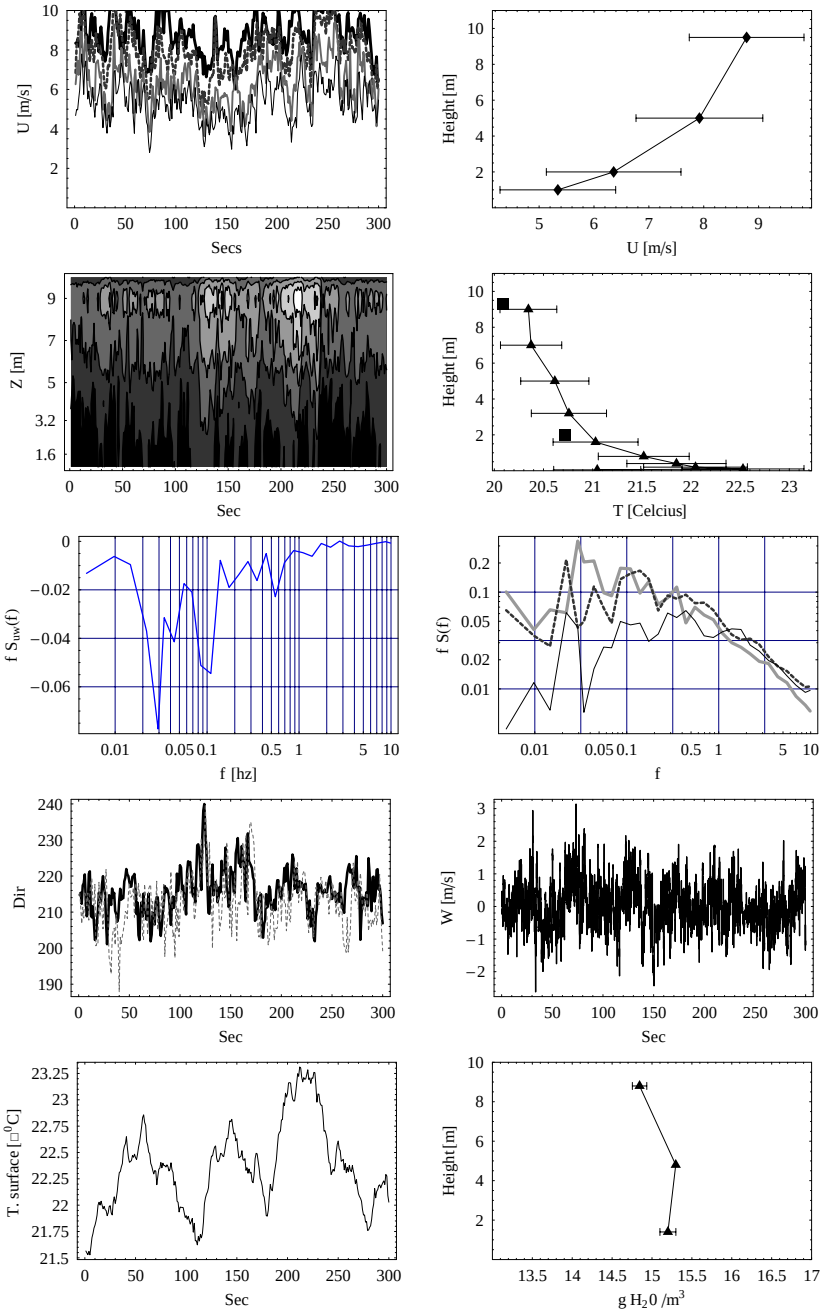

Figure 27. Overview of the meteorology during the release. In the first row is shown the wind-speed time series and the corresponding averaged wind profile. Second row shows time series of the temperature contours measured by the thermocouples and the corresponding temperature profile, the boxes shows the pt100 temperature. Third row shows the co-spectrum of $u'w'$ and the power spectra of u, v, w. The fourth row shows time series of the wind directions measured at 10 and 2m and the second figure shows a time series of the vertical fluctuations w'. The fifth row shows a time series of the surface temperature and the profile of absolute humidity.

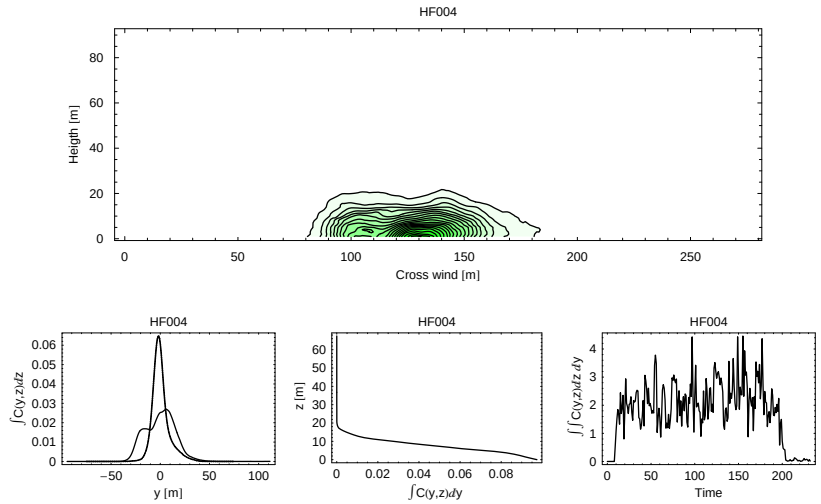

Figure 28. Overview of the measured HF plume profiles by the LIDAR. The top figure shows the contour lines of the mean profile. The bottom figures show : 1) The cross wind integrated profile in the vertical direction (thin line : fixed frame; thick line: moving frame). 2) The cross wind integrated profile in the horizontal direction.3) A timeserie of the cross wind integrated area of each LIDAR scan

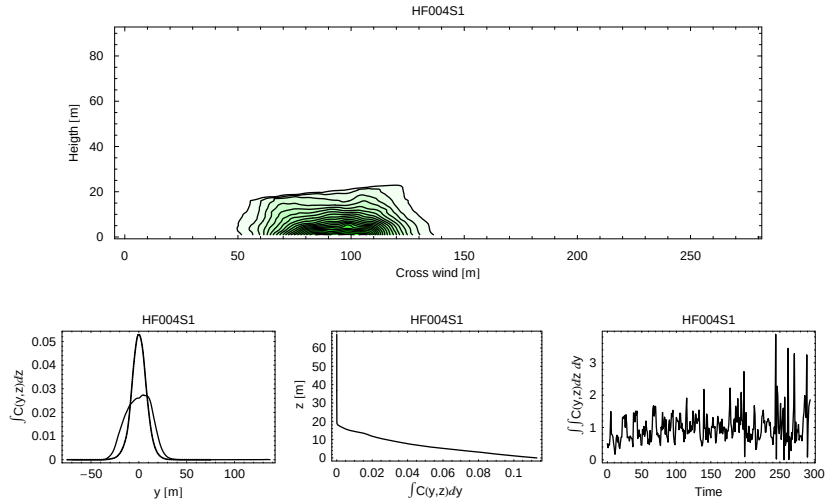

Figure 29. Overview of the measured smoke plume profiles by the LIDAR. The top figure shows the contour lines of the mean profile. The bottom figures show : 1) The cross wind integrated profile in the vertical direction (thin line : fixed frame; thick line: moving frame). 2) The cross wind integrated profile in the horizontal direction.3) A timeserie of the cross wind integrated area of each LIDAR scan

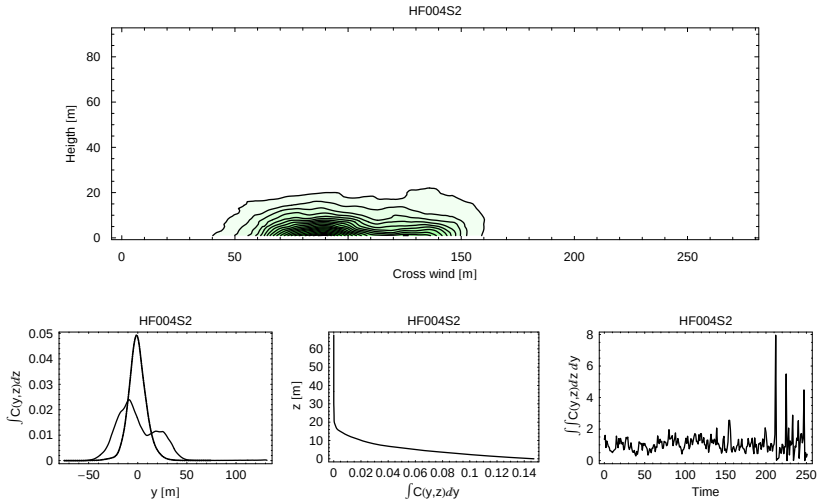

Figure 30. Overview of the measured smoke plume profiles by the LIDAR. The top figure shows the contour lines of the mean profile. The bottom figures show : 1) The cross wind integrated profile in the vertical direction (thin line : fixed frame; thick line: moving frame). 2) The cross wind integrated profile in the horizontal direction.3) A timeserie of the cross wind integrated area of each LIDAR scan

HF005

Comments: Overcast.

Table 21. Timing

Release	Start	Stop	2D scans
HF005	13:35:21.14	13:39:09.19	116
HF005S1	13:23:29.86	13:25:44.81	69
HF005S2	13:45:20.38	14:04:11.85	571

Table 22. Plume parameters 100m downwind derived from lidar measurements

Parameter	Unit	HF005	HF005S1	HF005S2
$\overline{H}$	[m]	5.32	4.92	4.85
σ_z	[m]	3.32	3.01	3.15
σ_y	[m]	14.08	12.58	16.73
σ_{ym}	[m]	7.48	8.81	8.20

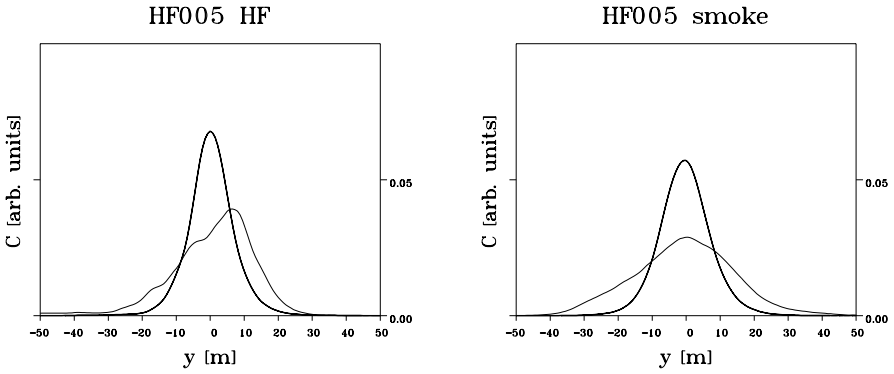

Figure 31. Depth integrated horizontal profiles from fixed frame analysis (thin line) and moving frame analysis (thick line).

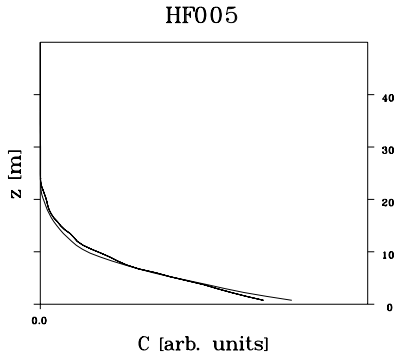

Figure 32. Cross-plume integrated vertical concentration profiles. Thin line: smoke, thick line: HF.

Parameter	Unit	HF005	HF005S1	HF005S2
Cup 10m	[m/s]	6.852	7.009	7.651
Cup 5m	[m/s]	6.047	6.192	6.816
Cup 2m	[m/s]	4.848	5.055	5.490
Cup 1m	[m/s]	4.067	4.219	4.562
Dir. 10m	deg.	223.506	217.492	223.395
Dir. 2m	deg.	219.801	215.418	220.372
Temp 10m	[^{o}C]	19.560	19.551	19.295
Temp 2m	[^{o}C]	19.804	19.764	19.553
RH 10m	[%]	80.019	80.337	82.652
RH 6m	[%]	80.894	81.234	83.035
RH 2m	[%]	80.011	80.603	82.525
Abs Hum 10m	[g H_2O/m^3]	13.473	13.519	13.701
Abs Hum 2m	[g H_2O/m^3]	13.666	13.734	13.888
TC 9m	[^{o}C]	19.576	19.526	19.309
TC 7m	[^{o}C]	19.616	19.556	19.356
TC 5m	[^{o}C]	19.763	19.693	19.502
TC 320cm	[^{o}C]	19.755	19.657	19.499
TC 160cm	[^{o}C]	19.836	19.677	19.607
TC 80cm	[^{o}C]	19.999	19.802	19.793
TC 40cm	[^{o}C]	20.085	19.838	19.885
TC 20cm	[^{o}C]	20.151	19.853	19.969
TC 10cm	[^{o}C]	20.131	19.923	20.097
TC 5cm	[^{o}C]	20.491	20.022	20.400
T surface	[^{o}C]	19.566	19.286	19.608
U	[m/s]	6.810	7.089	7.664
σ_u^2	[m^2/s^2]	1.532	0.790	1.852
σ_v^2	[m^2/s^2]	1.315	0.523	1.185
σ_w^2	[m^2/s^2]	0.263	0.259	0.370
σ_T^2	[K^2]	0.011	0.005	0.020
u_*	[m/s]	0.502	0.320	0.421
$\overline{w't'}$	[m/s K]	0.022	0.010	0.018
L	[m]	-434.163	-257.224	-313.290

Table 23. Key meteorological parameters measured during the experiments. The upper part represents the profile measurements and the lower part represents micrometeorological paramters measured by the sonic

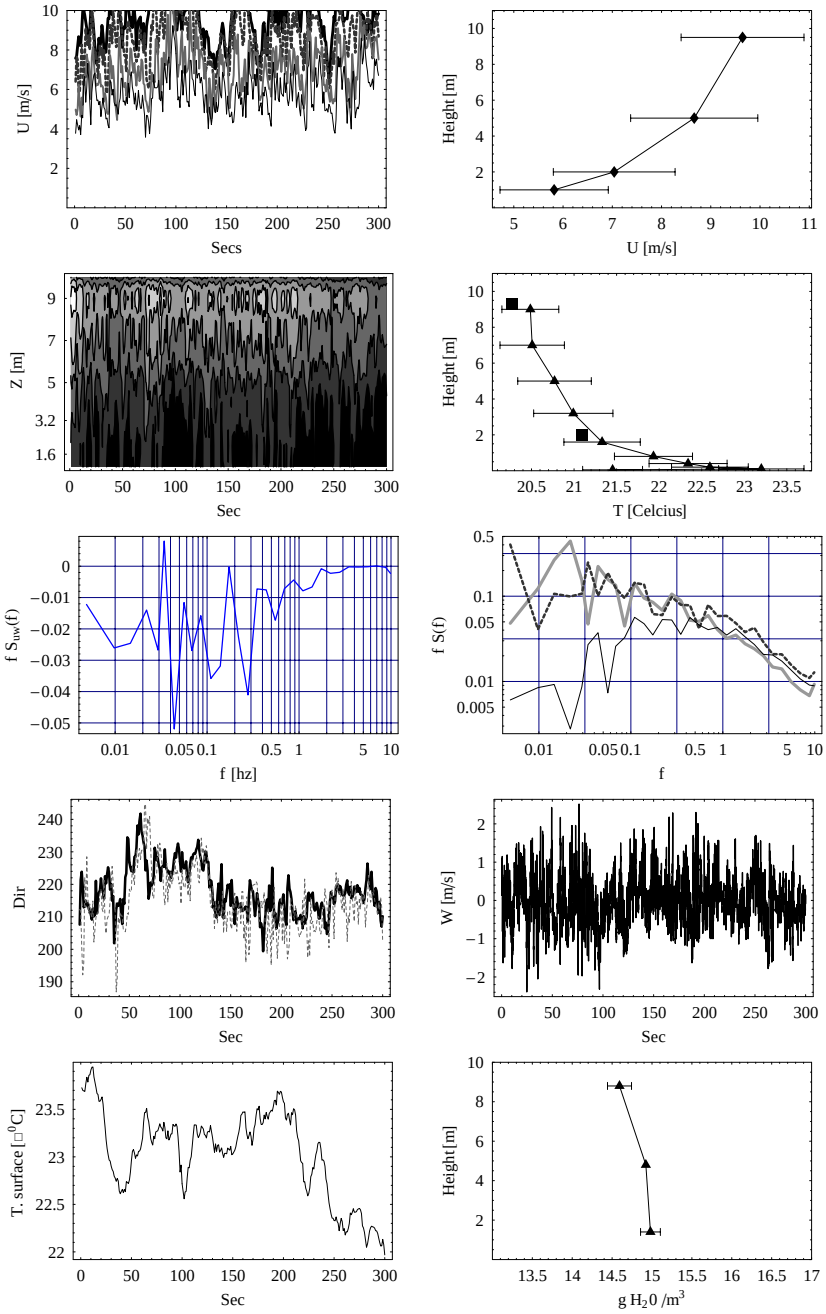

Figure 33. Overview of the meteorology during the release. In the first row is shown the wind-speed time series and the corresponding averaged wind profile. Second row shows time series of the temperature contours measured by the thermocouples and the corresponding temperature profile, the boxes shows the pt100 temperature. Third row shows the co-spectrum of $u'w'$ and the power spectra of u, v, w. The fourth row shows time series of the wind directions measured at 10 and 2m and the second figure shows a time series of the vertical fluctuations w'. The fifth row shows a time series of the surface temperature and the profile of absolute humidity.

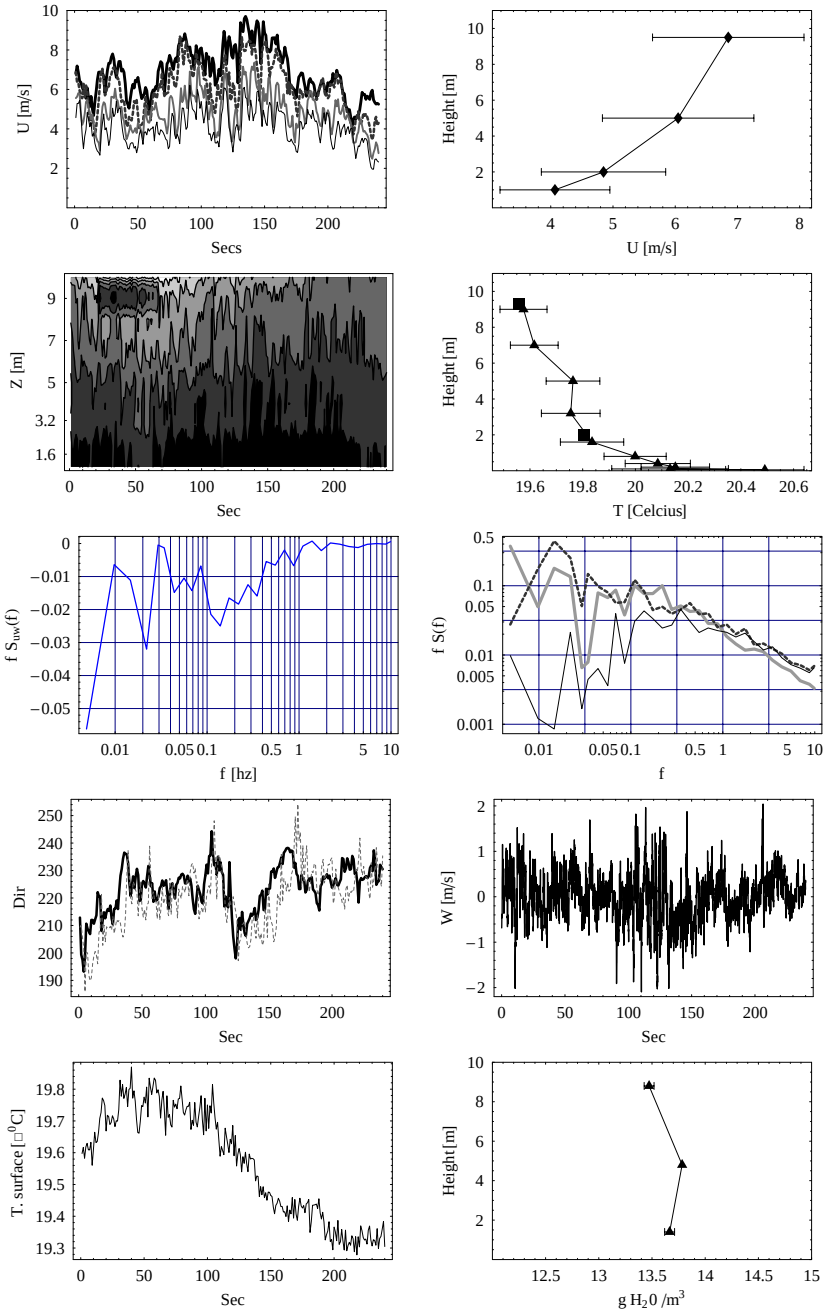

Figure 34. Overview of the meteorology during the release. In the first row is shown the wind-speed time series and the corresponding averaged wind profile. Second row shows time series of the temperature contours measured by the thermocouples and the corresponding temperature profile, the boxes shows the pt100 temperature. Third row shows the co-spectrum of $u'w'$ and the power spectra of u, v, w. The fourth row shows time series of the wind directions measured at 10 and 2m and the second figure shows a time series of the vertical fluctuations w'. The fifth row shows a time series of the surface temperature and the profile of absolute humidity.

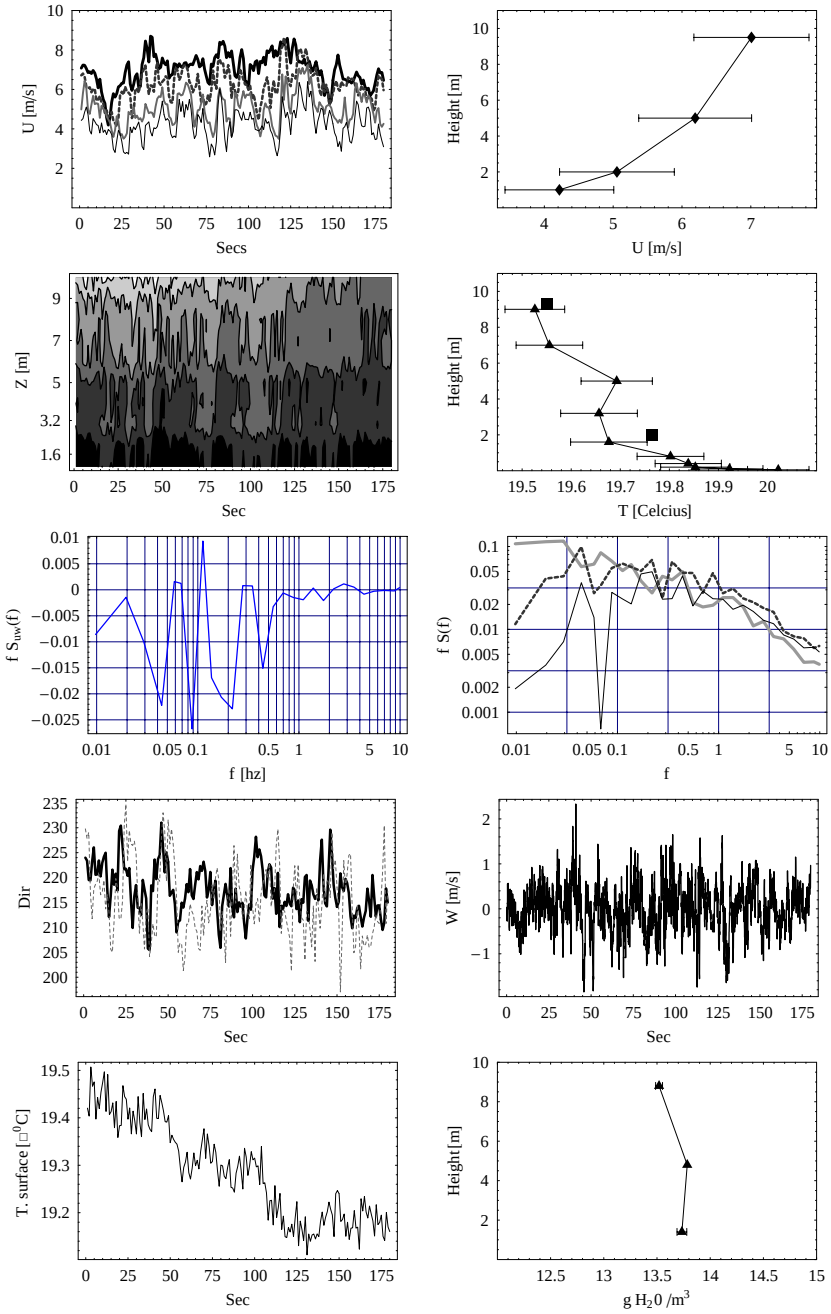

Figure 35. Overview of the meteorology during the release. In the first row is shown the wind-speed time series and the corresponding averaged wind profile. Second row shows time series of the temperature contours measured by the thermocouples and the corresponding temperature profile, the boxes shows the pt100 temperature. Third row shows the co-spectrum of $u'w'$ and the power spectra of u, v, w. The fourth row shows time series of the wind directions measured at 10 and 2m and the second figure shows a time series of the vertical fluctuations w'. The fifth row shows a time series of the surface temperature and the profile of absolute humidity.

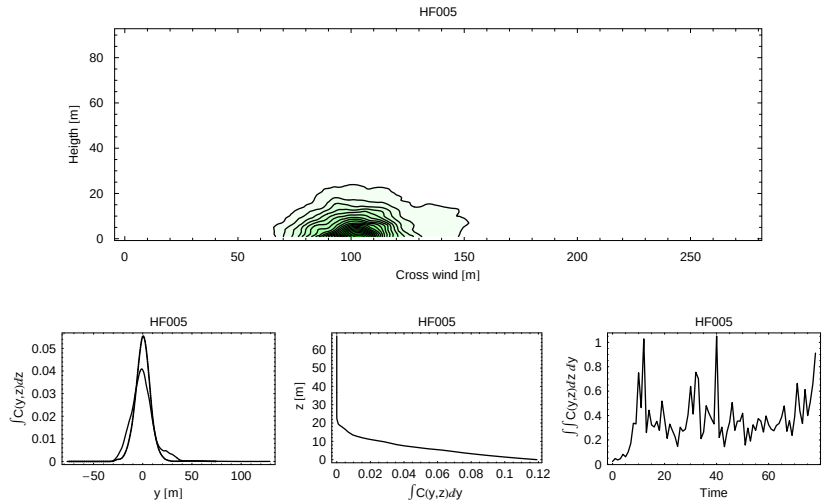

Figure 36. Overview of the measured HF plume profiles by the LIDAR. The top figure shows the contour lines of the mean profile. The bottom figures show : 1) The cross wind integrated profile in the vertical direction (thin line : fixed frame; thick line: moving frame). 2) The cross wind integrated profile in the horizontal direction.3) A timeserie of the cross wind integrated area of each LIDAR scan

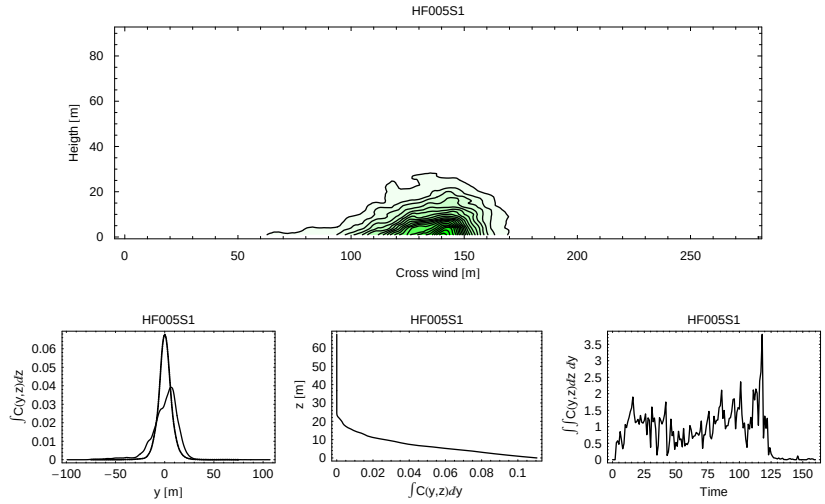

Figure 37. Overview of the measured smoke plume profiles by the LIDAR. The top figure shows the contour lines of the mean profile. The bottom figures show : 1) The cross wind integrated profile in the vertical direction (thin line : fixed frame; thick line: moving frame). 2) The cross wind integrated profile in the horizontal direction.3) A timeserie of the cross wind integrated area of each LIDAR scan

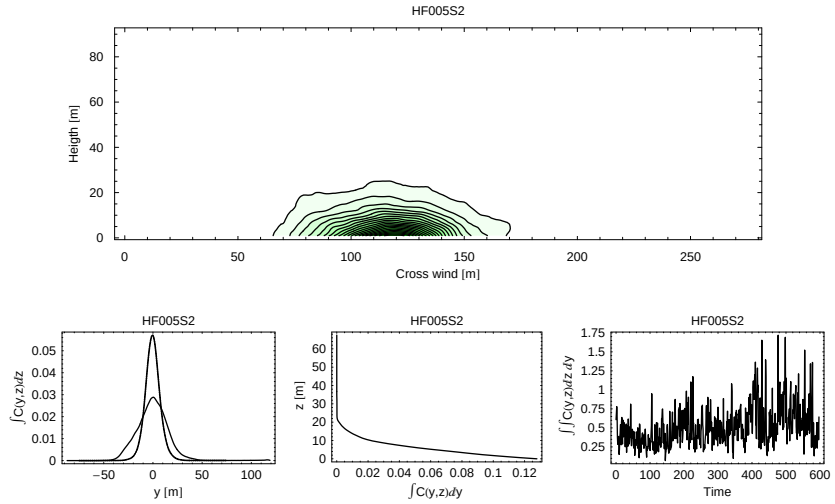

Figure 38. Overview of the measured smoke plume profiles by the LIDAR. The top figure shows the contour lines of the mean profile. The bottom figures show : 1) The cross wind integrated profile in the vertical direction (thin line : fixed frame; thick line: moving frame). 2) The cross wind integrated profile in the horizontal direction.3) A timeserie of the cross wind integrated area of each LIDAR scan

HF006

Comments: 7/8 cloud cover of light cumulus with spells of sunshine. Problems with the smoke machine.

Table 24. Timing

Release	Start	Stop	2D scans
HF006	16:29:19.35	16:32:25.93	95
HF006S1	16:38:07.73	16:48:42.73	321

Table 25. Plume parameters 100m downwind derived from lidar measurements

Parameter	Unit	HF006	HF006S1
$\overline{H}$	[m]	6.08	5.64
σ_z	[m]	3.48	3.37
σ_y	[m]	12.39	17.42
σ_{ym}	[m]	6.55	7.81

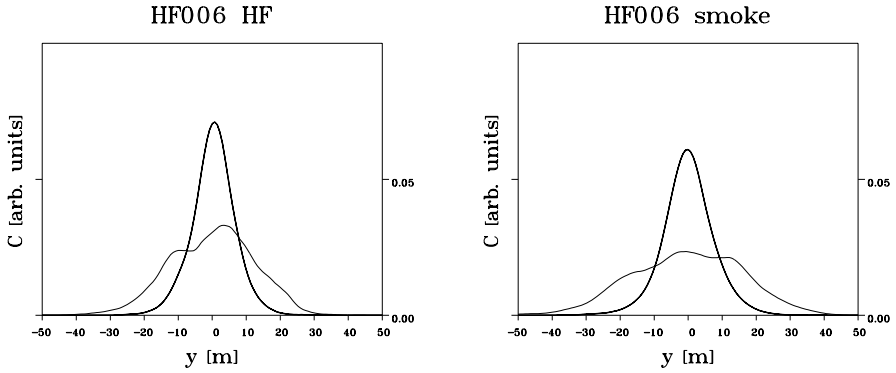

Figure 39. Depth integrated horizontal profiles from fixed frame analysis (thin line) and moving frame analysis (thick line).

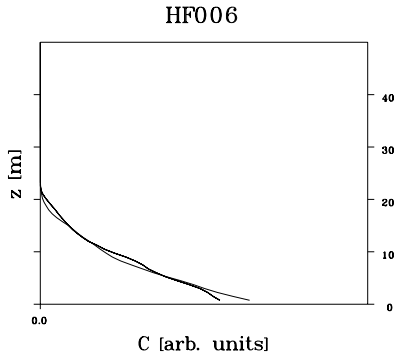

Figure 40. Cross-plume integrated vertical concentration profiles. Thin line: smoke, thick line: HF.

Parameter	Unit	HF006	HF006S1
Cup 10m	[m/s]	7.162	7.219
Cup 5m	[m/s]	6.405	6.458
Cup 2m	[m/s]	5.139	5.240
Cup 1m	[m/s]	4.199	4.407
Dir. 10m	deg.	226.767	216.942
Dir. 2m	deg.	226.114	214.521
Temp 10m	[^{o}C]	20.450	20.505
Temp 2m	[^{o}C]	21.185	21.209
RH 10m	[%]	75.506	75.748
RH 6m	[%]	74.998	75.312
RH 2m	[%]	73.808	74.044
Abs Hum 10m	[g H_2O/m^3]	13.392	13.477
Abs Hum 2m	[g H_2O/m^3]	13.662	13.723
TC 9m	[^{o}C]	20.600	20.600
TC 7m	[^{o}C]	20.683	20.678
TC 5m	[^{o}C]	20.870	20.900
TC 320cm	[^{o}C]	20.968	20.975
TC 160cm	[^{o}C]	21.311	21.268
TC 80cm	[^{o}C]	21.824	21.709
TC 40cm	[^{o}C]	22.105	21.982
TC 20cm	[^{o}C]	22.342	22.211
TC 10cm	[^{o}C]	22.727	22.544
TC 5cm	[^{o}C]	23.711	23.454
T surface	[^{o}C]	22.171	22.145
U	[m/s]	7.111	7.187
σ_u^2	[m^2/s^2]	1.320	1.266
σ_v^2	[m^2/s^2]	1.133	1.148
σ_w^2	[m^2/s^2]	0.253	0.320
σ_T^2	[K^2]	0.083	0.135
u_*	[m/s]	0.407	0.487
$\overline{w't'}$	[m/s K]	0.067	0.078
L	[m]	-75.802	-111.974

Table 26. Key meteorological parameters measured during the experiments. The upper part represents the profile measurements and the lower part represents micrometeorological paramters measured by the sonic

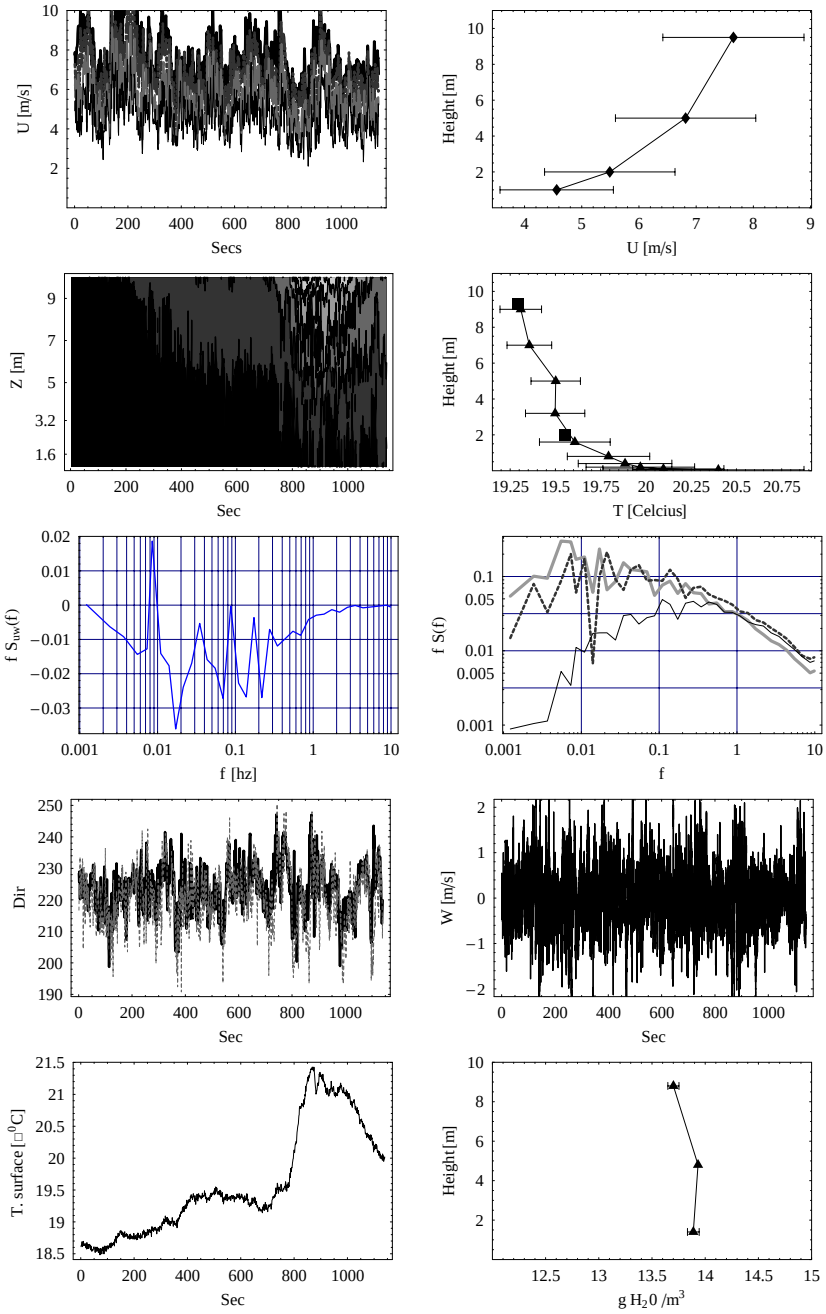

Figure 41. Overview of the meteorology during the release. In the first row is shown the wind-speed time series and the corresponding averaged wind profile. Second row shows time series of the temperature contours measured by the thermocouples and the corresponding temperature profile, the boxes shows the pt100 temperature. Third row shows the co-spectrum of $u'w'$ and the power spectra of u, v, w. The fourth row shows time series of the wind directions measured at 10 and 2m and the second figure shows a time series of the vertical fluctuations w'. The fifth row shows a time series of the surface temperature and the profile of absolute humidity.

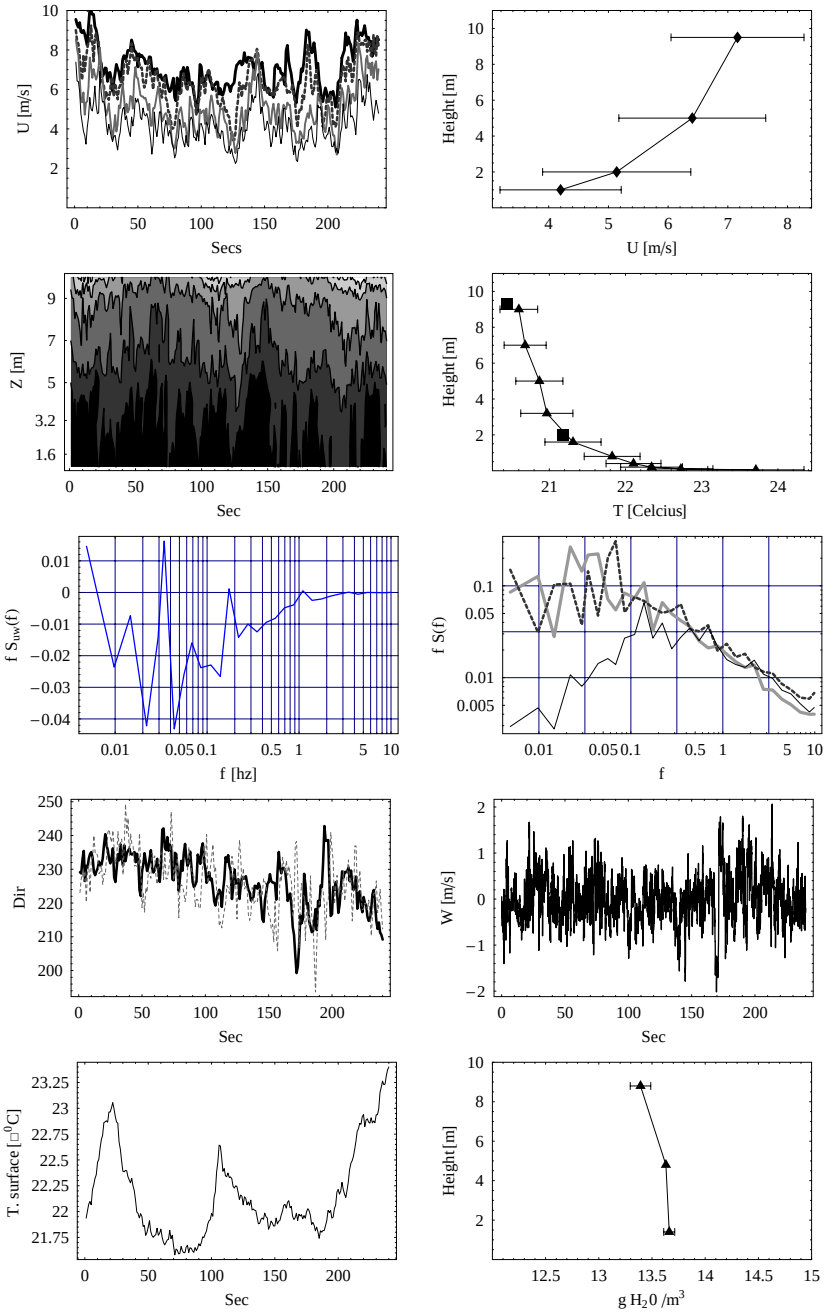

Figure 42. Overview of the meteorology during the release. In the first row is shown the wind-speed time series and the corresponding averaged wind profile. Second row shows time series of the temperature contours measured by the thermocouples and the corresponding temperature profile, the boxes shows the pt100 temperature. Third row shows the co-spectrum of $u'w'$ and the power spectra of u, v, w. The fourth row shows time series of the wind directions measured at 10 and 2m and the second figure shows a time series of the vertical fluctuations w'. The fifth row shows a time series of the surface temperature and the profile of absolute humidity.

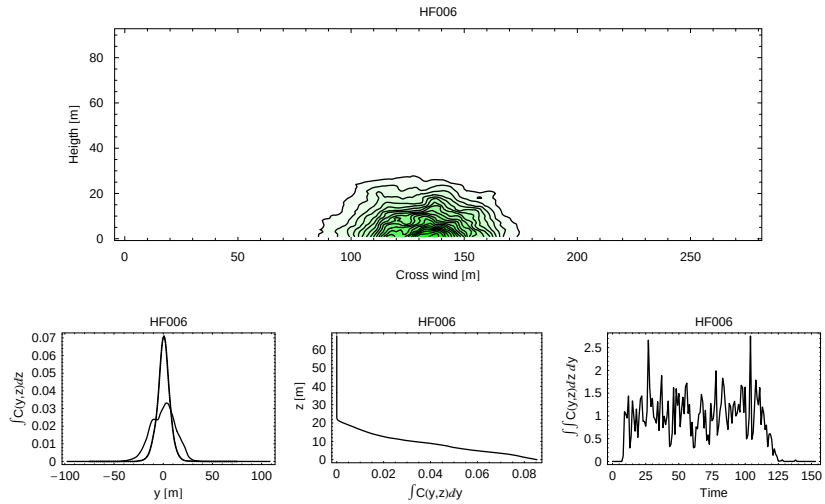

Figure 43. Overview of the measured HF plume profiles by the LIDAR. The top figure shows the contour lines of the mean profile. The bottom figures show : 1) The cross wind integrated profile in the vertical direction (thin line : fixed frame; thick line: moving frame). 2) The cross wind integrated profile in the horizontal direction.3) A timeserie of the cross wind integrated area of each LIDAR scan

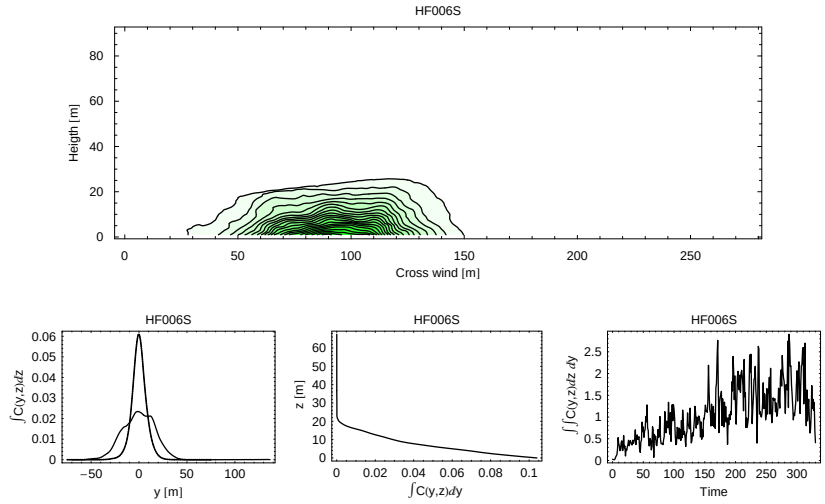

Figure 44. Overview of the measured smoke plume profiles by the LIDAR. The top figure shows the contour lines of the mean profile. The bottom figures show : 1) The cross wind integrated profile in the vertical direction (thin line : fixed frame; thick line: moving frame). 2) The cross wind integrated profile in the horizontal direction.3) A timeserie of the cross wind integrated area of each LIDAR scan

HF007

Comments:4/8 cloud cover of scattered cumulus, sunshine and low humidity. Very unstable with fluctuating wind. Smoke interrupted an postponed for 15 minutes because of bad wind direction.

Table 27. Timing

Release	Start	Stop	2D scans
HF007	11:18:25.00	11:20:30.34	62
HF007S1	11:44:43.78	12:00:22.68	523

Table 28. Plume parameters 100m downwind derived from lidar measurements

Parameter	Unit	HF007	HF007S1
$\overline{H}$	[m]	7.03	6.91
σ_z	[m]	3.43	4.52
σ_y	[m]	13.92	18.36
σ_{ym}	[m]	6.67	7.78

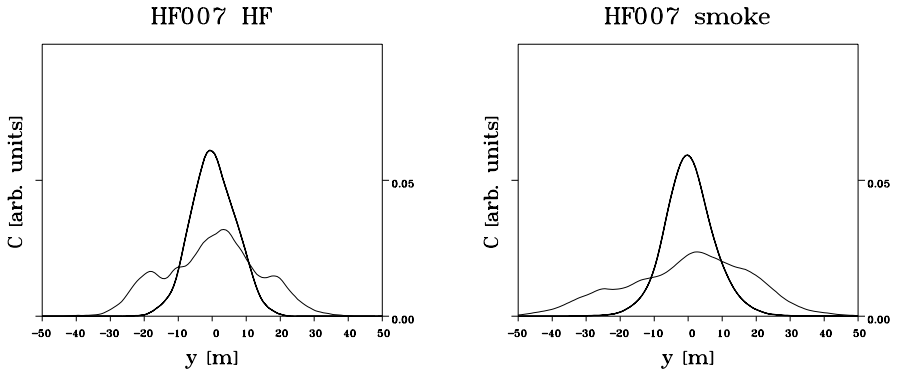

Figure 45. Depth integrated horizontal profiles from fixed frame analysis (thin line) and moving frame analysis (thick line).

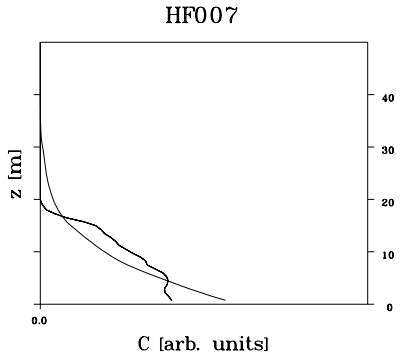

Figure 46. Cross-plume integrated vertical concentration profiles. Thin line: smoke, thick line: HF.

Parameter	Unit	HF007	HF007S1
Cup 10m	[m/s]	4.168	5.212
Cup 5m	[m/s]	3.951	4.766
Cup 2m	[m/s]	3.379	4.003
Cup 1m	[m/s]	2.847	3.390
Dir. 10m	deg.	238.209	247.516
Dir. 2m	deg.	237.747	245.430
Temp 10m	[^{o}C]	18.858	19.542
Temp 2m	[^{o}C]	19.892	20.696
RH 10m	[%]	55.554	59.932
RH 6m	[%]	57.421	52.196
RH 2m	[%]	52.561	48.513
Abs Hum 10m	[g H_2O/m^3]	8.975	10.079
Abs Hum 2m	[g H_2O/m^3]	9.023	8.728
TC 9m	[^{o}C]	19.233	19.868
TC 7m	[^{o}C]	19.347	20.023
TC 5m	[^{o}C]	19.623	20.185
TC 320cm	[^{o}C]	20.082	20.609
TC 160cm	[^{o}C]	20.451	21.107
TC 80cm	[^{o}C]	21.530	22.258
TC 40cm	[^{o}C]	22.289	22.901
TC 20cm	[^{o}C]	22.865	23.429
TC 10cm	[^{o}C]	24.096	24.640
TC 5cm	[^{o}C]	26.187	26.665
T surface	[^{o}C]	25.474	26.453
U	[m/s]	4.243	5.288
σ_u^2	[m^2/s^2]	0.573	1.421
σ_v^2	[m^2/s^2]	0.574	0.788
σ_w^2	[m^2/s^2]	0.209	0.251
σ_T^2	[K^2]	0.294	0.375
u_*	[m/s]	0.393	0.363
$\overline{w't'}$	[m/s K]	0.134	0.149
L	[m]	-33.915	-24.075

Table 29. Key meteorological parameters measured during the experiments. The upper part represents the profile measurements and the lower part represents micrometeorological paramters measured by the sonic

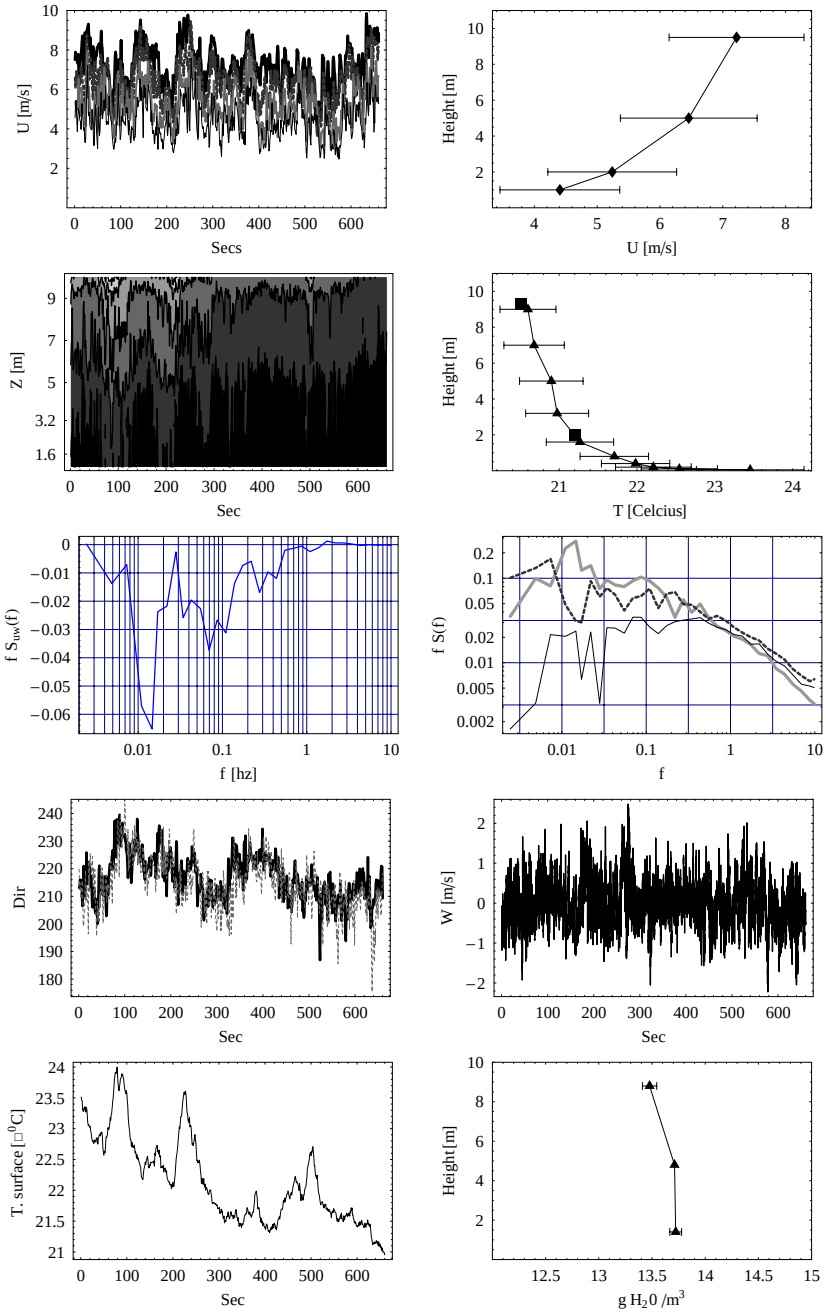

Figure 47. Overview of the meteorology during the release. In the first row is shown the wind-speed time series and the corresponding averaged wind profile. Second row shows time series of the temperature contours measured by the thermocouples and the corresponding temperature profile, the boxes shows the pt100 temperature. Third row shows the co-spectrum of $u'w'$ and the power spectra of u, v, w. The fourth row shows time series of the wind directions measured at 10 and 2m and the second figure shows a time series of the vertical fluctuations w'. The fifth row shows a time series of the surface temperature and the profile of absolute humidity.

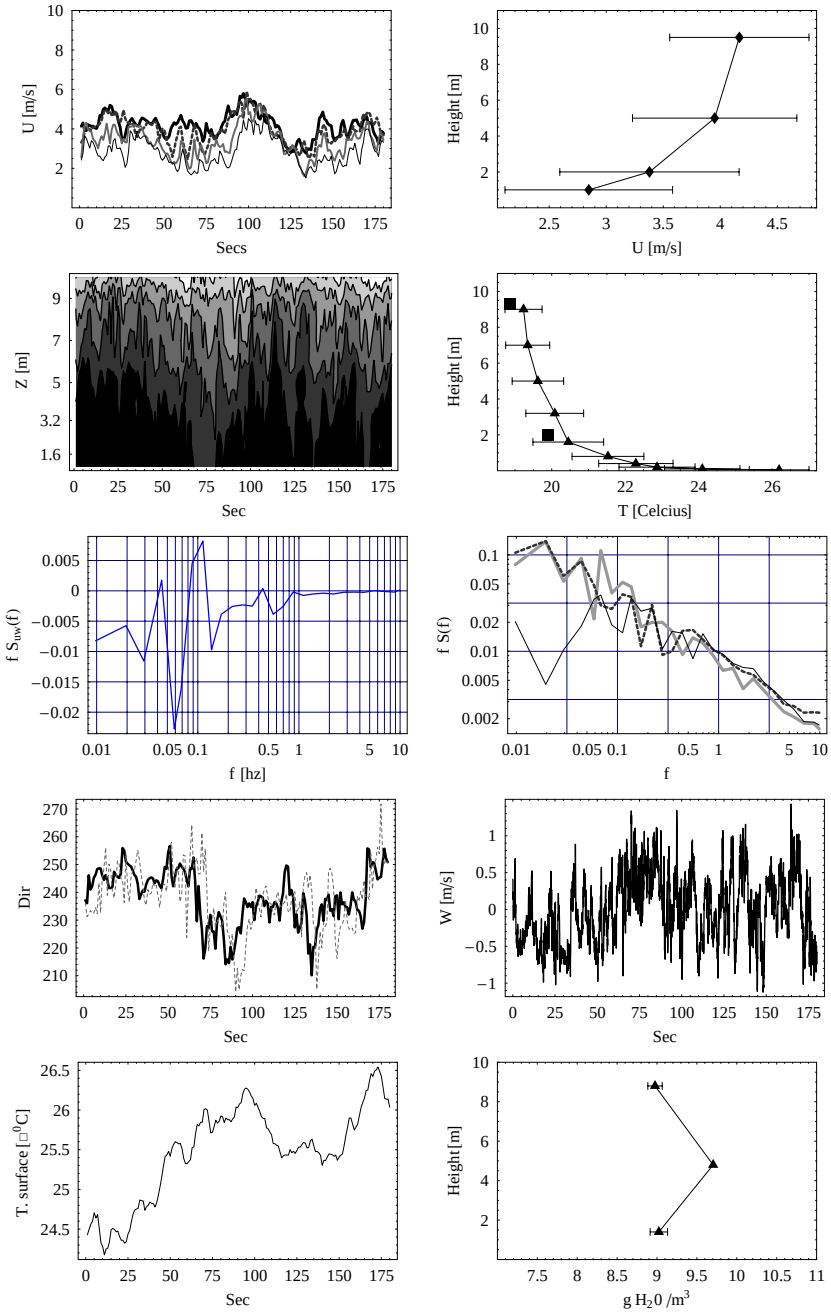

Figure 48. Overview of the meteorology during the release. In the first row is shown the wind-speed time series and the corresponding averaged wind profile. Second row shows time series of the temperature contours measured by the thermocouples and the corresponding temperature profile, the boxes shows the pt100 temperature. Third row shows the co-spectrum of $u'w'$ and the power spectra of u, v, w. The fourth row shows time series of the wind directions measured at 10 and 2m and the second figure shows a time series of the vertical fluctuations w'. The fifth row shows a time series of the surface temperature and the profile of absolute humidity.

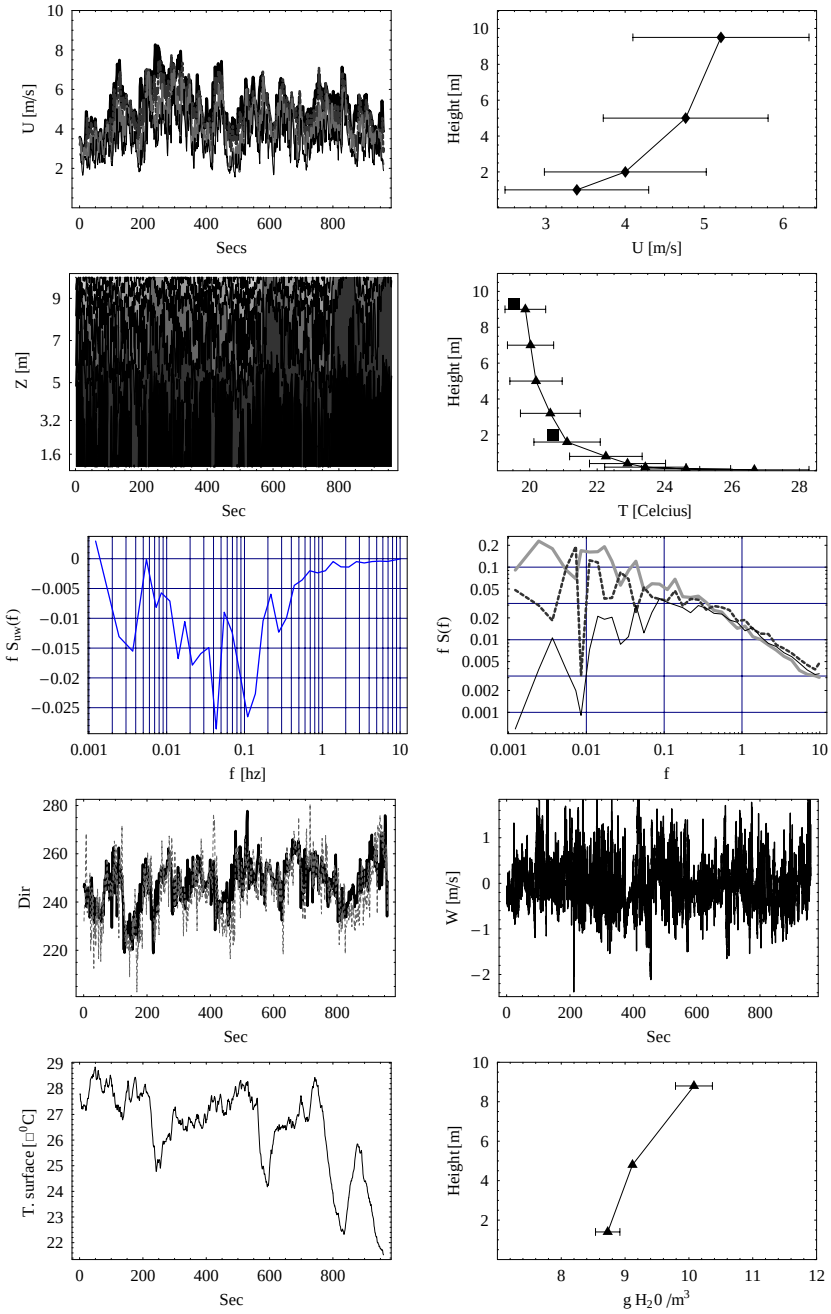

Figure 49. Overview of the meteorology during the release. In the first row is shown the wind-speed time series and the corresponding averaged wind profile. Second row shows time series of the temperature contours measured by the thermocouples and the corresponding temperature profile, the boxes shows the pt100 temperature. Third row shows the co-spectrum of $u'w'$ and the power spectra of u, v, w. The fourth row shows time series of the wind directions measured at 10 and 2m and the second figure shows a time series of the vertical fluctuations w'. The fifth row shows a time series of the surface temperature and the profile of absolute humidity.

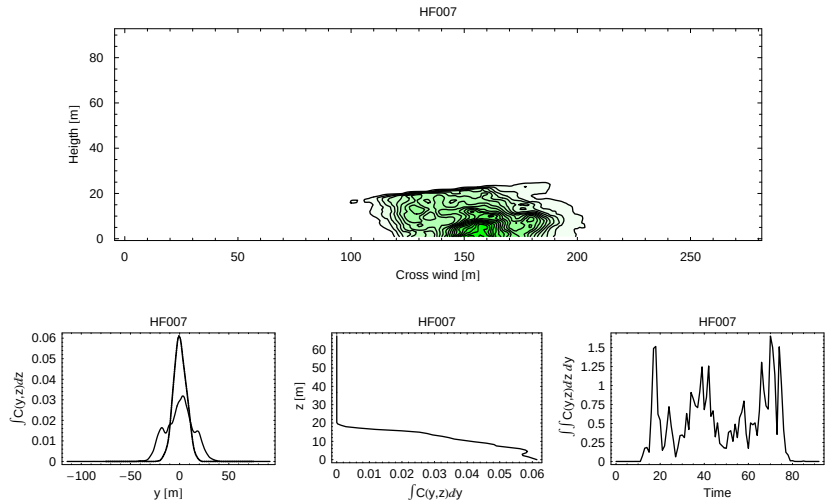

Figure 50. Overview of the measured HF plume profiles by the LIDAR. The top figure shows the contour lines of the mean profile. The bottom figures show : 1) The cross wind integrated profile in the vertical direction (thin line : fixed frame; thick line: moving frame). 2) The cross wind integrated profile in the horizontal direction.3) A timeserie of the cross wind integrated area of each LIDAR scan

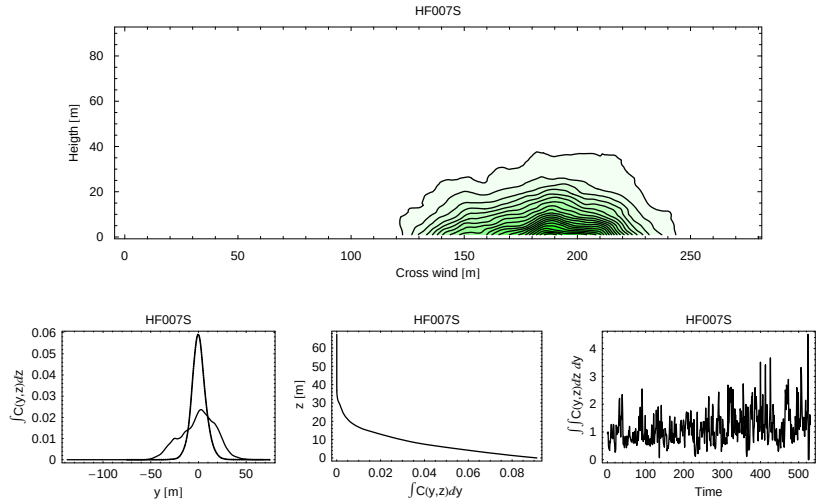

Figure 51. Overview of the measured smoke plume profiles by the LIDAR. The top figure shows the contour lines of the mean profile. The bottom figures show : 1) The cross wind integrated profile in the vertical direction (thin line : fixed frame; thick line: moving frame). 2) The cross wind integrated profile in the horizontal direction.3) A timeserie of the cross wind integrated area of each LIDAR scan

HF008

Comments:Light (2/8) cloud cover consisting of both high and low clouds. Sunshine. No signs of lift off.

Table 30. Timing

Release	Start	Stop	2D scans
HF008	09:32:25.40	09:35:35.11	124
HF008S1	09:38:48.18	09:46:13.90	290
HF008S2	09:46:30.54	09:55:04.09	334
HF008S3	09:55:31.50	10:03:13.97	301

Table 31. Plume parameters 100m downwind derived from lidar measurements

Parameter	Unit	HF008	HF008S1	HF008S2	HF008S3
$\overline{H}$	[m]	8.15	6.72	6.66	8.60
σ_z	[m]	4.77	4.31	4.21	5.58
σ_y	[m]	13.02	17.04	25.47	13.42
σ_{ym}	[m]	6.86	8.14	8.94	7.64

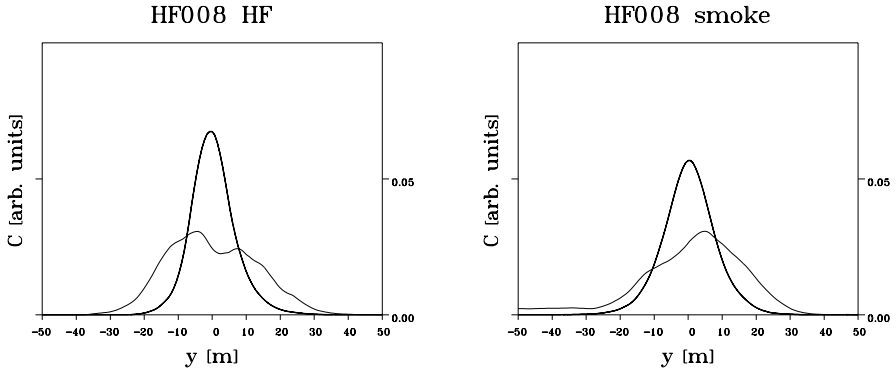

Figure 52. Depth integrated horizontal profiles from fixed frame analysis (thin line) and moving frame analysis (thick line).

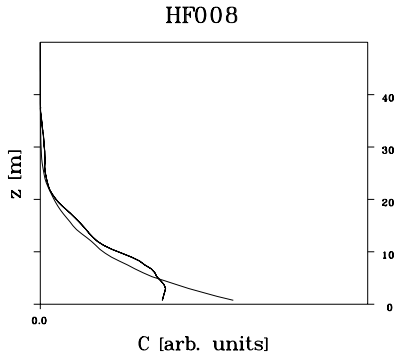

Figure 53. Cross-plume integrated vertical concentration profiles. Thin line: smoke, thick line: HF.

Parameter	Unit	HF008	HF008S1	HF008S2	HF008S3
Cup 10m	[m/s]	3.810	4.597	4.505	4.200
Cup 5m	[m/s]	3.357	4.246	4.128	3.995
Cup 2m	[m/s]	2.813	3.507	3.459	3.418
Cup 1m	[m/s]	2.396	2.971	2.975	2.899
Dir. 10m	deg.	240.242	240.649	238.639	234.098
Dir. 2m	deg.	238.321	240.548	238.827	232.203
Temp 10m	[^{o}C]	16.797	17.204	17.503	17.674
Temp 2m	[^{o}C]	17.414	18.110	18.355	18.689
RH 10m	[%]	77.455	72.323	70.134	69.393
RH 6m	[%]	77.532	72.845	70.386	69.390
RH 2m	[%]	75.970	69.942	67.838	66.476
Abs Hum 10m	[g H_2O/m^3]	11.069	10.590	10.454	10.450
Abs Hum 2m	[g H_2O/m^3]	11.265	10.810	10.637	10.632
TC 9m	[^{o}C]	17.238	17.635	17.820	18.029
TC 7m	[^{o}C]	17.177	17.586	17.779	17.992
TC 5m	[^{o}C]	17.507	17.902	18.125	18.296
TC 320cm	[^{o}C]	17.708	18.144	18.380	18.562
TC 160cm	[^{o}C]	17.875	18.445	18.624	18.953
TC 80cm	[^{o}C]	18.570	19.303	19.463	19.943
TC 40cm	[^{o}C]	19.142	19.945	20.164	20.688
TC 20cm	[^{o}C]	19.330	20.166	20.420	21.038
TC 10cm	[^{o}C]	20.160	21.127	21.429	22.082
TC 5cm	[^{o}C]	21.327	22.491	22.892	23.802
T surface	[^{o}C]	19.781	21.035	21.571	22.587
U	[m/s]	3.908	4.619	4.477	4.218
σ_u^2	[m^2/s^2]	0.231	0.833	0.801	0.589
σ_v^2	[m^2/s^2]	0.379	0.687	1.122	0.440
σ_w^2	[m^2/s^2]	0.172	0.190	0.204	0.177
σ_T^2	[K^2]	0.206	0.226	0.286	0.346
u_*	[m/s]	0.213	0.334	0.308	0.235
$\overline{w't'}$	[m/s K]	0.113	0.110	0.135	0.153
L	[m]	-6.308	-25.335	-16.123	-6.321

Table 32. Key meteorological parameters measured during the experiments. The upper part represents the profile measurements and the lower part represents micrometeorological paramters measured by the sonic

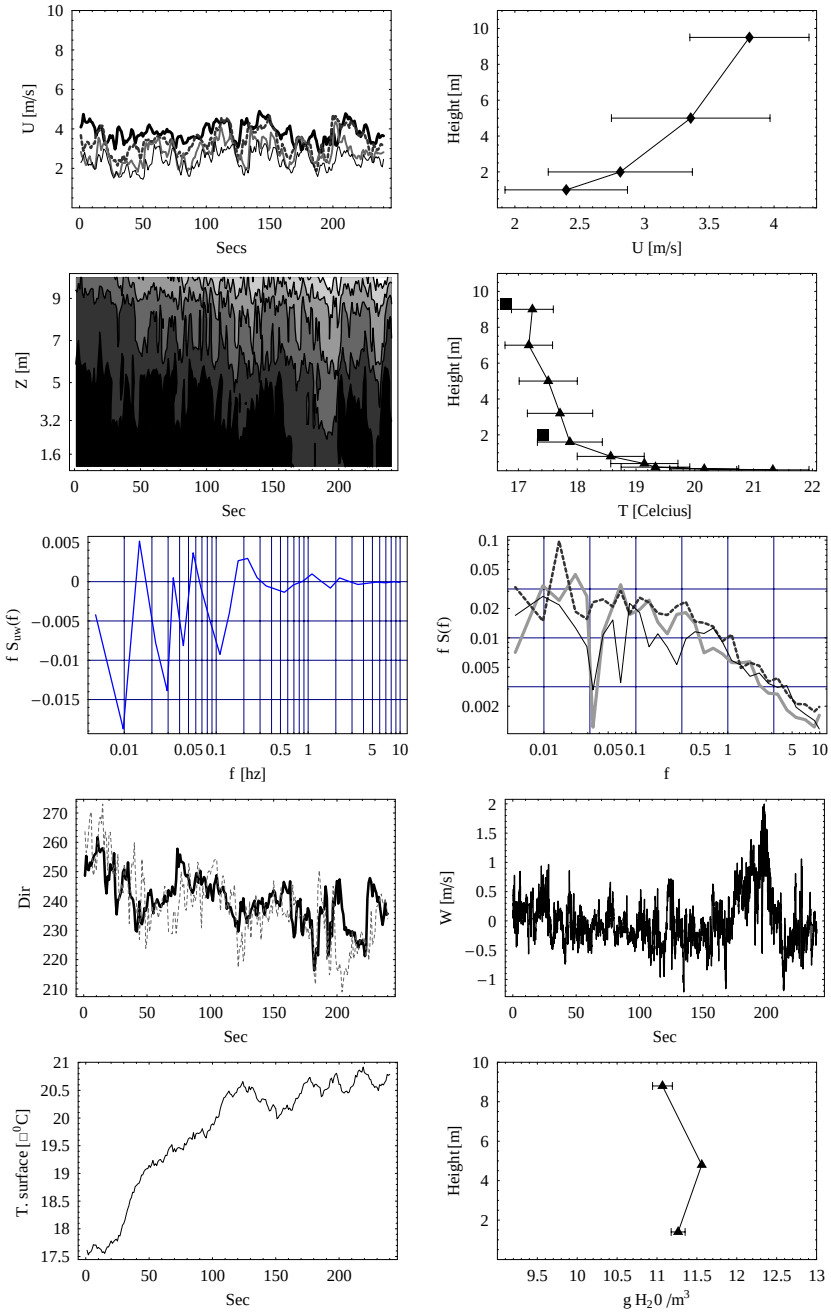

Figure 54. Overview of the meteorology during the release. In the first row is shown the wind-speed time series and the corresponding averaged wind profile. Second row shows time series of the temperature contours measured by the thermocouples and the corresponding temperature profile, the boxes shows the pt100 temperature. Third row shows the co-spectrum of $u'w'$ and the power spectra of u, v, w. The fourth row shows time series of the wind directions measured at 10 and 2m and the second figure shows a time series of the vertical fluctuations w'. The fifth row shows a time series of the surface temperature and the profile of absolute humidity.

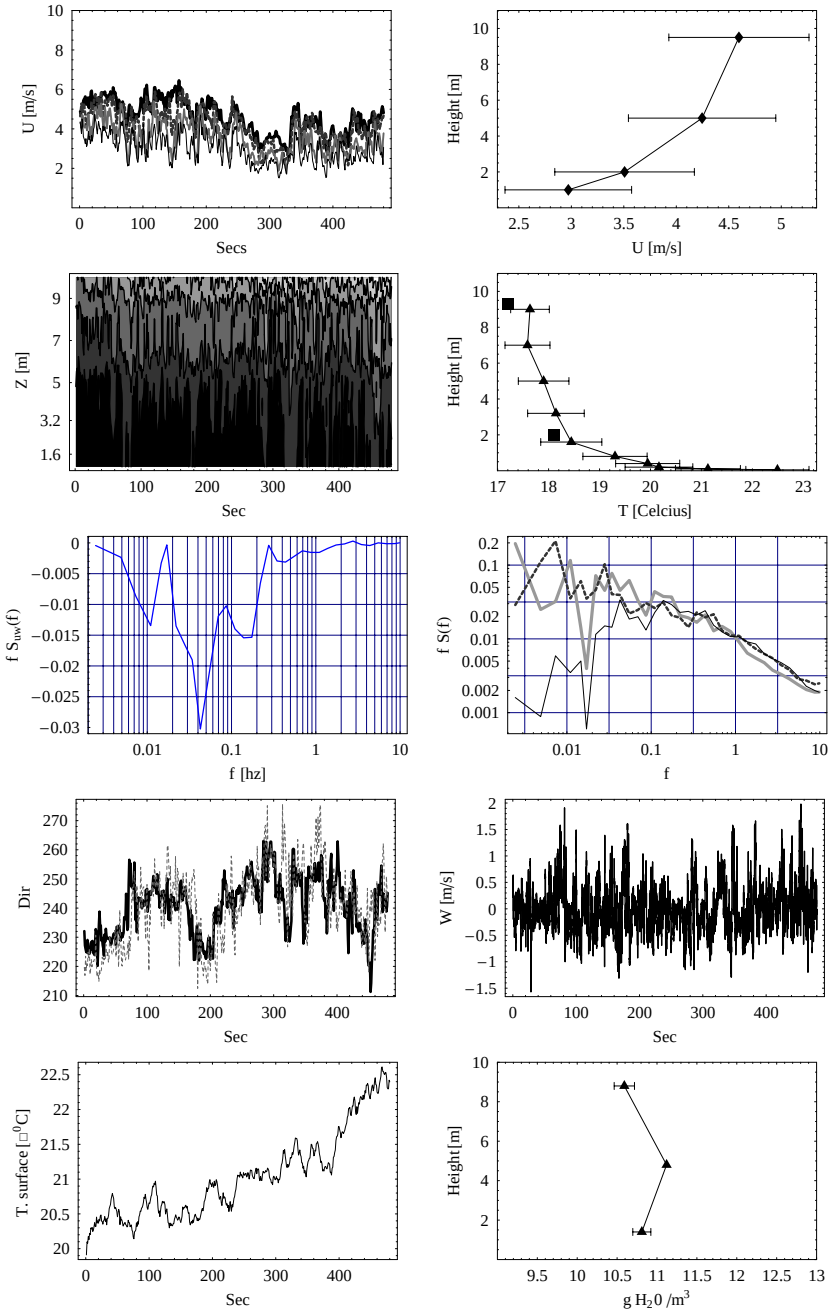

Figure 55. Overview of the meteorology during the release. In the first row is shown the wind-speed time series and the corresponding averaged wind profile. Second row shows time series of the temperature contours measured by the thermocouples and the corresponding temperature profile, the boxes shows the pt100 temperature. Third row shows the co-spectrum of $u'w'$ and the power spectra of u, v, w. The fourth row shows time series of the wind directions measured at 10 and 2m and the second figure shows a time series of the vertical fluctuations w'. The fifth row shows a time series of the surface temperature and the profile of absolute humidity.

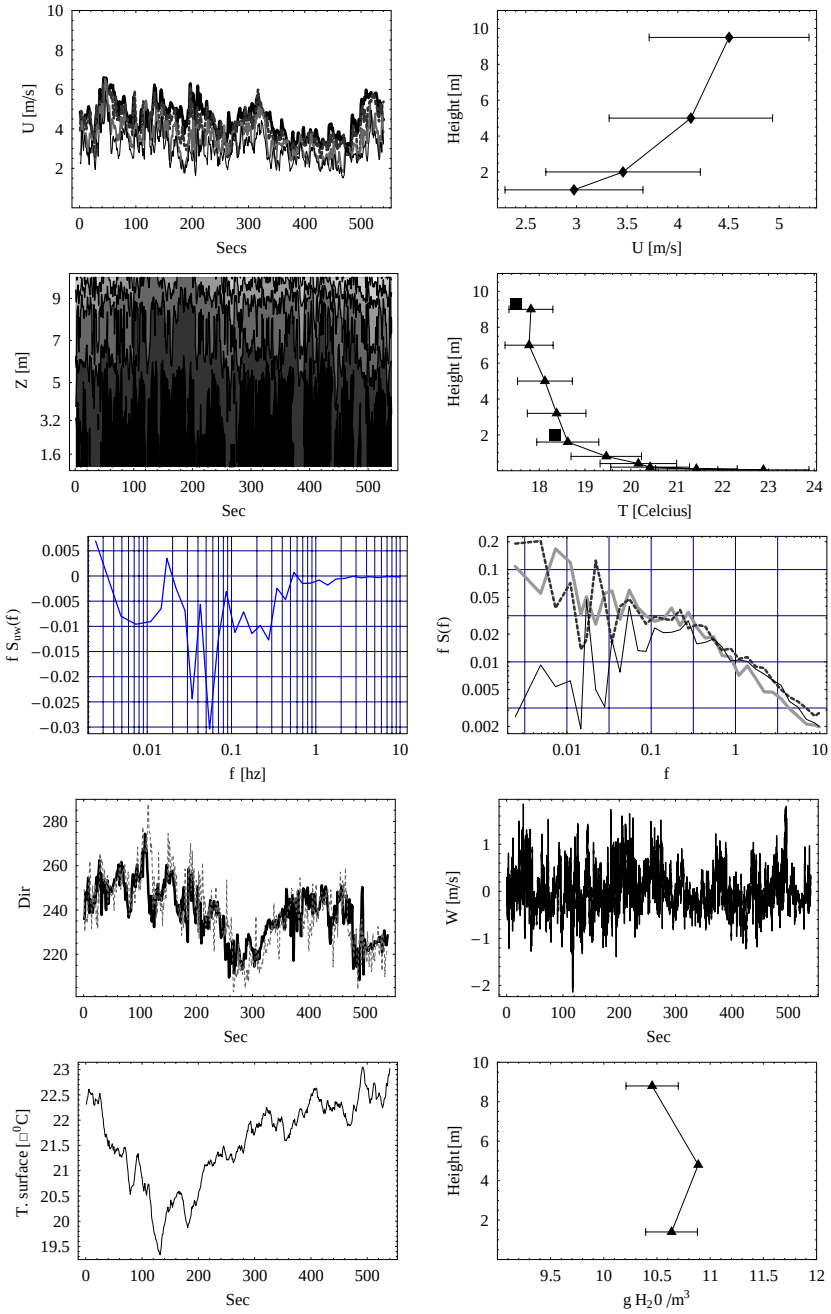

Figure 56. Overview of the meteorology during the release. In the first row is shown the wind-speed time series and the corresponding averaged wind profile. Second row shows time series of the temperature contours measured by the thermocouples and the corresponding temperature profile, the boxes shows the pt100 temperature. Third row shows the co-spectrum of $u'w'$ and the power spectra of u, v, w. The fourth row shows time series of the wind directions measured at 10 and 2m and the second figure shows a time series of the vertical fluctuations w'. The fifth row shows a time series of the surface temperature and the profile of absolute humidity.

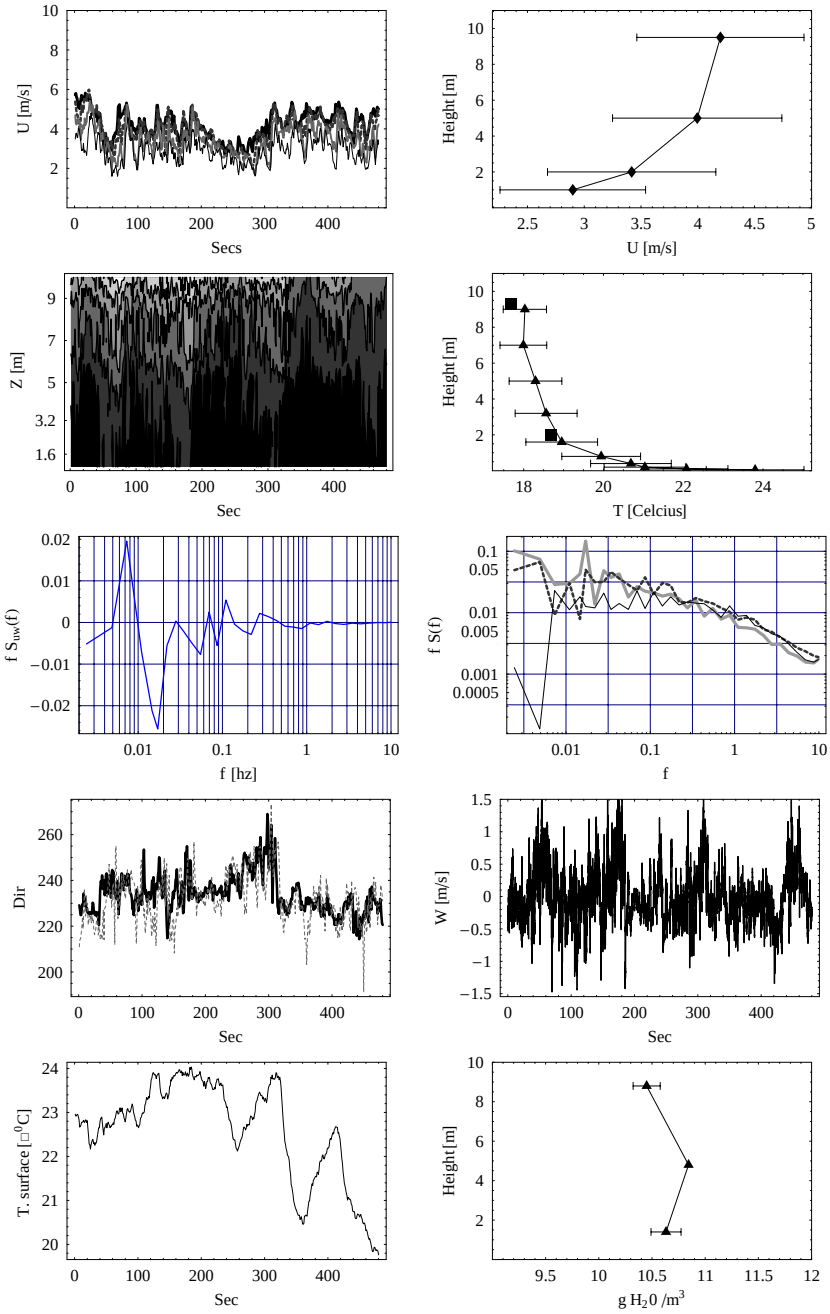

Figure 57. Overview of the meteorology during the release. In the first row is shown the wind-speed time series and the corresponding averaged wind profile. Second row shows time series of the temperature contours measured by the thermocouples and the corresponding temperature profile, the boxes shows the pt100 temperature. Third row shows the co-spectrum of $u'w'$ and the power spectra of u, v, w. The fourth row shows time series of the wind directions measured at 10 and 2m and the second figure shows a time series of the vertical fluctuations w'. The fifth row shows a time series of the surface temperature and the profile of absolute humidity.

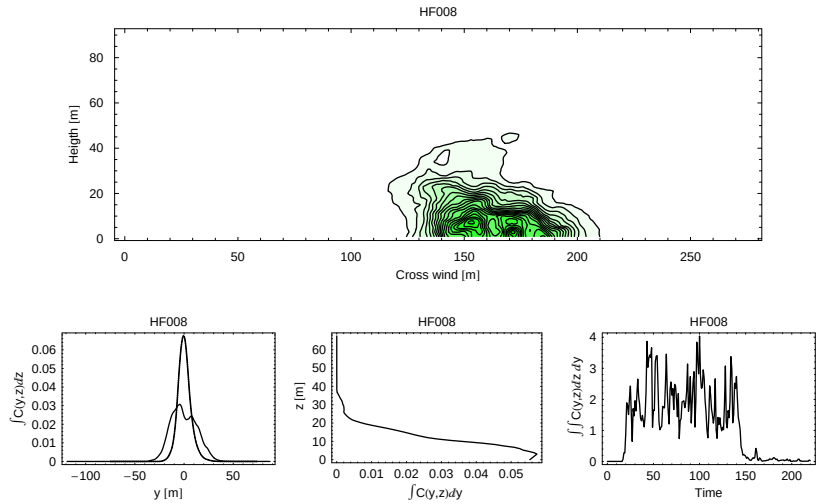

Figure 58. Overview of the measured HF plume profiles by the LIDAR. The top figure shows the contour lines of the mean profile. The bottom figures show : 1) The cross wind integrated profile in the vertical direction (thin line : fixed frame; thick line: moving frame). 2) The cross wind integrated profile in the horizontal direction.3) A timeserie of the cross wind integrated area of each LIDAR scan

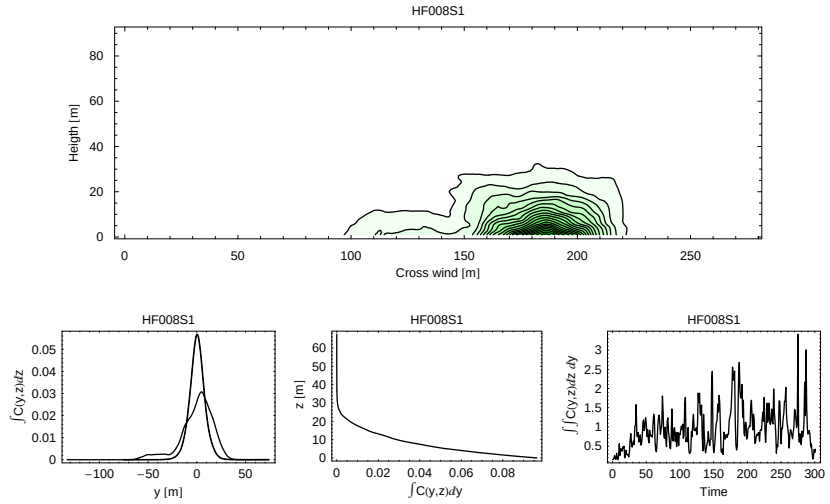

Figure 59. Overview of the measured smoke plume profiles by the LIDAR. The top figure shows the contour lines of the mean profile. The bottom figures show : 1) The cross wind integrated profile in the vertical direction (thin line : fixed frame; thick line: moving frame). 2) The cross wind integrated profile in the horizontal direction.3) A timeserie of the cross wind integrated area of each LIDAR scan

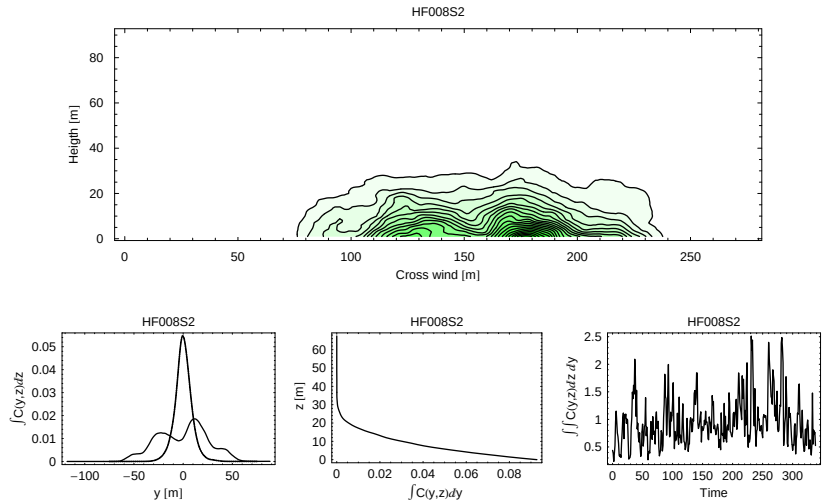

Figure 60. Overview of the measured smoke plume profiles by the LIDAR. The top figure shows the contour lines of the mean profile. The bottom figures show : 1) The cross wind integrated profile in the vertical direction (thin line : fixed frame; thick line: moving frame). 2) The cross wind integrated profile in the horizontal direction.3) A timeserie of the cross wind integrated area of each LIDAR scan

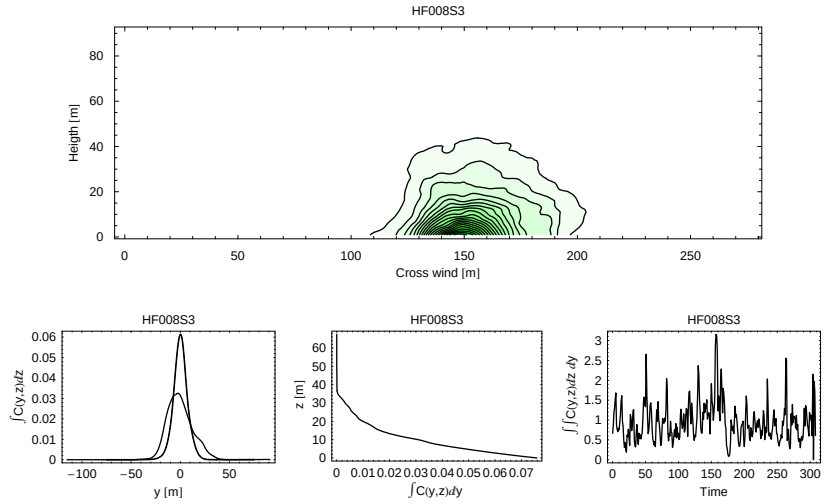

Figure 61. Overview of the measured smoke plume profiles by the LIDAR. The top figure shows the contour lines of the mean profile. The bottom figures show : 1) The cross wind integrated profile in the vertical direction (thin line : fixed frame; thick line: moving frame). 2) The cross wind integrated profile in the horizontal direction.3) A timeserie of the cross wind integrated area of each LIDAR scan

HF009

Comments:Quite windy and quite low humidity. 4/8 cover of cumulus. Sunshine. The HF was mixed with butane. No signs of lift-off and not much dense gas behaviour.

Table 33. Timing

Release	Start	Stop	2D scans
HF009	13:08:11.94	13:10:49.52	108
HF009S1	13:14:54.11	13:19:28.30	187
HF009S2	13:19:41.42	13:27:13.90	308
HF009S3	13:27:27.52	13:34:37.86	293

Table 34. Plume parameters 100m downwind derived from lidar measurements

Parameter	Unit	HF009	HF009S1	HF009S2	HF009S3
$\overline{H}$	[m]	4.29	5.78	4.77	4.99
σ_z	[m]	2.66	3.78	3.50	3.29
σ_y	[m]	16.93	14.81	19.36	25.58
σ_{ym}	[m]	6.14	8.13	8.83	8.75

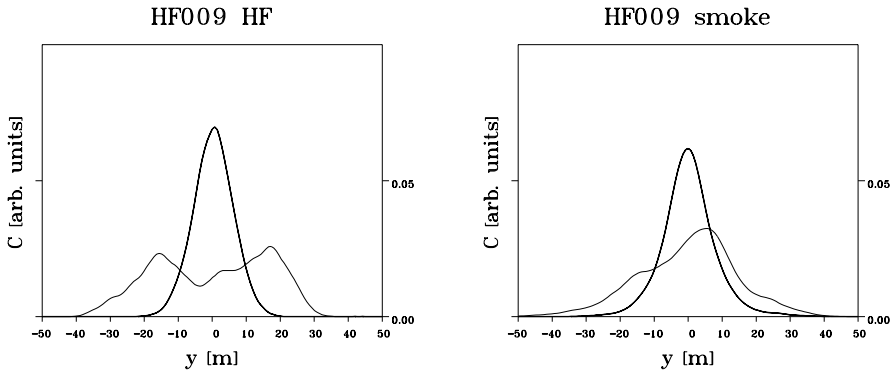

Figure 62. Depth integrated horizontal profiles from fixed frame analysis (thin line) and moving frame analysis (thick line).

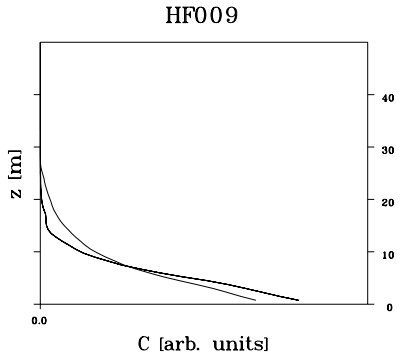

Figure 63. Cross-plume integrated vertical concentration profiles. Thin line: smoke, thick line: HF.

Parameter	Unit	HF009	HF009S1	HF009S2	HF009S3
Cup 10m	[m/s]	8.831	6.925	7.067	7.444
Cup 5m	[m/s]	7.790	6.336	6.534	6.750
Cup 2m	[m/s]	6.499	5.264	5.390	5.620
Cup 1m	[m/s]	5.485	4.411	4.471	4.636
Dir. 10m	deg.	238.802	226.413	225.724	228.911
Dir. 2m	deg.	238.429	224.176	222.179	227.360
Temp 10m	[^{o}C]	20.229	20.173	20.174	20.205
Temp 2m	[^{o}C]	21.569	21.190	21.186	21.410
RH 10m	[%]	70.157	72.089	73.200	73.565
RH 6m	[%]	50.668	51.547	52.111	52.366
RH 2m	[%]	46.435	47.897	48.619	48.001
Abs Hum 10m	[g H_2O/m^3]	12.284	12.581	12.775	12.863
Abs Hum 2m	[g H_2O/m^3]	8.789	8.869	8.999	9.001
TC 9m	[^{o}C]	20.382	20.431	20.442	20.587
TC 7m	[^{o}C]	20.501	20.499	20.497	20.702
TC 5m	[^{o}C]	20.764	20.708	20.702	20.905
TC 320cm	[^{o}C]	21.232	21.027	20.995	21.328
TC 160cm	[^{o}C]	21.796	21.526	21.473	22.003
TC 80cm	[^{o}C]	22.886	22.453	22.372	23.122
TC 40cm	[^{o}C]	23.360	22.908	22.829	23.698
TC 20cm	[^{o}C]	24.034	23.468	23.356	24.443
TC 10cm	[^{o}C]	24.993	24.293	24.165	25.413
TC 5cm	[^{o}C]	26.886	26.041	25.792	27.519
T surface	[^{o}C]	27.073	25.515	25.274	27.253
U	[m/s]	8.891	6.875	7.075	7.397
σ_u^2	[m^2/s^2]	1.733	1.734	1.147	0.928
σ_v^2	[m^2/s^2]	0.923	1.341	1.274	1.896
σ_w^2	[m^2/s^2]	0.290	0.372	0.342	0.302
σ_T^2	[K^2]	0.273	0.262	0.293	0.260
u_*	[m/s]	0.496	0.435	0.347	0.378
$\overline{w't'}$	[m/s K]	0.133	0.163	0.139	0.141
L	[m]	-69.009	-37.920	-22.730	-28.785

Table 35. Key meteorological parameters measured during the experiments. The upper part represents the profile measurements and the lower part represents micrometeorological paramters measured by the sonic

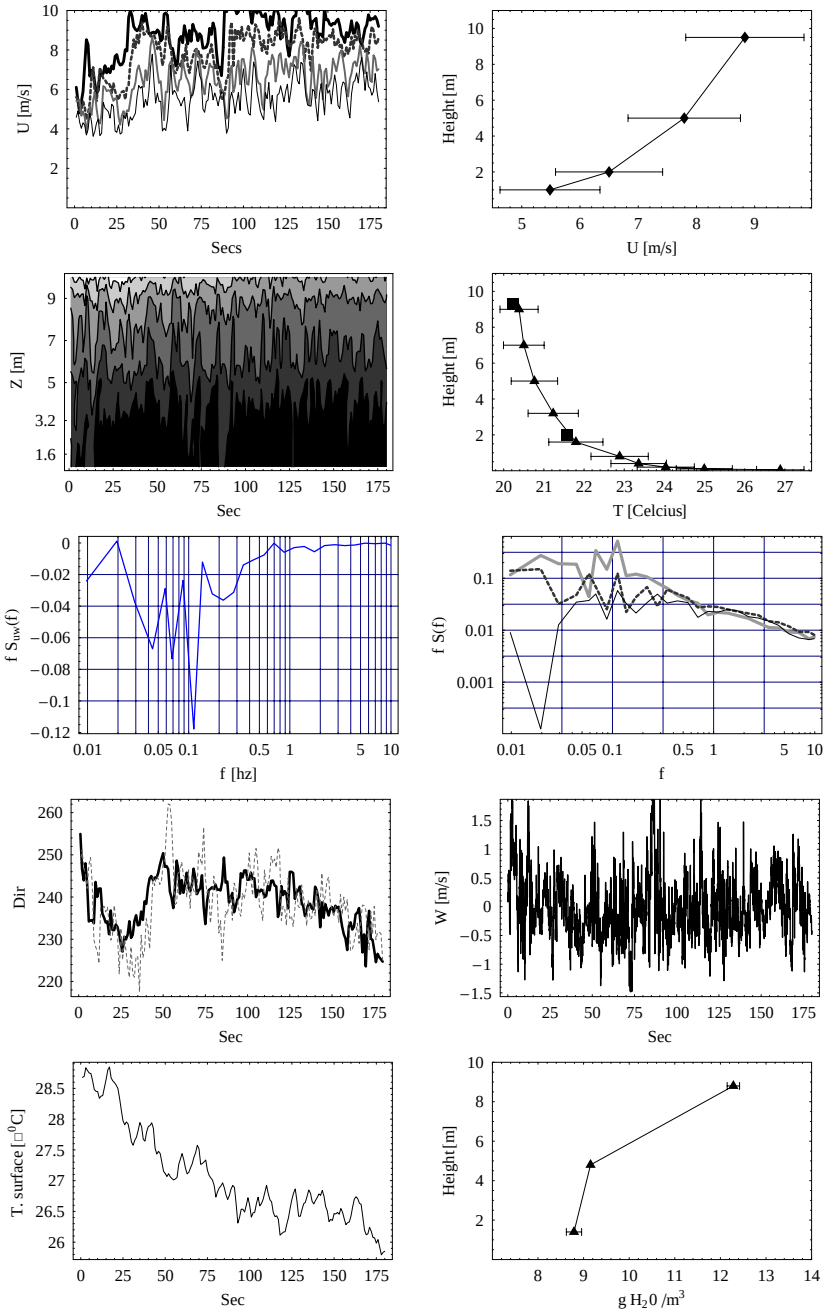

Figure 64. Overview of the meteorology during the release. In the first row is shown the wind-speed time series and the corresponding averaged wind profile. Second row shows time series of the temperature contours measured by the thermocouples and the corresponding temperature profile, the boxes shows the pt100 temperature. Third row shows the co-spectrum of $u'w'$ and the power spectra of u, v, w. The fourth row shows time series of the wind directions measured at 10 and 2m and the second figure shows a time series of the vertical fluctuations w'. The fifth row shows a time series of the surface temperature and the profile of absolute humidity.

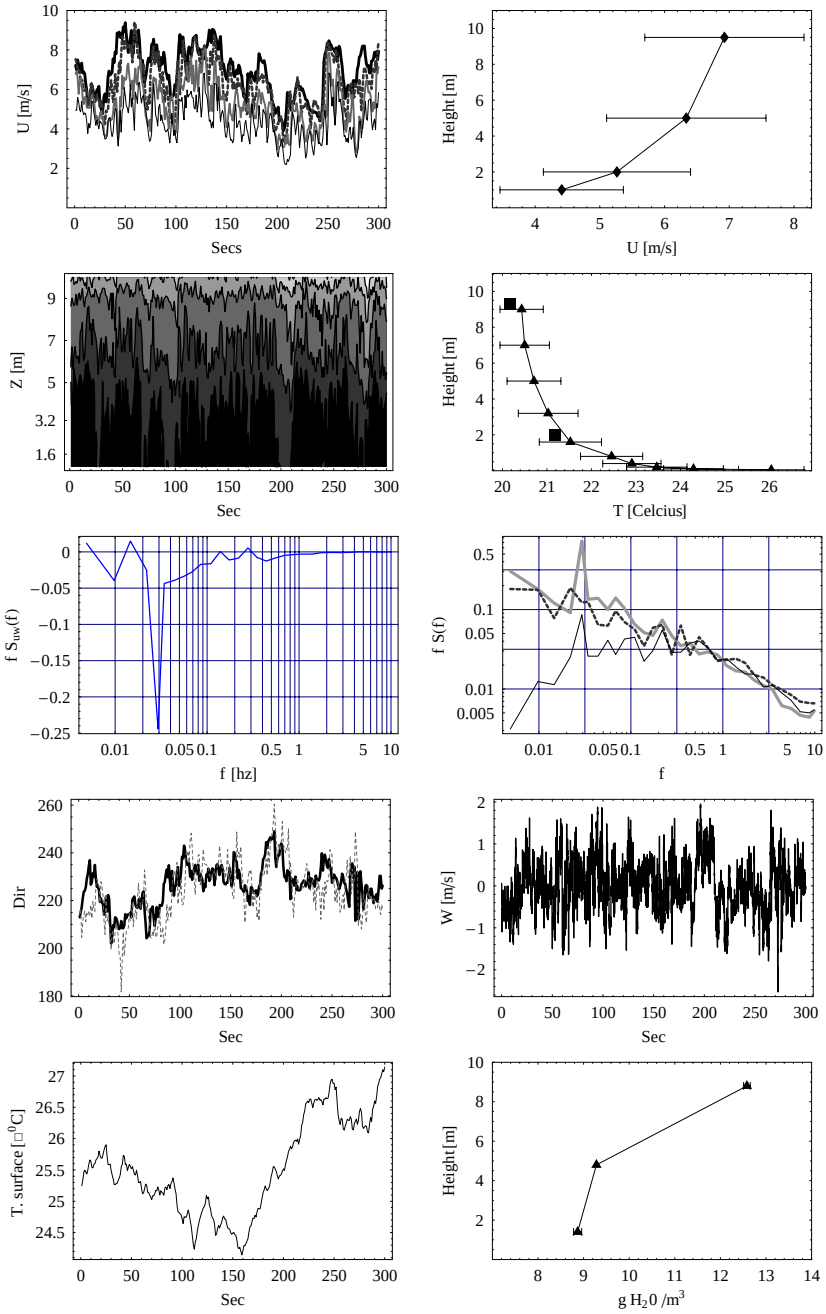

Figure 65. Overview of the meteorology during the release. In the first row is shown the wind-speed time series and the corresponding averaged wind profile. Second row shows time series of the temperature contours measured by the thermocouples and the corresponding temperature profile, the boxes shows the pt100 temperature. Third row shows the co-spectrum of $u'w'$ and the power spectra of u, v, w. The fourth row shows time series of the wind directions measured at 10 and 2m and the second figure shows a time series of the vertical fluctuations w'. The fifth row shows a time series of the surface temperature and the profile of absolute humidity.

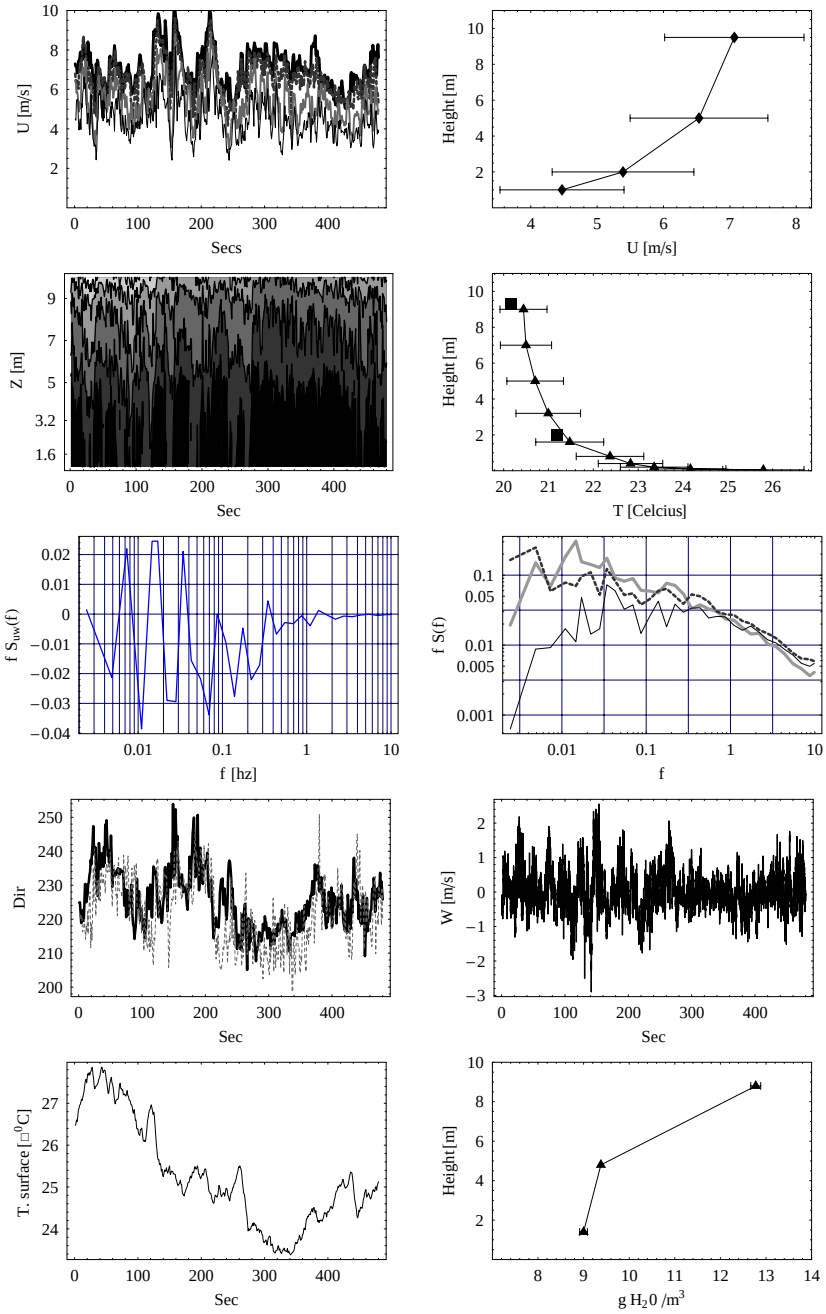

Figure 66. Overview of the meteorology during the release. In the first row is shown the wind-speed time series and the corresponding averaged wind profile. Second row shows time series of the temperature contours measured by the thermocouples and the corresponding temperature profile, the boxes shows the pt100 temperature. Third row shows the co-spectrum of $u'w'$ and the power spectra of u, v, w. The fourth row shows time series of the wind directions measured at 10 and 2m and the second figure shows a time series of the vertical fluctuations w'. The fifth row shows a time series of the surface temperature and the profile of absolute humidity.

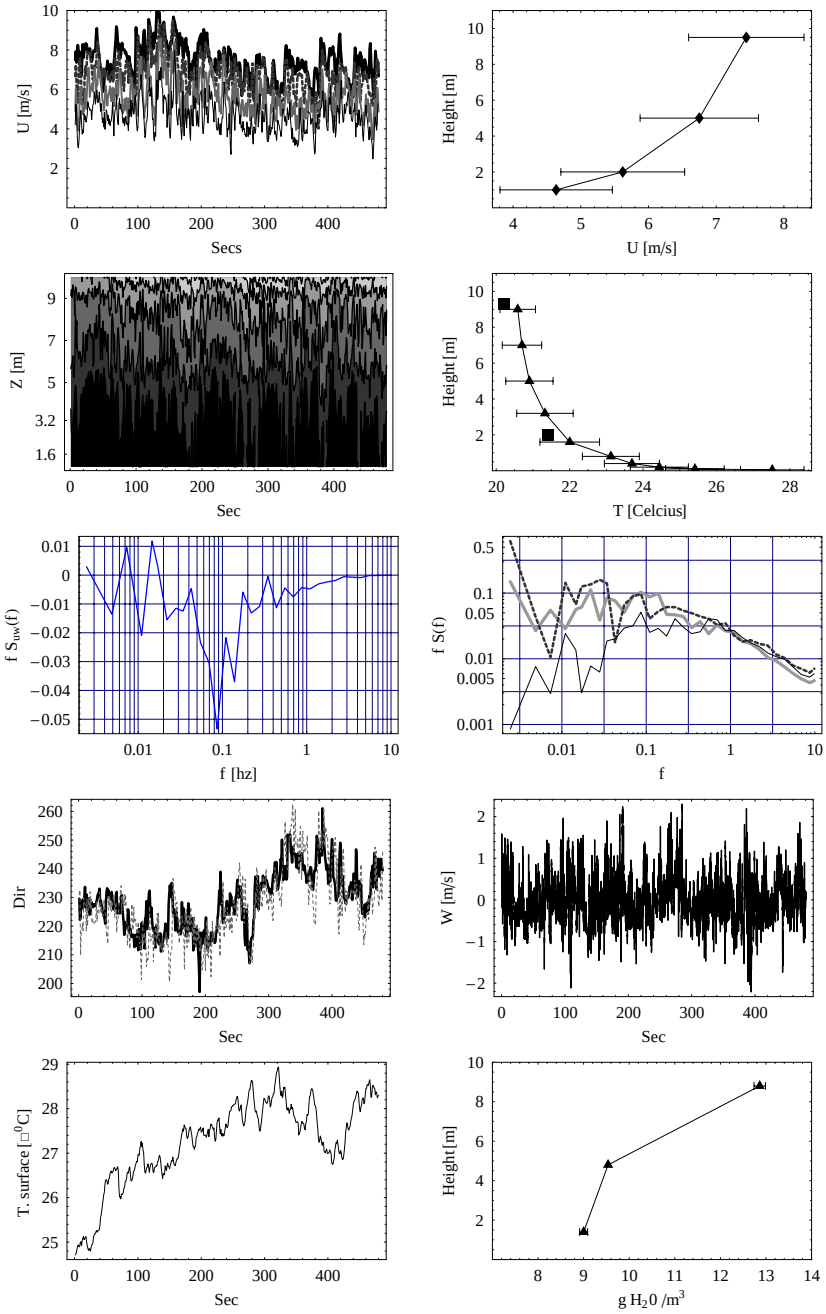

Figure 67. Overview of the meteorology during the release. In the first row is shown the wind-speed time series and the corresponding averaged wind profile. Second row shows time series of the temperature contours measured by the thermocouples and the corresponding temperature profile, the boxes shows the pt100 temperature. Third row shows the co-spectrum of $u'w'$ and the power spectra of u, v, w. The fourth row shows time series of the wind directions measured at 10 and 2m and the second figure shows a time series of the vertical fluctuations w'. The fifth row shows a time series of the surface temperature and the profile of absolute humidity.

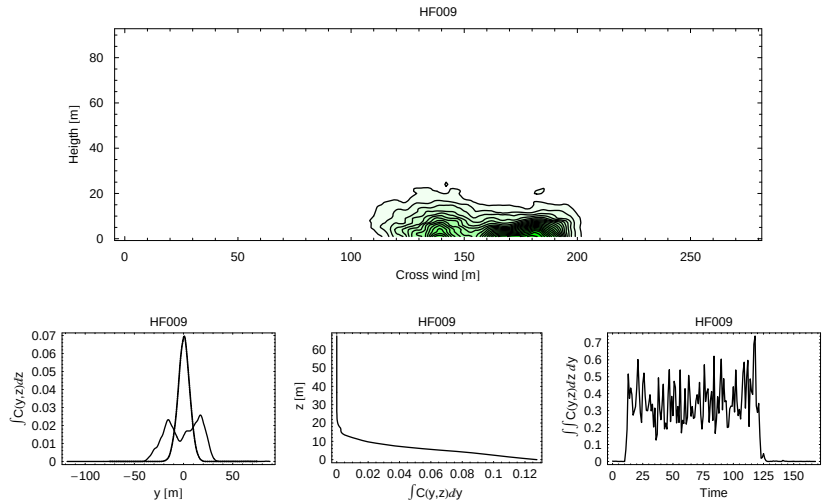

Figure 68. Overview of the measured HF plume profiles by the LIDAR. The top figure shows the contour lines of the mean profile. The bottom figures show : 1) The cross wind integrated profile in the vertical direction (thin line : fixed frame; thick line: moving frame). 2) The cross wind integrated profile in the horizontal direction.3) A timeserie of the cross wind integrated area of each LIDAR scan

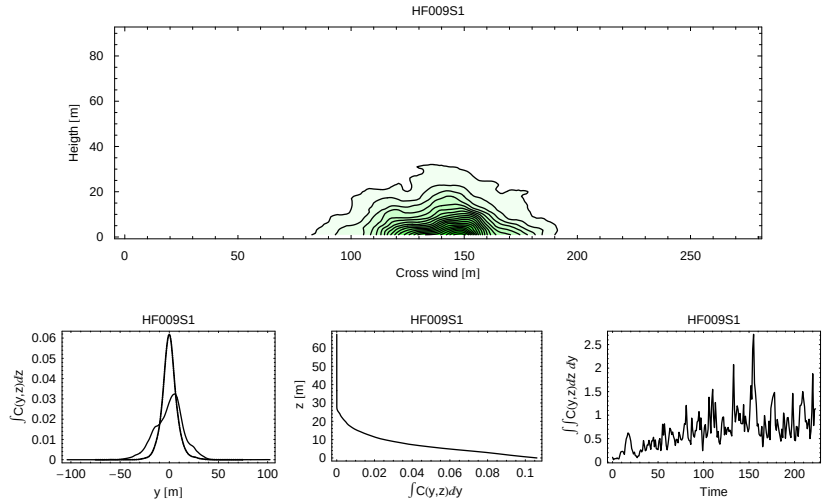

Figure 69. Overview of the measured smoke plume profiles by the LIDAR. The top figure shows the contour lines of the mean profile. The bottom figures show : 1) The cross wind integrated profile in the vertical direction (thin line : fixed frame; thick line: moving frame). 2) The cross wind integrated profile in the horizontal direction.3) A timeserie of the cross wind integrated area of each LIDAR scan

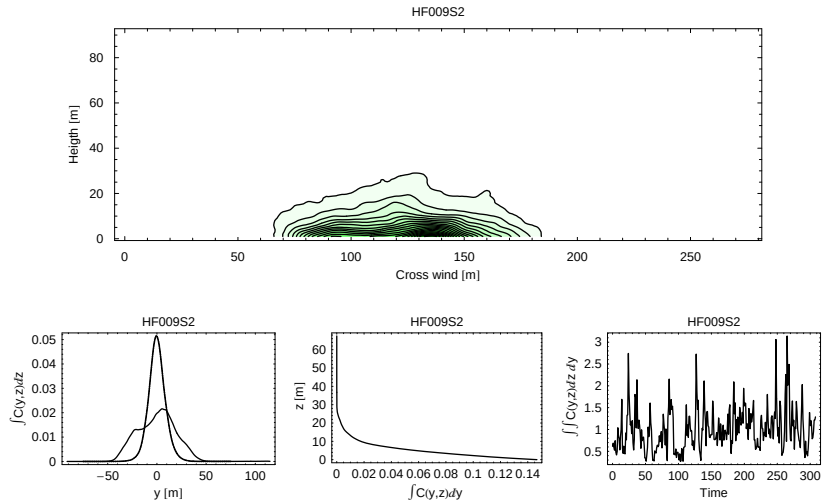

Figure 70. Overview of the measured smoke plume profiles by the LIDAR. The top figure shows the contour lines of the mean profile. The bottom figures show : 1) The cross wind integrated profile in the vertical direction (thin line : fixed frame; thick line: moving frame). 2) The cross wind integrated profile in the horizontal direction.3) A timeserie of the cross wind integrated area of each LIDAR scan

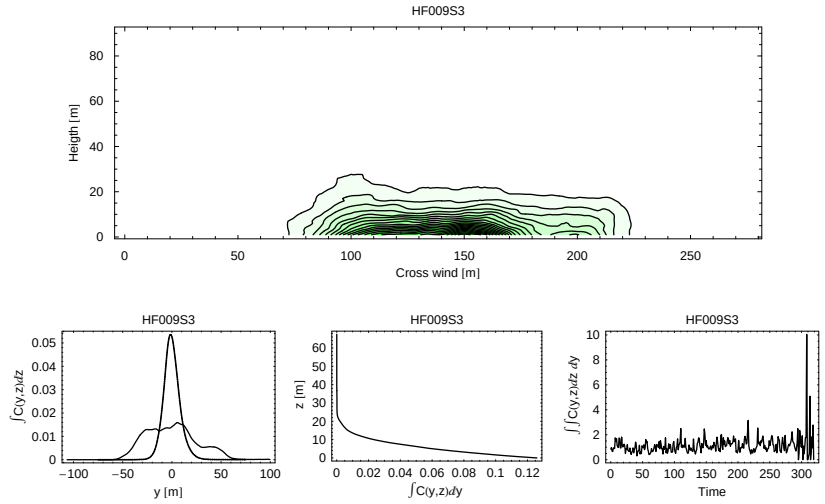

Figure 71. Overview of the measured smoke plume profiles by the LIDAR. The top figure shows the contour lines of the mean profile. The bottom figures show : 1) The cross wind integrated profile in the vertical direction (thin line : fixed frame; thick line: moving frame). 2) The cross wind integrated profile in the horizontal direction.3) A timeserie of the cross wind integrated area of each LIDAR scan

HF010

Comments: An early morning release trying to catch low wind speed and high humidity conditions, with some success. Already unstable and sunny. Cloudless sky during HF release, a few scattered clouds (1/8) during smoke release. Both plume fluctuating with large vertical mixing dominated by rising thermal jets. No lift-off.

Table 36. Timing

Release	Start	Stop	2D scans
HF010	08:08:25.88	08:11:49.32	133
HF010S1	08:14:42.17	08:24:55.69	399
HF010S2	08:25:26.17	08:33:41.22	322

Table 37. Plume parameters 100m downwind derived from lidar measurements

Parameter	Unit	HF010	HF010S1	HF010S2
$\overline{H}$	[m]	6.13	4.96	4.78
σ_z	[m]	3.50	3.33	3.19
σ_y	[m]	10.66	10.14	13.37
σ_{ym}	[m]	7.56	6.58	6.70

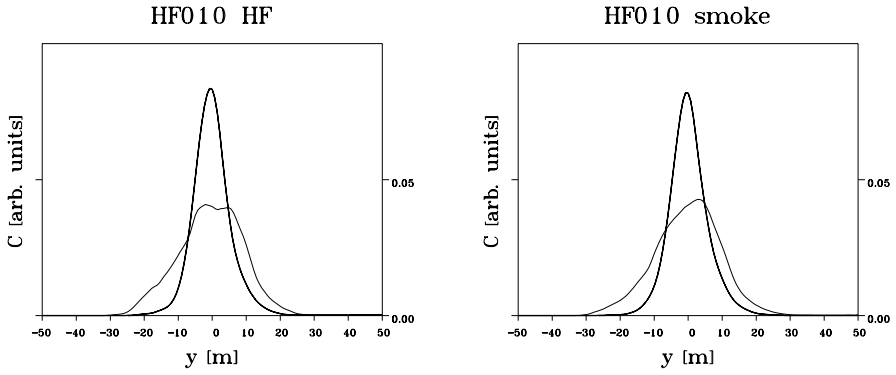

Figure 72. Depth integrated horizontal profiles from fixed frame analysis (thin line) and moving frame analysis (thick line).

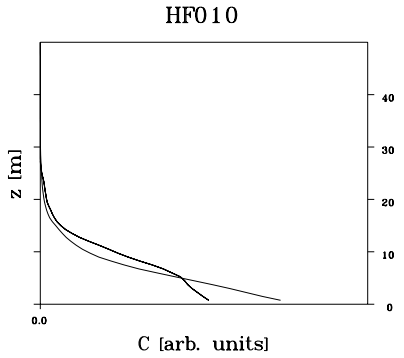

Figure 73. Cross-plume integrated vertical concentration profiles. Thin line: smoke, thick line: HF.

Parameter	Unit	HF010	HF010S1	HF010S2
Cup 10m	[m/s]	5.311	5.560	6.063
Cup 5m	[m/s]	4.716	4.889	5.263
Cup 2m	[m/s]	3.969	3.932	4.280
Cup 1m	[m/s]	3.309	3.210	3.565
Dir. 10m	deg.	245.800	248.355	246.447
Dir. 2m	deg.	244.805	246.232	244.357
Temp 10m	[^{o}C]	14.197	14.431	14.647
Temp 2m	[^{o}C]	14.469	14.770	15.090
RH 10m	[%]	82.227	81.152	79.551
RH 6m	[%]	82.977	81.863	80.156
RH 2m	[%]	82.874	81.550	79.508
Abs Hum 10m	[g H_2O/m^3]	10.036	10.048	9.980
Abs Hum 2m	[g H_2O/m^3]	10.285	10.309	10.248
TC 9m	[^{o}C]	14.393	14.640	14.812
TC 7m	[^{o}C]	14.325	14.583	14.772
TC 5m	[^{o}C]	14.565	14.837	15.044
TC 320cm	[^{o}C]	14.549	14.866	15.096
TC 160cm	[^{o}C]	14.545	14.906	15.161
TC 80cm	[^{o}C]	14.822	15.209	15.526
TC 40cm	[^{o}C]	15.049	15.473	15.806
TC 20cm	[^{o}C]	15.021	15.455	15.792
TC 10cm	[^{o}C]	15.301	15.775	16.170
TC 5cm	[^{o}C]	14.874	15.811	16.368
T surface	[^{o}C]	13.947	14.460	15.095
U	[m/s]	5.331	5.681	6.197
σ_u^2	[m^2/s^2]	1.042	1.026	1.118
σ_v^2	[m^2/s^2]	0.453	0.497	0.545
σ_w^2	[m^2/s^2]	0.243	0.227	0.193
σ_T^2	[K^2]	0.013	0.037	0.042
u_*	[m/s]	0.422	0.421	0.380
$\overline{w't'}$	[m/s K]	0.025	0.034	0.042
L	[m]	-219.361	-163.513	-97.083

Table 38. Key meteorological parameters measured during the experiments. The upper part represents the profile measurements and the lower part represents micrometeorological paramters measured by the sonic

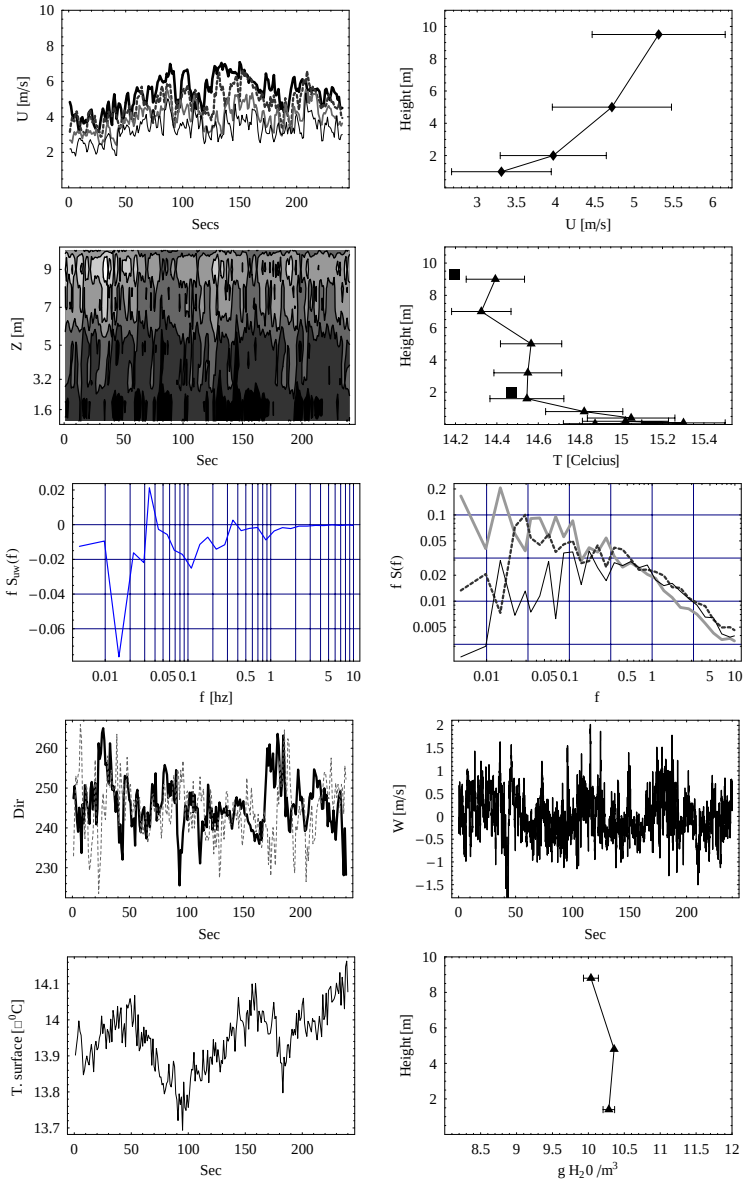

Figure 74. Overview of the meteorology during the release

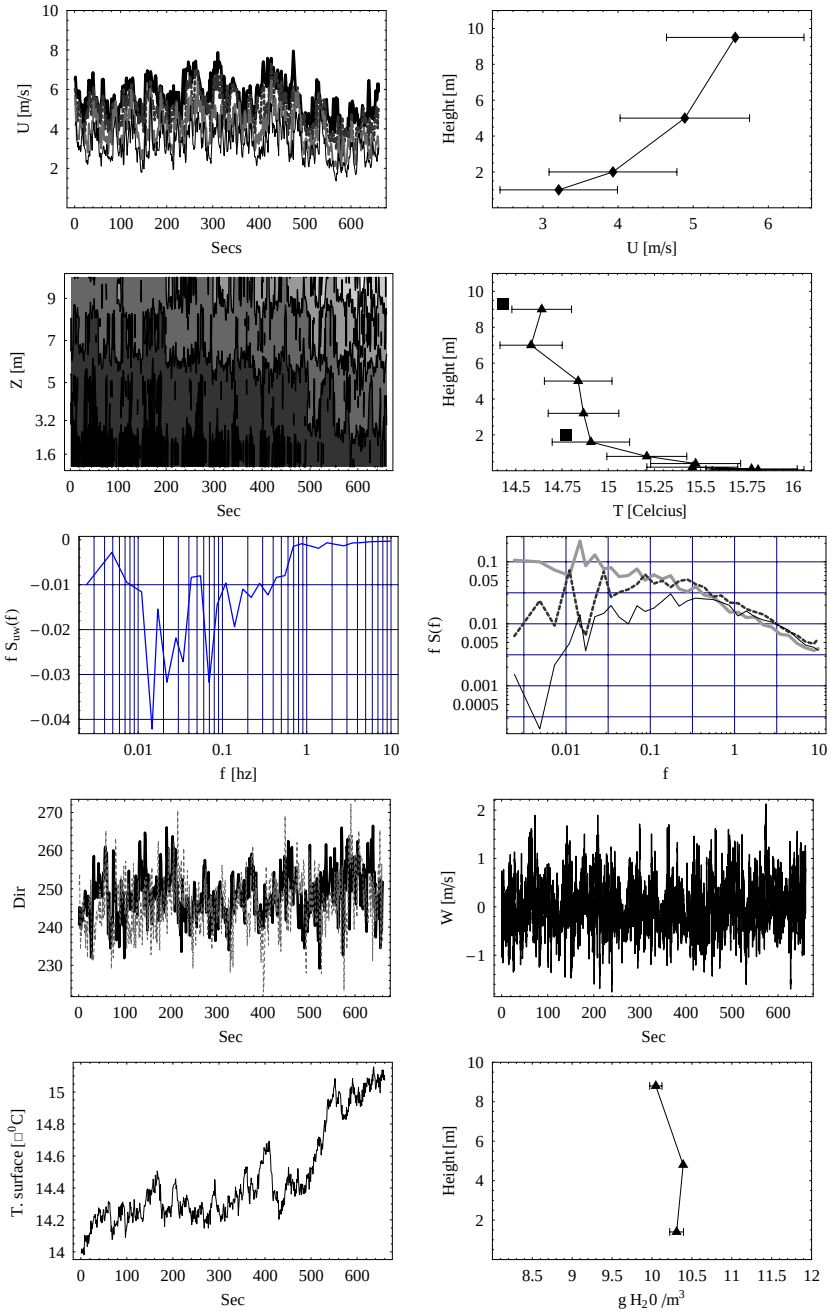

Figure 75. Overview of the meteorology during the release. In the first row is shown the wind-speed time series and the corresponding averaged wind profile. Second row shows time series of the temperature contours measured by the thermocouples and the corresponding temperature profile, the boxes shows the pt100 temperature. Third row shows the co-spectrum of $u'w'$ and the power spectra of u, v, w. The fourth row shows time series of the wind directions measured at 10 and 2m and the second figure shows a time series of the vertical fluctuations w'. The fifth row shows a time series of the surface temperature and the profile of absolute humidity.

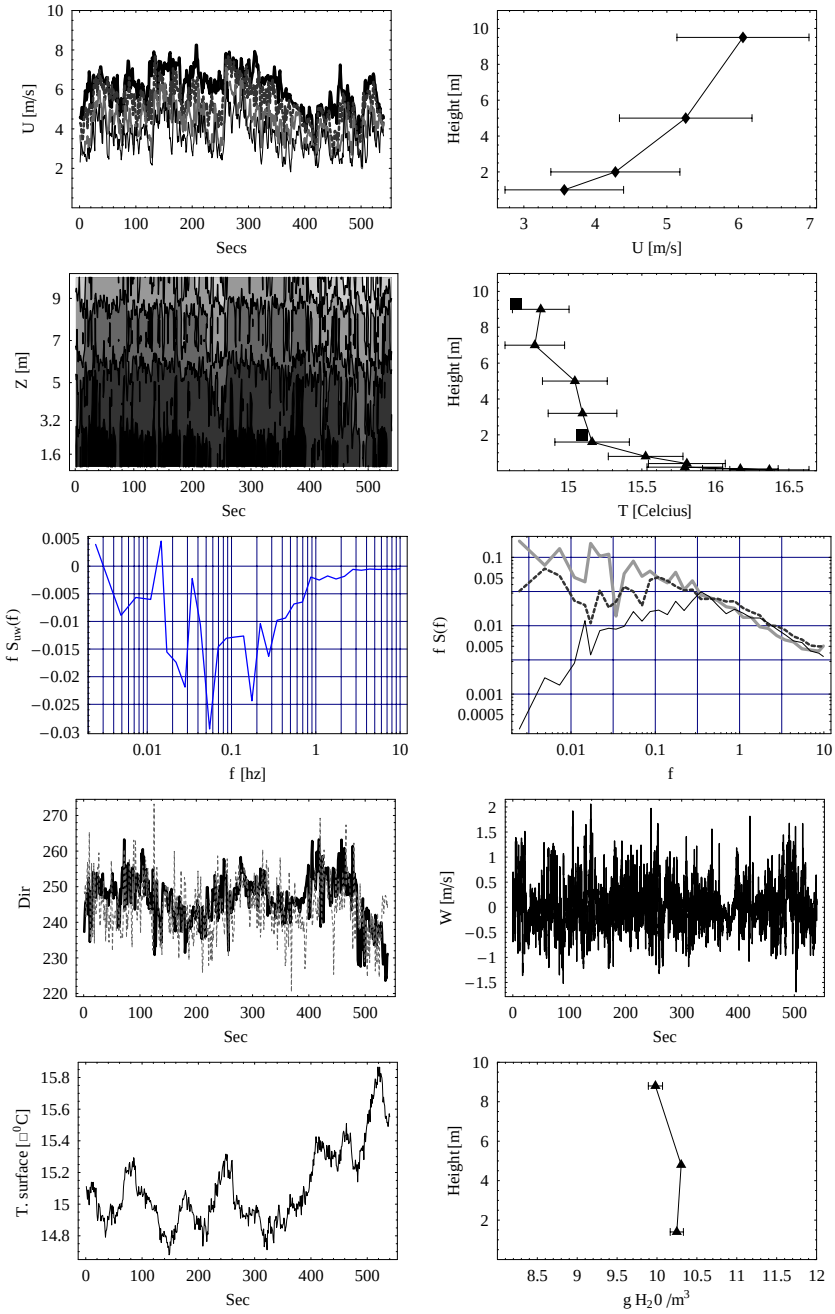

Figure 76. Overview of the meteorology during the release. In the first row is shown the wind-speed time series and the corresponding averaged wind profile. Second row shows time series of the temperature contours measured by the thermocouples and the corresponding temperature profile, the boxes shows the pt100 temperature. Third row shows the co-spectrum of $u'w'$ and the power spectra of u, v, w. The fourth row shows time series of the wind directions measured at 10 and 2m and the second figure shows a time series of the vertical fluctuations w'. The fifth row shows a time series of the surface temperature and the profile of absolute humidity.

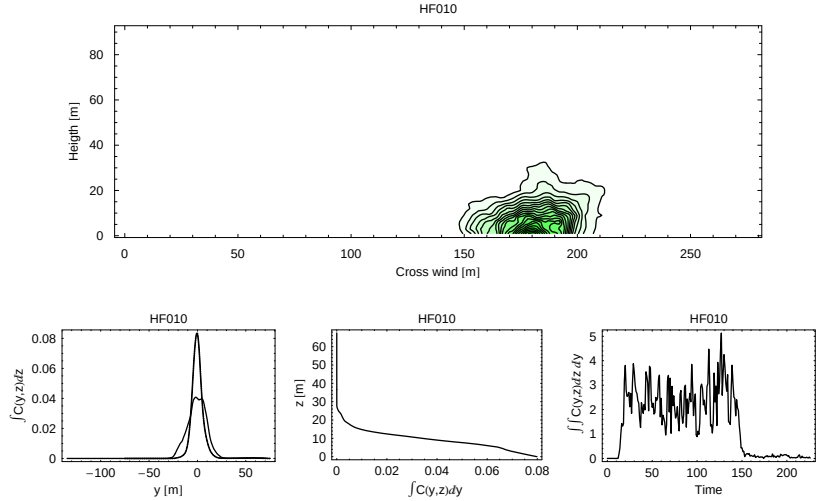

Figure 77. Overview of the measured HF plume profiles by the LIDAR. The top figure shows the contour lines of the mean profile. The bottom figures show : 1) The cross wind integrated profile in the vertical direction (thin line : fixed frame; thick line: moving frame). 2) The cross wind integrated profile in the horizontal direction.3) A timeserie of the cross wind integrated area of each LIDAR scan

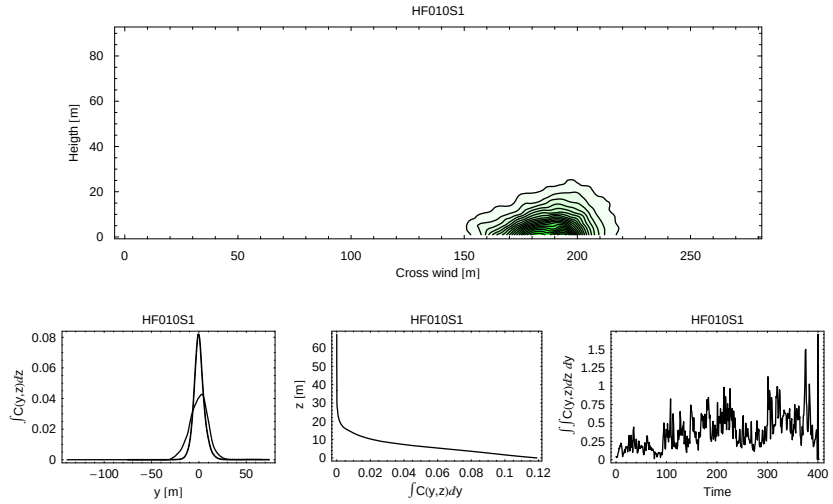

Figure 78. Overview of the measured smoke plume profiles by the LIDAR. The top figure shows the contour lines of the mean profile. The bottom figures show : 1) The cross wind integrated profile in the vertical direction (thin line : fixed frame; thick line: moving frame). 2) The cross wind integrated profile in the horizontal direction.3) A timeserie of the cross wind integrated area of each LIDAR scan

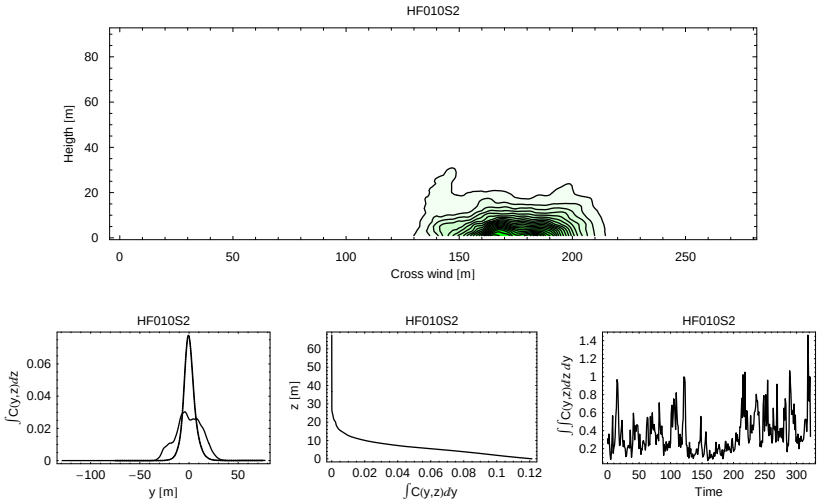

Figure 79. Overview of the measured smoke plume profiles by the LIDAR. The top figure shows the contour lines of the mean profile. The bottom figures show : 1) The cross wind integrated profile in the vertical direction (thin line : fixed frame; thick line: moving frame). 2) The cross wind integrated profile in the horizontal direction.3) A timeserie of the cross wind integrated area of each LIDAR scan

HF011

Comments: 2/8 cloud cover, sunshine and unstable. Butane added to the HF. Filters had not been collected from the last experiment, hence no filter data. The HF looks passive with upwards thermal jets. A spill on the ground from the smoke machine generates light smoke visible about 100m downwind. Later on the smoke machine strikes (clogged nozzle).

Table 39. Timing

Release	Start	Stop	2D scans
HF011	09:24:24.53	09:27:43.30	136

Table 40. Plume parameters 100m downwind derived from lidar measurements

Parameter	Unit	HF011
$\overline{H}$	[m]	5.96
σ_z	[m]	4.02
σ_y	[m]	13.03
σ_{ym}	[m]	7.41

Parameter	Unit	HF011
Cup 10m	[m/s]	6.580
Cup 5m	[m/s]	5.754
Cup 2m	[m/s]	4.605
Cup 1m	[m/s]	3.835
Dir. 10m	deg.	261.185
Dir. 2m	deg.	258.686
Temp 10m	[^{o}C]	16.095
Temp 2m	[^{o}C]	16.702
RH 10m	[%]	69.576
RH 6m	[%]	70.913
RH 2m	[%]	68.783
Abs Hum 10m	[g H_2O/m^3]	9.531
Abs Hum 2m	[g H_2O/m^3]	9.773
TC 9m	[^{o}C]	16.232
TC 7m	[^{o}C]	16.267
TC 5m	[^{o}C]	16.471
TC 320cm	[^{o}C]	16.591
TC 160cm	[^{o}C]	16.830
TC 80cm	[^{o}C]	17.308
TC 40cm	[^{o}C]	17.575
TC 20cm	[^{o}C]	17.679
TC 10cm	[^{o}C]	18.125
TC 5cm	[^{o}C]	18.774
T surface	[^{o}C]	17.646
U	[m/s]	6.662
σ_u^2	[m^2/s^2]	0.979
σ_v^2	[m^2/s^2]	1.524
σ_w^2	[m^2/s^2]	0.270
σ_T^2	[K^2]	0.064
u_*	[m/s]	0.487
$\overline{w't'}$	[m/s K]	0.055
L	[m]	-155.455

Table 41. Key meteorological parameters measured during the experiments. The upper part represents the profile measurements and the lower part represents micrometeorological paramters measured by the sonic

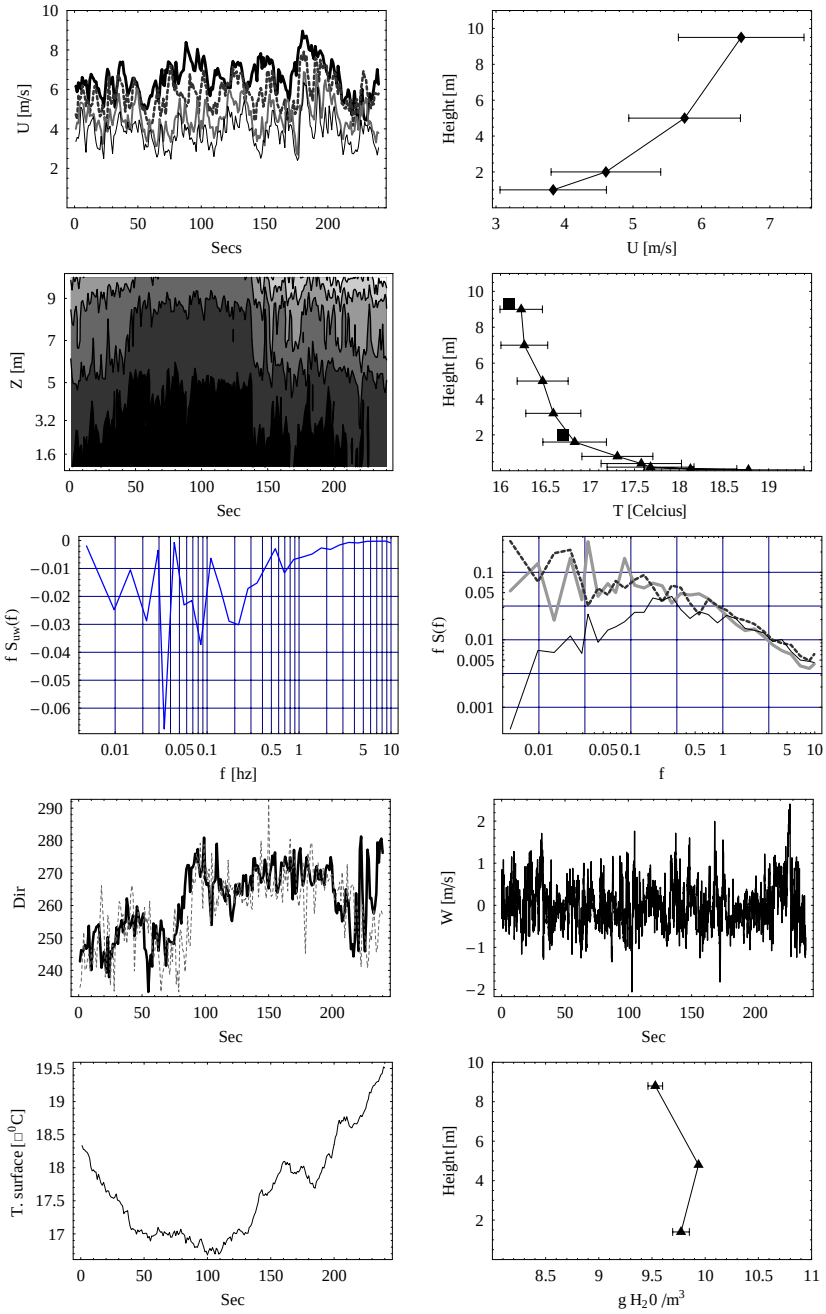

Figure 80. Overview of the meteorology during the release. In the first row is shown the wind-speed time series and the corresponding averaged wind profile. Second row shows time series of the temperature contours measured by the thermocouples and the corresponding temperature profile, the boxes shows the pt100 temperature. Third row shows the co-spectrum of $u'w'$ and the power spectra of u, v, w. The fourth row shows time series of the wind directions measured at 10 and 2m and the second figure shows a time series of the vertical fluctuations w'. The fifth row shows a time series of the surface temperature and the profile of absolute humidity.

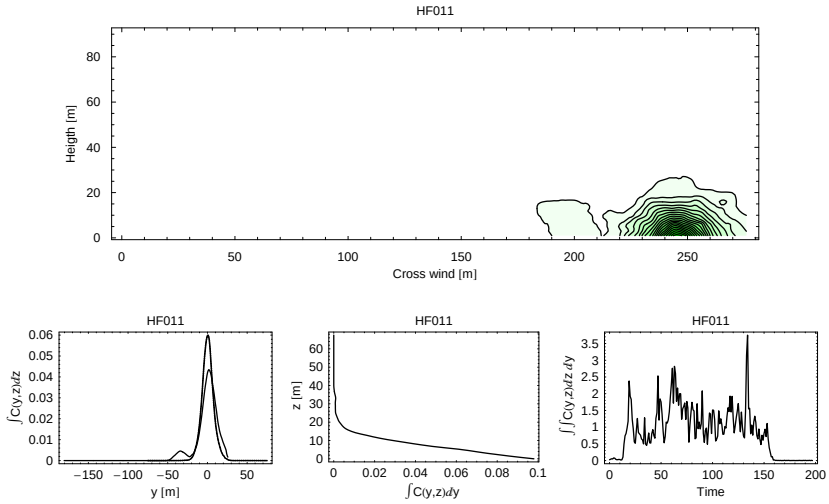

Figure 81. Overview of the measured HF plume profiles by the LIDAR. The top figure shows the contour lines of the mean profile. The bottom figures show : 1) The cross wind integrated profile in the vertical direction (thin line : fixed frame; thick line: moving frame). 2) The cross wind integrated profile in the horizontal direction.3) A timeserie of the cross wind integrated area of each LIDAR scan

HF012

Comments: Calm, damp morning with little wind, cloudless sky and a 5-10m thick layer of fog on the ground. Here and there frost in the grass. At release start the fog has gone and the temperature profile turned. Almost no wind and already very unstable conditions. A small smoke puff is released in order to see how it behaves. The smoke puff goes horizontally, then rises vertically up to a level of perhaps 20 meters! HF and smoke show the same behaviour typical for very unstable conditions. Both flap up and down, sometimes clearly lifted off the ground, sometimes on the ground. The HF cloud is disappearing slowly over the edge of the Bowl while the smoke is started. At this point the HF cloud is on the ground.

Table 42. Timing

Release	Start	Stop	2D scans
HF012	07:49:19.20	07:52:21.33	102
HF012S1	07:59:07.50	08:10:57.31	395
HF012S2	08:27:46.12	08:31:48.45	178
HF012S3	08:32:17.67	08:34:19.83	90
HF012S4	08:35:04.21	08:39:31.42	196

Table 43. Plume parameters 100m downwind derived from lidar measurements

Parameter	Unit	HF012	HF012S1	HF012S2	HF012S3	HF012S4
$\overline{H}$	[m]	19.29	16.59	11.40	8.06	9.23
σ_z	[m]	7.46	7.06	6.77	5.25	6.03
σ_y	[m]	11.23	19.28	17.71	13.93	22.66
σ_{ym}	[m]	8.42	13.23	8.00	7.98	10.24

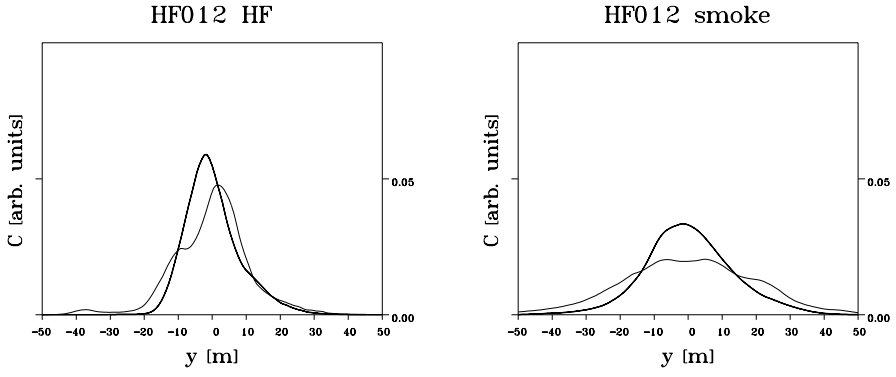

Figure 82. Depth integrated horizontal profiles from fixed frame analysis (thin line) and moving frame analysis (thick line).

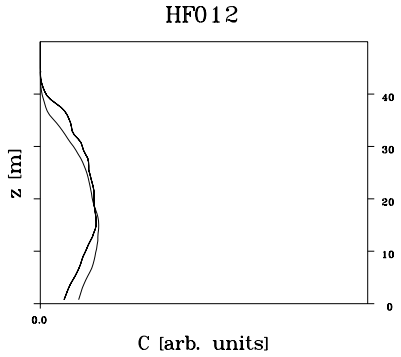

Figure 83. Cross-plume integrated vertical concentration profiles. Thin line: smoke, thick line: HF.

Parameter	Unit	HF012	HF012S1	HF012S2	HF012S3	HF012S4
Cup 10m	[m/s]	1.593	0.905	2.658	2.674	2.582
Cup 5m	[m/s]	1.491	0.938	2.596	2.487	2.422
Cup 2m	[m/s]	1.285	0.788	2.246	2.101	2.049
Cup 1m	[m/s]	1.132	0.657	1.868	1.825	1.765
Dir. 10m	deg.	248.226	241.131	235.602	235.094	249.865
Dir. 2m	deg.	244.138	231.391	231.690	234.974	249.900
Temp 10m	[^{o}C]	11.699	12.105	13.607	13.594	13.778
Temp 2m	[^{o}C]	11.841	12.341	14.057	14.098	14.220
RH 10m	[%]	90.909	91.626	84.015	82.767	82.617
RH 6m	[%]	88.242	88.404	82.374	81.685	81.581
RH 2m	[%]	92.117	91.795	84.437	83.302	82.472
Abs Hum 10m	[g H_2O/m^3]	9.505	9.827	9.889	9.734	9.828
Abs Hum 2m	[g H_2O/m^3]	9.717	9.990	10.217	10.106	10.080
TC 9m	[^{o}C]	11.917	12.666	13.949	14.009	14.217
TC 7m	[^{o}C]	11.644	12.320	13.613	13.697	13.919
TC 5m	[^{o}C]	11.951	12.648	13.939	14.041	14.236
TC 320cm	[^{o}C]	11.870	12.575	13.937	14.079	14.314
TC 160cm	[^{o}C]	11.817	12.497	14.006	14.113	14.291
TC 80cm	[^{o}C]	12.207	12.900	14.480	14.626	14.768
TC 40cm	[^{o}C]	12.527	13.303	14.930	15.120	15.135
TC 20cm	[^{o}C]	12.616	13.363	15.014	15.168	15.170
TC 10cm	[^{o}C]	12.956	13.821	15.624	15.765	15.660
TC 5cm	[^{o}C]	13.524	14.562	16.238	16.407	16.145
T surface	[^{o}C]	11.340	12.465	14.429	14.375	14.755
U	[m/s]	1.511	0.914	2.677	2.671	2.592
σ_u^2	[m^2/s^2]	0.106	0.165	0.215	0.261	0.150
σ_v^2	[m^2/s^2]	0.082	0.074	0.237	0.226	0.147
σ_w^2	[m^2/s^2]	0.040	0.053	0.087	0.098	0.086
σ_T^2	[K^2]	0.018	0.187	0.053	0.079	0.084
u_*	[m/s]	0.144	0.115	0.226	0.292	0.213
$\overline{w't'}$	[m/s K]	0.012	0.029	0.039	0.061	0.045
L	[m]	-18.892	-3.849	-22.126	-30.059	-15.787

Table 44. Key meteorological parameters measured during the experiments. The upper part represents the profile measurements and the lower part represents micrometeorological paramters measured by the sonic

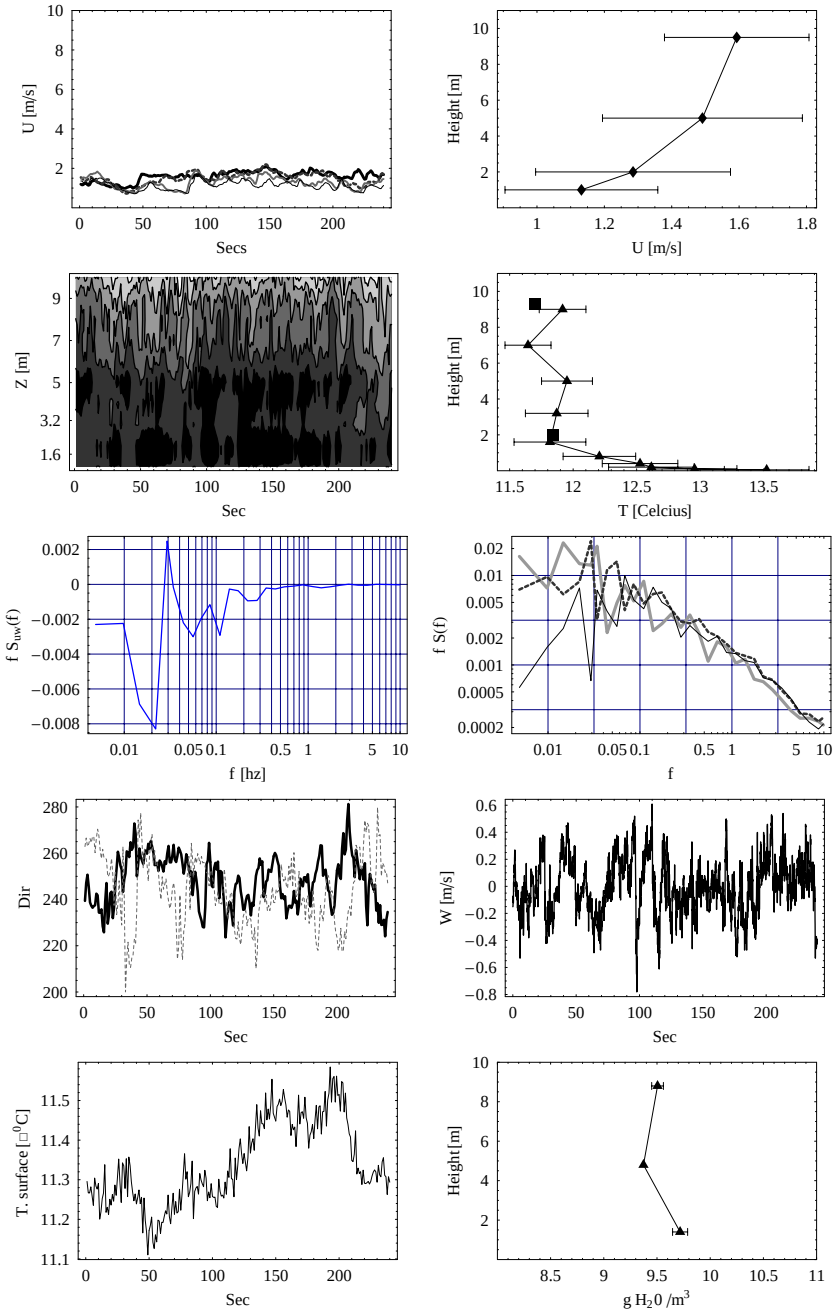

Figure 84. Overview of the meteorology during the release. In the first row is shown the wind-speed time series and the corresponding averaged wind profile. Second row shows time series of the temperature contours measured by the thermocouples and the corresponding temperature profile, the boxes shows the pt100 temperature. Third row shows the co-spectrum of $u'w'$ and the power spectra of u, v, w. The fourth row shows time series of the wind directions measured at 10 and 2m and the second figure shows a time series of the vertical fluctuations w'. The fifth row shows a time series of the surface temperature and the profile of absolute humidity.

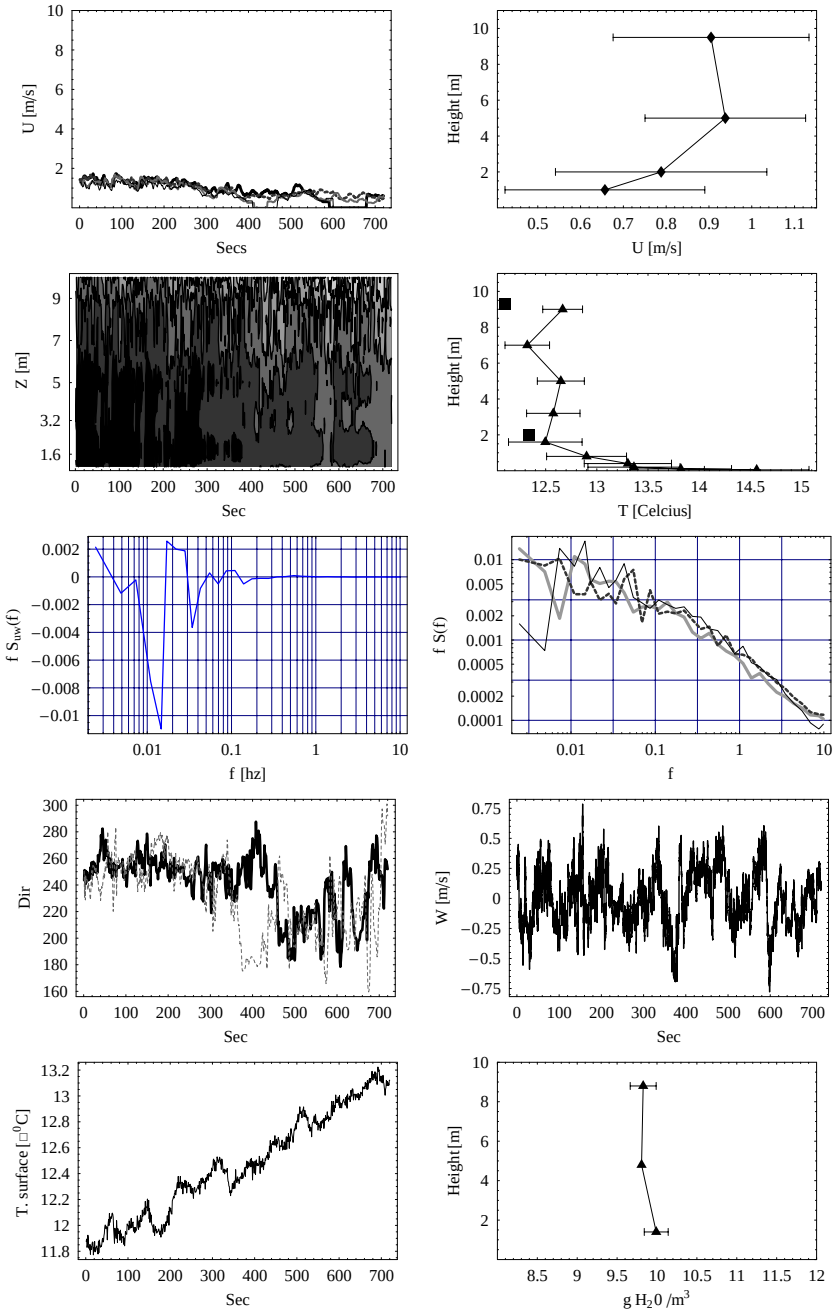

Figure 85. Overview of the meteorology during the release. In the first row is shown the wind-speed time series and the corresponding averaged wind profile. Second row shows time series of the temperature contours measured by the thermocouples and the corresponding temperature profile, the boxes shows the pt100 temperature. Third row shows the co-spectrum of $u'w'$ and the power spectra of u, v, w. The fourth row shows time series of the wind directions measured at 10 and 2m and the second figure shows a time series of the vertical fluctuations w'. The fifth row shows a time series of the surface temperature and the profile of absolute humidity.

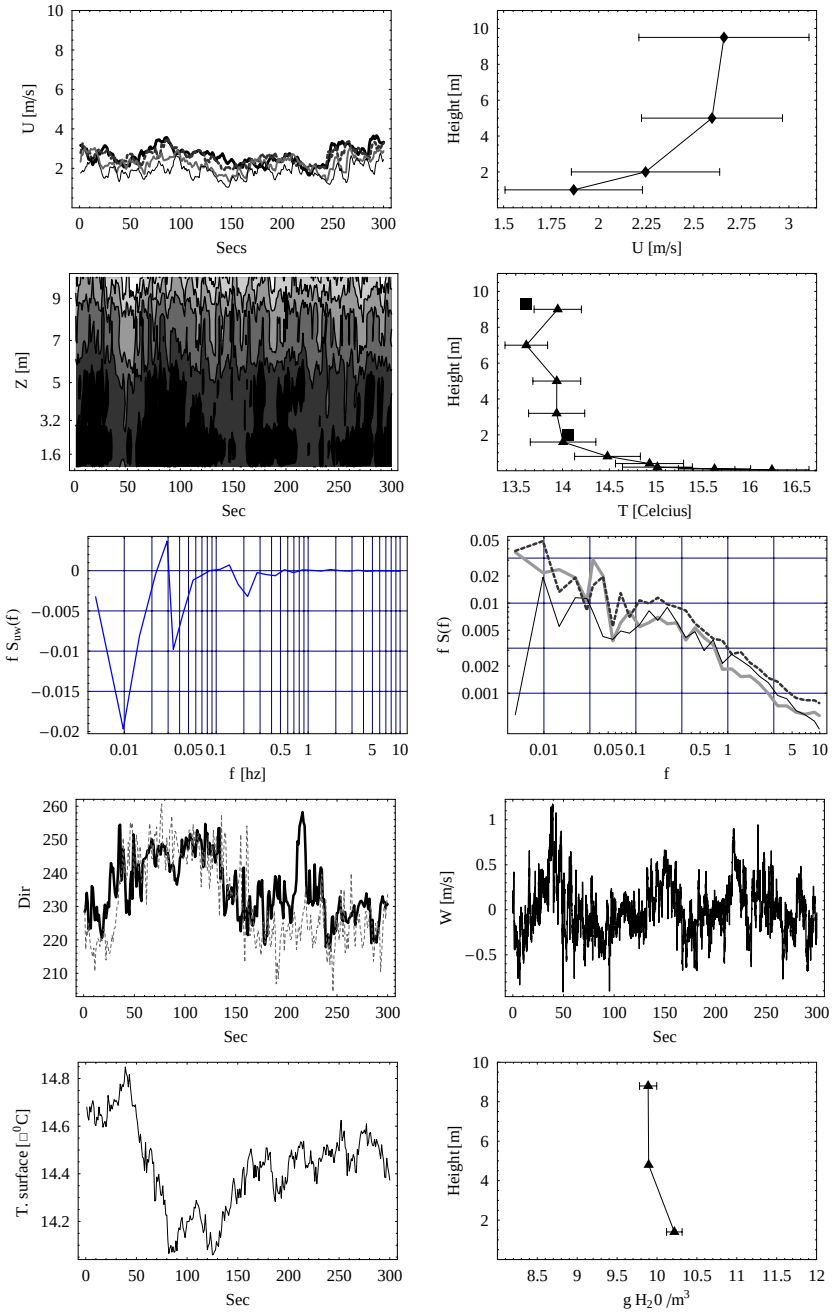

Figure 86. Overview of the meteorology during the release. In the first row is shown the wind-speed time series and the corresponding averaged wind profile. Second row shows time series of the temperature contours measured by the thermocouples and the corresponding temperature profile, the boxes shows the pt100 temperature. Third row shows the co-spectrum of $u'w'$ and the power spectra of u, v, w. The fourth row shows time series of the wind directions measured at 10 and 2m and the second figure shows a time series of the vertical fluctuations w'. The fifth row shows a time series of the surface temperature and the profile of absolute humidity.

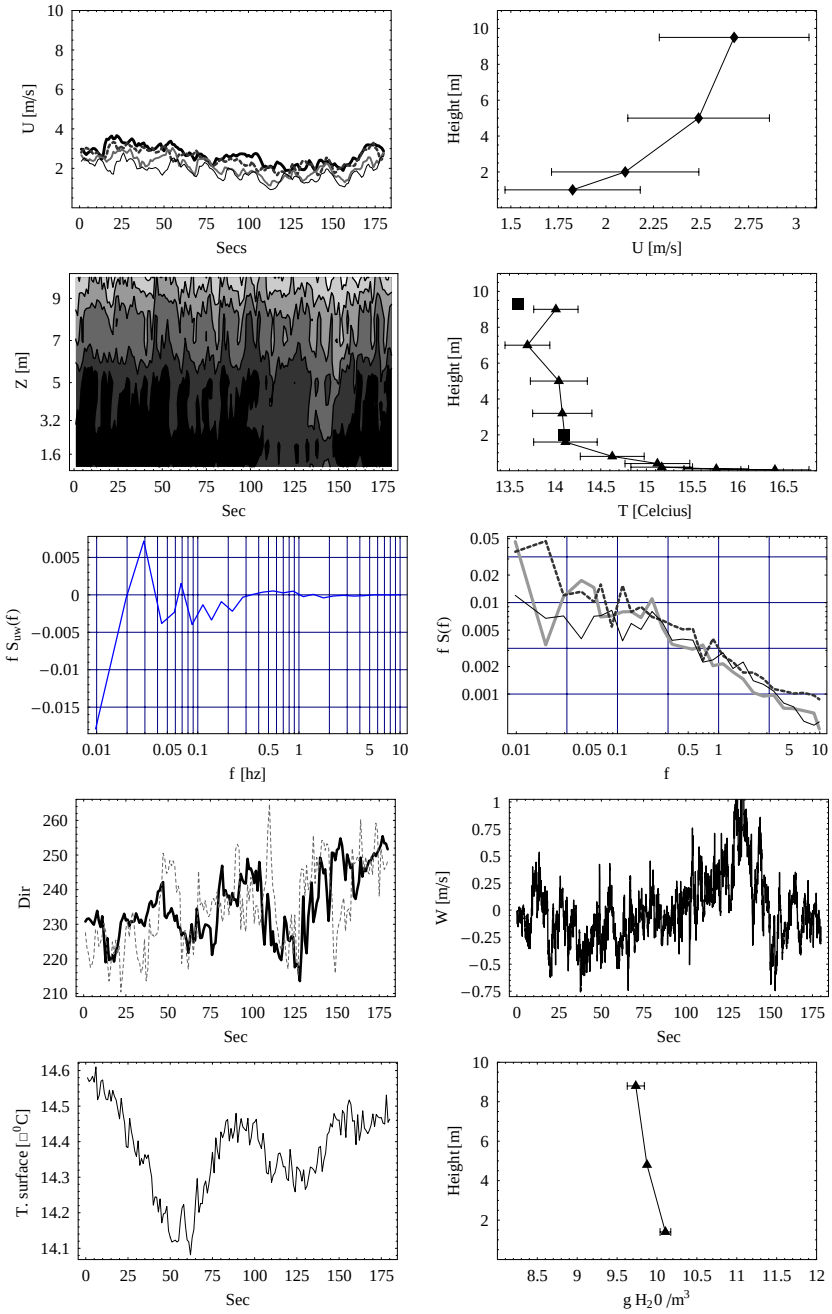

Figure 87. Overview of the meteorology during the release. In the first row is shown the wind-speed time series and the corresponding averaged wind profile. Second row shows time series of the temperature contours measured by the thermocouples and the corresponding temperature profile, the boxes shows the pt100 temperature. Third row shows the co-spectrum of $u'w'$ and the power spectra of u, v, w. The fourth row shows time series of the wind directions measured at 10 and 2m and the second figure shows a time series of the vertical fluctuations w'. The fifth row shows a time series of the surface temperature and the profile of absolute humidity.

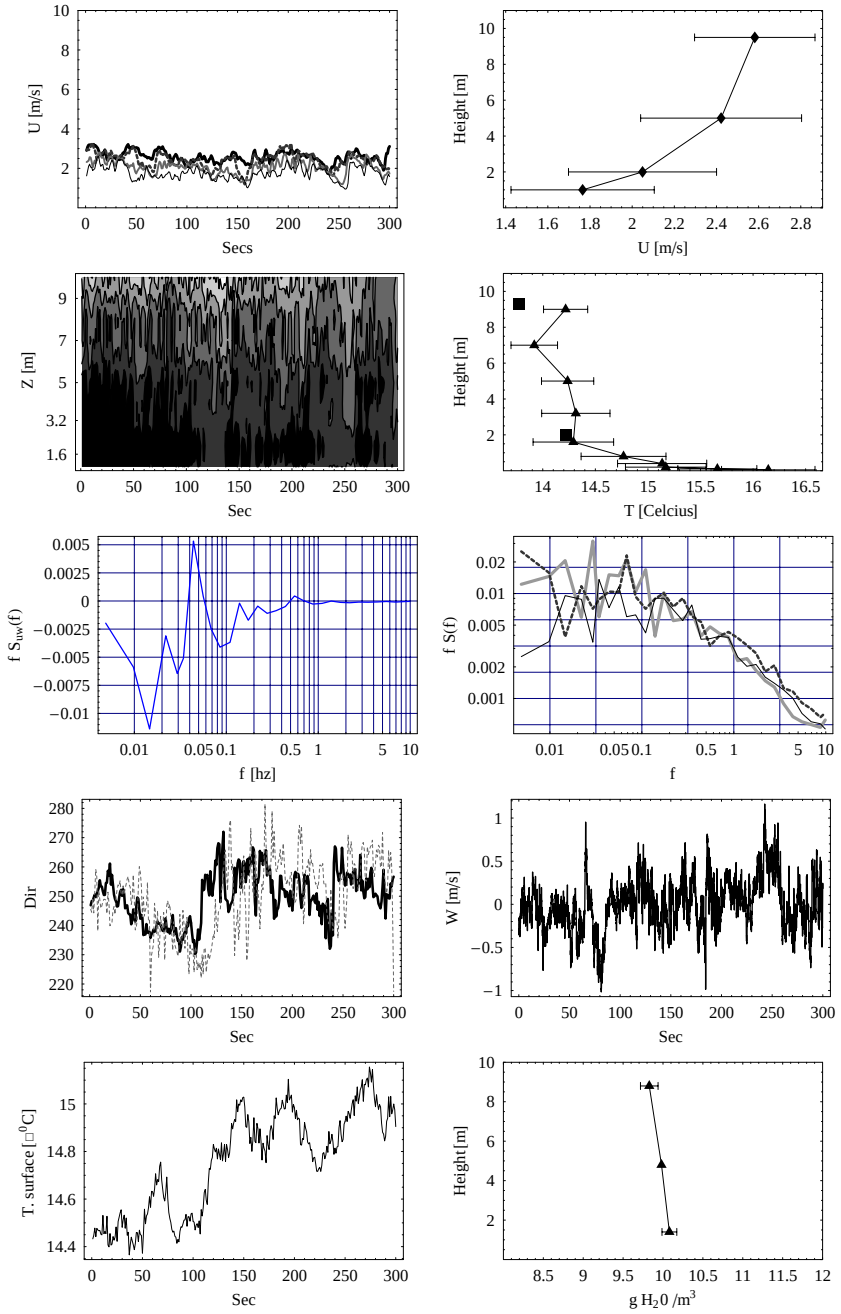

Figure 88. Overview of the meteorology during the release. In the first row is shown the wind-speed time series and the corresponding averaged wind profile. Second row shows time series of the temperature contours measured by the thermocouples and the corresponding temperature profile, the boxes shows the pt100 temperature. Third row shows the co-spectrum of $u'w'$ and the power spectra of u, v, w. The fourth row shows time series of the wind directions measured at 10 and 2m and the second figure shows a time series of the vertical fluctuations w'. The fifth row shows a time series of the surface temperature and the profile of absolute humidity.

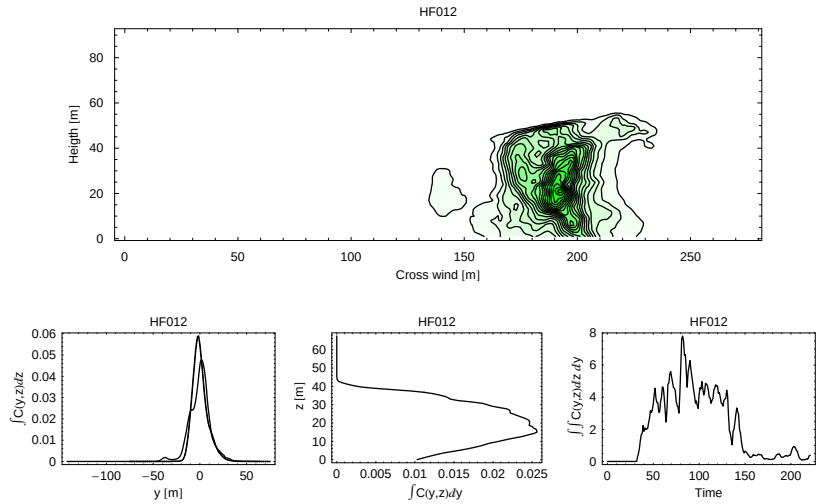

Figure 89. Overview of the measured HF plume profiles by the LIDAR. The top figure shows the contour lines of the mean profile. The bottom figures show : 1) The cross wind integrated profile in the vertical direction (thin line : fixed frame; thick line: moving frame). 2) The cross wind integrated profile in the horizontal direction.3) A timeserie of the cross wind integrated area of each LIDAR scan

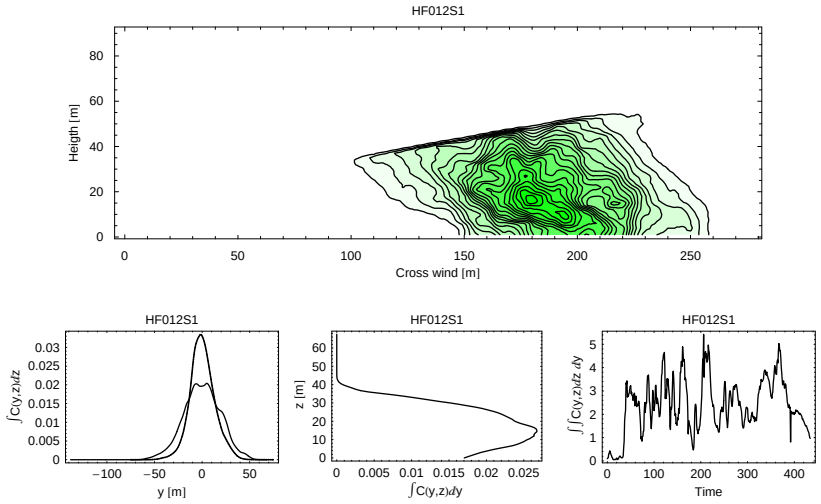

Figure 90. Overview of the measured smoke plume profiles by the LIDAR. The top figure shows the contour lines of the mean profile. The bottom figures show : 1) The cross wind integrated profile in the vertical direction (thin line : fixed frame; thick line: moving frame). 2) The cross wind integrated profile in the horizontal direction.3) A timeserie of the cross wind integrated area of each LIDAR scan

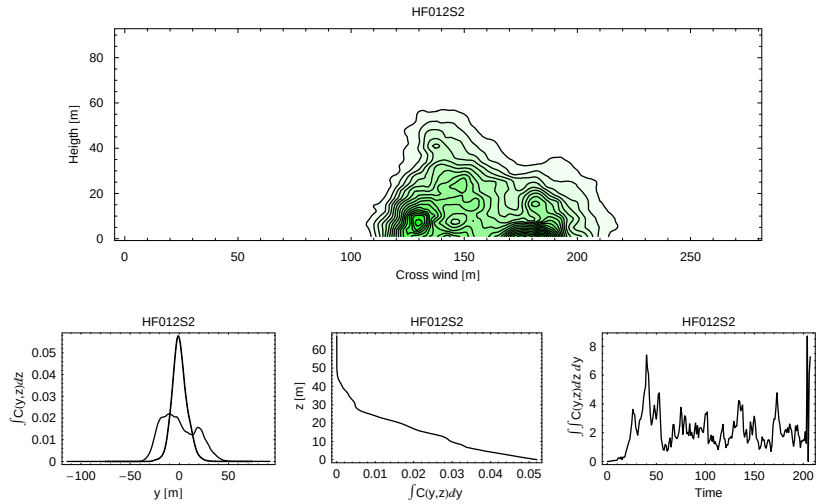

Figure 91. Overview of the measured smoke plume profiles by the LIDAR. The top figure shows the contour lines of the mean profile. The bottom figures show : 1) The cross wind integrated profile in the vertical direction (thin line : fixed frame; thick line: moving frame). 2) The cross wind integrated profile in the horizontal direction.3) A timeserie of the cross wind integrated area of each LIDAR scan

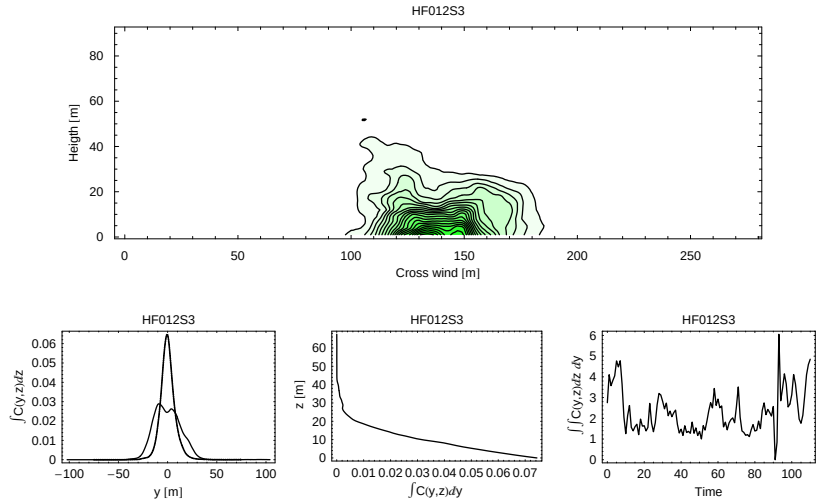

Figure 92. Overview of the measured smoke plume profiles by the LIDAR. The top figure shows the contour lines of the mean profile. The bottom figures show : 1) The cross wind integrated profile in the vertical direction (thin line : fixed frame; thick line: moving frame). 2) The cross wind integrated profile in the horizontal direction.3) A timeserie of the cross wind integrated area of each LIDAR scan

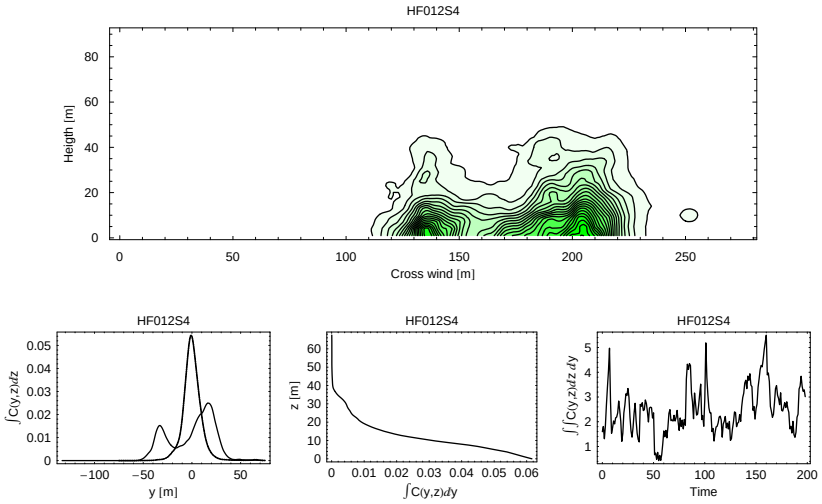

Figure 93. Overview of the measured smoke plume profiles by the LIDAR. The top figure shows the contour lines of the mean profile. The bottom figures show : 1) The cross wind integrated profile in the vertical direction (thin line : fixed frame; thick line: moving frame). 2) The cross wind integrated profile in the horizontal direction.3) A timeserie of the cross wind integrated area of each LIDAR scan

B.2 overview of the meteorological conditions for the campaign

Below a summary of meteorological conditions during the Campaign is given in graphical form. Six plots are shown for each day all based on five minute averages. The quantities shown were all measured at a height of approximately 10m. The friction velocity u_* and the (inverse) Monin-Obukhov length scale were derived from sonic anemometer measurements. We recall that the friction velocity is a measure of the vertical flux of horizontal momentum, i.e. ${u_*}^2 \equiv -\langle u'w' \rangle$, where u' and w' are the fluctuating parts of the horizontal and vertical velocity components, respectively. The Monin-Obukhov length scale is defined as $L = -\frac{{u_*}^3 < T >}{\kappa g < T'w' >}$, where T is the absolute temperature and g is the acceleration of gravity. z/L is a stability measure for the height z above the ground. $1/L$ is positive for stable conditions, negative for unstable conditions and zero for neutral conditions. z/L is a stability measure. It measures the ratio between energy dissipation and energy production associated with the sensible heat flux. In a constant flux layer both L and u_* are independent of z. The arrows on the plots mark times where HF releases were made.

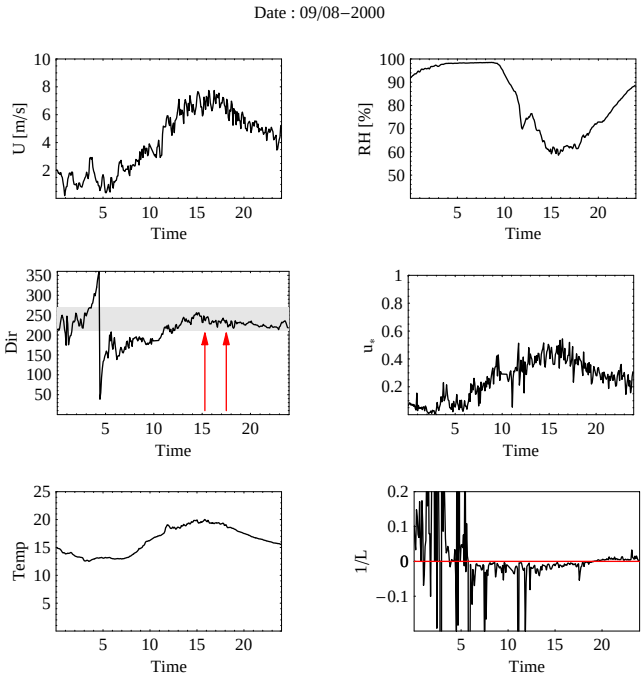

Figure 94. Whole day overview

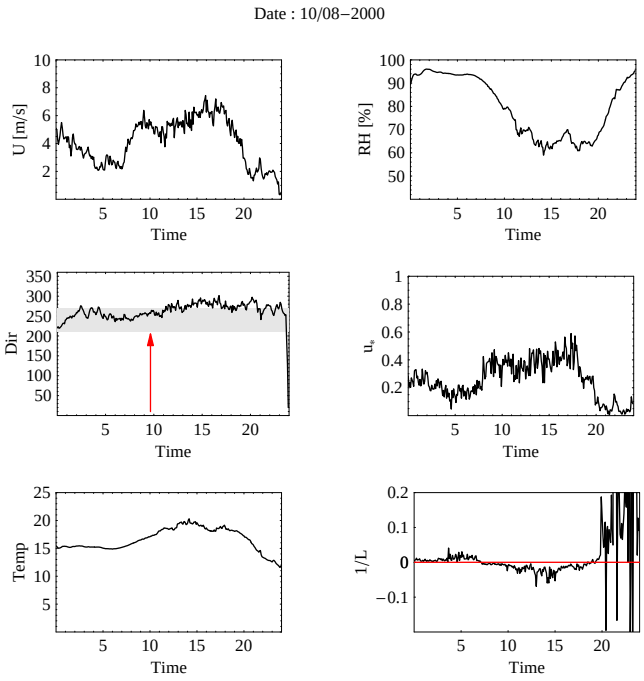

Figure 95. Whole day overview

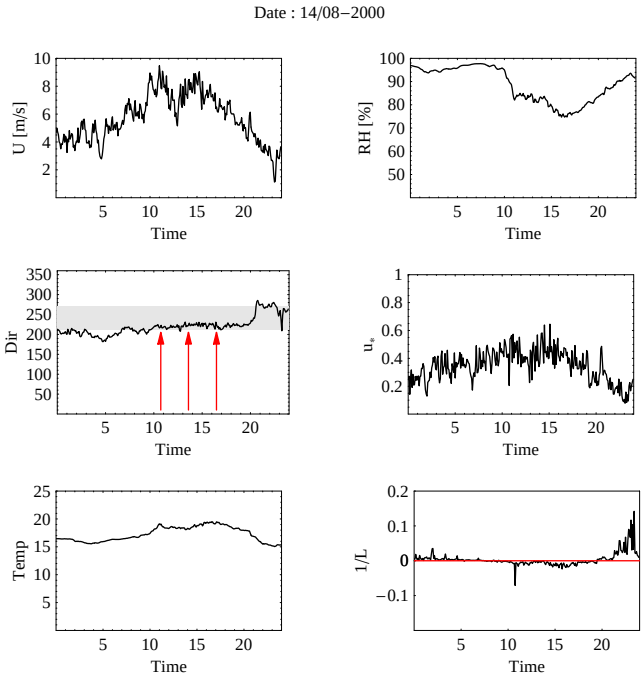

Figure 96. Whole day overview

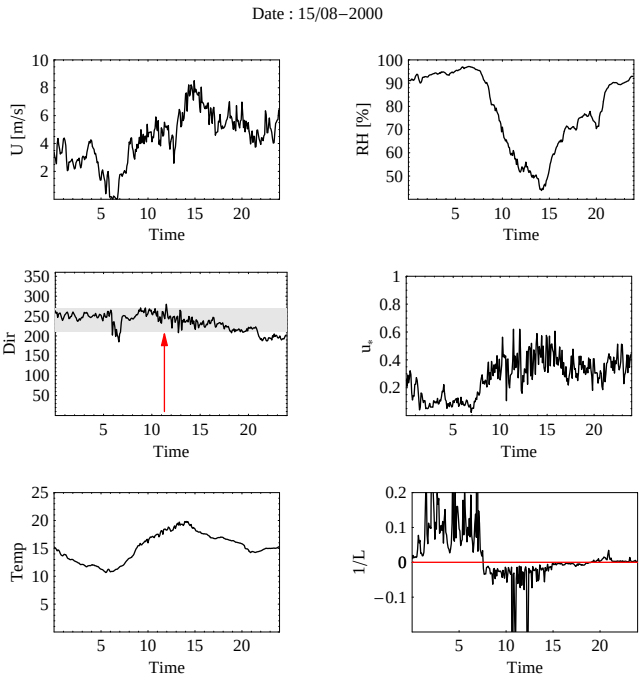

Figure 97. Whole day overview

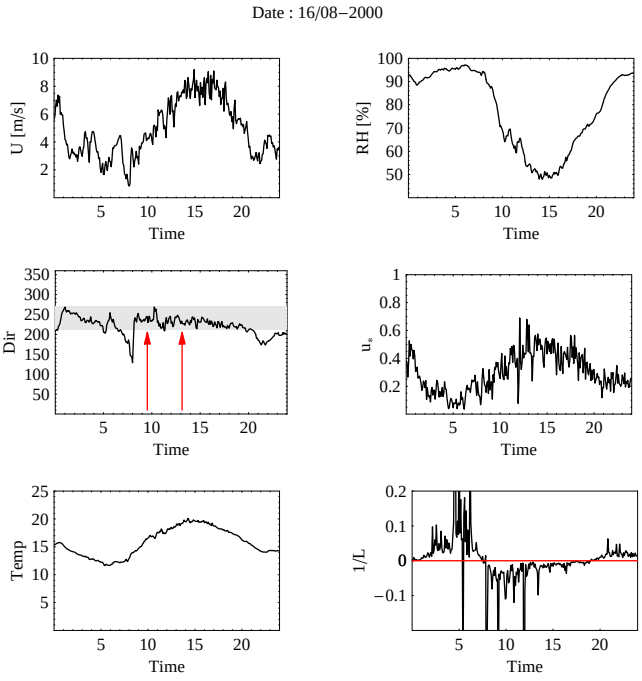

Figure 98. Whole day overview

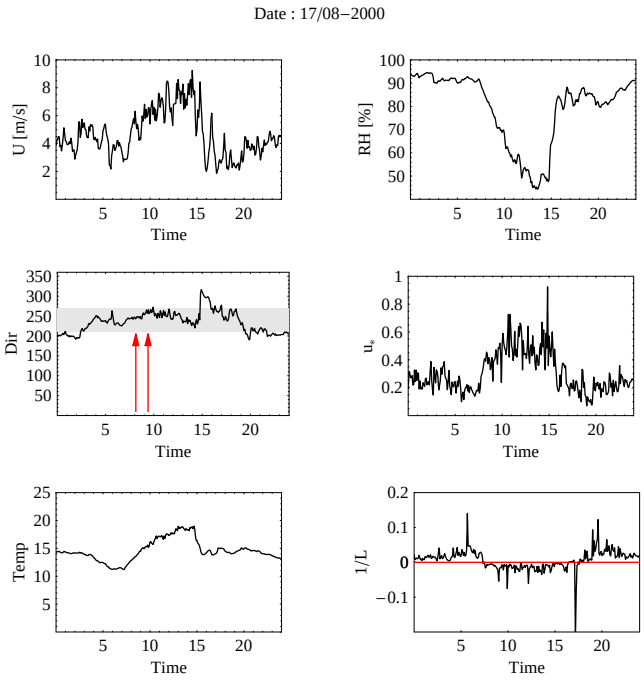

Figure 99. Whole day overview

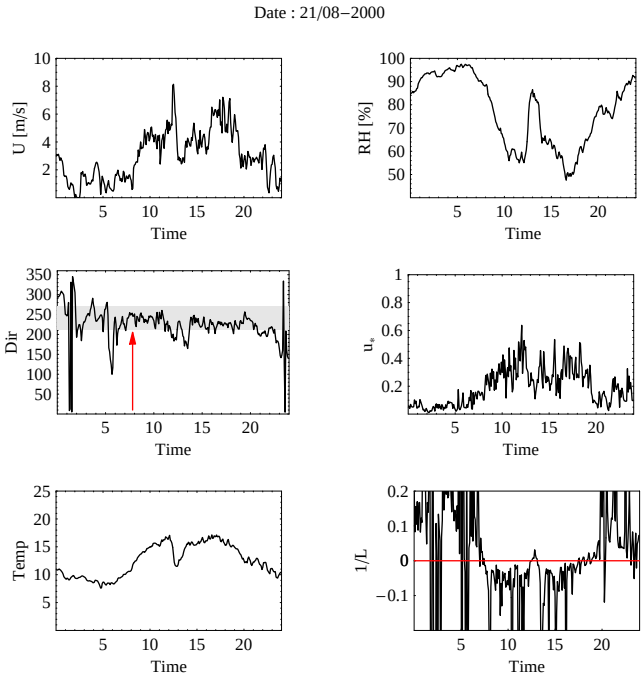

Figure 100. Whole day overview

Bibliographic Data Sheet **Risø–R–1212(EN)**

Title and author(s)

Meteorology and lidar data from the URAHFREP field trials

Søren Ott and Hans E. Jørgensen

ISBN	ISSN
87–550–2762–8;87-550-2763-6(Internet)	0106–2840

Dept. or group	Date
Department of System Analysis	August 2001

Groups own reg. number(s)	Project/contract No.
	CEC D.G. XII ENV4-CT97-0630

Pages	Tables	Illustrations	References
118	44	100	10

Abstract (Max. 2000 char.)

Abstract This report describes the experimental results obtained by the Risø team during the URAHFREP field trials.**U***nderstanding dispersion of industrial* **R***eleases of* **A***nhydrous* **H***ydrogen* **F***luoride and the associated* **R***isk to the* **E***nvironment and* **P***eople*. The purpose of the field trials was to study the possible influence of HF thermodynamics on the dispersion of atmospheric HF clouds. In order to test if the lift-off or enhanced mixing created by the HF release was strong enough compared to the naturally fluctuations the HF releases were accompanied by passive smoke release, made shortly after to obtain a reference to the HF release. The instrumentation included various types of HF sensors, thermocouple arrays, a fully instrumented release rig, a passive smoke machine, a meteorological mast and a lidar backscatter system.This report deals exclusively with the meteorological data and the lidar data. The trials cover a range meteorological conditions. These include neutral conditions with relatively high windspeed and low humidity as well as unstable conditions with low windspeed and high humidity, the most favorable conditions for lift-off to occur.

The lidar was used to scan vertical cross-plume slices 100 meter downwind of the source. A comparison of plume characteristics for HF clouds and passive smoke clouds has been made. The analysis shows no sign of any difference between the dispersion of HF and passive smoke except for one release, where a positive buoyancy effect cannot be excluded. An enhanced mixing effect of HF was not observed.

Descriptors

AEROSOLS; DISPERSIONS; EXPERIMENTAL DATA; FIELD TESTS; FLUCTUATIONS; METEOROLOGY; PLUMES; STATISTICS

Available on request from:
Information Service Department, Risø National Laboratory
(Afdelingen for Informationsservice, Forskningscenter Risø)
P.O. Box 49, DK–4000 Roskilde, Denmark
Phone (+45) 46 77 46 77, ext. 4004/4005 · Fax (+45) 46 77 40 13
E-mail: risoe@risoe.dk